

ELECTRODEPOSITION OF NICKEL SULFIDE AND ITS THERMAL OXIDATION
FOR PHOTOVOLTAIC APPLICATIONS

by

MUNTEHA PAC

Presented to the Faculty of the Graduate School of
The University of Texas at Arlington in Partial Fulfillment
of the Requirements
for the Degree of

MASTER OF SCIENCE IN MATERIALS SCIENCE AND ENGINEERING

THE UNIVERSITY OF TEXAS AT ARLINGTON

December 2011

Copyright © by Munteha Pac 2011

All Rights Reserved

ACKNOWLEDGEMENTS

I owe my deepest gratitude to Dr. Meng Tao. It has been almost 1.5 years since I started working under his supervision, and I clearly see that meeting with Dr. Tao was one of the most important milestones of my life. I am very thankful to him for his guidance, introducing me to the big picture of energy, tolerating my excitement, and patiently teaching me. I am also grateful to the invaluable members of my M.Sc. committee, Dr. Michael Jin, and Dr. Liu Fuqiang, who kindly agreed to be in my committee. I wish I had been wise enough to benefit a little bit more from their vision.

I would not be here, writing these sentences but for my beloved husband. I cannot thank him enough for his support from even before the beginning till the very end of my graduate study in all the ways I can think of.

I would like to express my deep gratitude to my family. My parents deserve infinite thanks not only for their love and support but also for having me brought up with consciousness and moral values. I am also indebted to my grandmother, and my parents-in-law for their immeasurable love, support and prays for me. Also thanks to serendipity for its clear cases at work throughout my life but most importantly by introducing me to Duygu Tamer and Elif Yenilmez.

I am thankful to my dear colleagues Dr. Xiaofei Han, and Bin Zhou for their support. I would also like to thankfully acknowledge Jeniffer Standlee and Libia Cuauhtli for their kindness, support and patience.

I gratefully acknowledge all the faculty members as well as the staff of Material Science and Engineering Department for their generous sharing of their knowledge and resources with a kind demeanor.

I also wish to thank Dr. Nguyen and her research group from Bioengineering Department at UT Arlington for allowing me to use ZetaPals.

This research is supported by the U.S. Department of Energy, Office of Basic Energy Sciences, Division of Materials Sciences and Engineering under Award No. DE-FG02-09ER46597.

November 1, 2011

ABSTRACT

ELECTRODEPOSITION OF NICKEL SULFIDE FOR PHOTOVOLTAIC APPLICATIONS AND ITS THERMAL OXIDATION

MUNTEHA PAC, M.S.

The University of Texas at Arlington, 2011

Supervising Professor: Meng Tao

Alternative photovoltaic materials that feature natural abundance, low extraction and processing costs, and reasonable efficiency have to be found. In this respect, transition metal chalcogenides such as oxide and sulfide compounds of Ni; is studied because in addition to the features like abundance and cost, its electronic and optical properties vary dramatically by modifications in its stoichiometry. In addition to its low cost, and mature technology, electrochemical deposition method has many advantages over other methods since it allows direct deposition on conducting substrate and achieves good electrical contact and precise control of film thickness. Process of manufacturing Nickel Oxysulfide compound consisted of two steps. First, the effect of deposition parameters on film uniformity and adhesion to FTO (fluorine-doped tin oxide) substrate has been investigated. These deposition parameters include gelatin as an additive to stabilize colloidal S [5], the ratio of Ni precursor (NiSO_4) and to S precursor ($\text{Na}_2\text{S}_2\text{O}_3$), and pH and temperature of the deposition solution. Solution stability is measured by zeta potential. Sulfur particles size is determined by DLS. With addition of 8.8×10^{-4} wt% gelatin in the deposition solution, the size of S particles was found to be ~ 250 nm. This eliminates the instability of the solution under acidic pH due to coagulation and flocculation of

colloidal S which causes poor uniformity and weak adhesion. In terms of deposition rate and film uniformity, the precursor ratio (Ni/S), pH, and temperature were found to be optimal at 0.013, 4.7, and 60°C, respectively. XRD is used to determine crystalline phases that constitute film. Only Ni₃S₂ was observed. In conclusion, the deposition solution is stabilized with gelatin and deposition parameters are optimized, leading to a uniform and adhesive Ni₃S₂ thin film on FTO substrate for photovoltaic applications. Finally, after Ni₃S₂ film deposition with desired properties, the thermal oxidation of films at different temperatures is studied. Oxidation at 500-550°C is found to be a temperature where Nickel sulfide film turned to two phases. These phases are Nickel Oxysulfide with an unknown stoichiometry and semiconducting Nickel Oxide.

TABLE OF CONTENTS

ACKNOWLEDGEMENTS	iii
ABSTRACT	v
LIST OF ILLUSTRATIONS.....	x
LIST OF TABLES	xiv
Chapter	Page
1. INTRODUCTION.....	1
1.1 History of energy consumption	1
1.2 Energy Market	4
1.2.1 Fossil Fuels	4
1.2.2 Alternative energy sources and requirements	12
1.2.3 Substitutes for existing petroleum liquids	16
1.2.4 Carbon free alternative energies	17
1.3 Solar Energy	19
1.3.1 Photovoltaics.....	21
1.4 Research Objective	29
2. BACKGROUND.....	31
2.1 Solar Cells	31
2.1.1 History of Solar Cells	31
2.1.2 Solar cell device physics.....	31

2.1.3 Important parameters in solar cells and device requirements	36
2.2 Solar cell absorber materials	39
2.2.1 Solar Cell Material Requirements	41
2.2.2 Metal Sulfides and Oxides	43
2.3.3 Nickel Sulfides and Oxides	48
2.3 Deposition Methods	52
2.3.1 Electrochemical deposition	53
2.4 Characterization Methods.....	57
2.4.1 UV-Vis transmittance spectrum and band-gap calculation	57
2.2.3 X-ray diffraction (XRD).....	58
2.2.4 Scanning electron microscope (SEM)	59
2.2.5 Dynamic Light Scattering and Zeta Potential.....	59
3. ELECTRODEPOSITION AND CHARACTERIZATION OF NICKEL SULFIDE	61
3.1 Introduction	61
3.2 Experimental	62
3.2.1 Sample Preparation	62
3.2.2 Deposition Process	64
3.2.3 Oxidation	65
3.2.4 Characterization	65
3.3 Effect of deposition conditions on Nickel Sulfide film structure	65
3.3.1 Effect of gelatin	66
3.3.2 Effect of Deposition Potential.....	69

3.3.3 Effect of solution temperature	72
3.3.4 Effect of Solution pH	74
3.3.5 Effect of Ni/S precursor ratio.....	75
3.3.6 Effect of Complexing Agents.....	79
3.4 Oxidation of Nickel Sulfide films and its optical properties	84
3.5 Summary	91
4. CONCLUSION AND FUTUREWORK.....	93
4.1 Conclusion	93
4.2 Future Work	94
REFERENCES.....	97
BIOGRAPHICAL INFORMATION	105

LIST OF ILLUSTRATIONS

Figure	Page
1.1 History of energy consumption in the US 1775-2009 [1]	2
1.2 World marketed energy consumption from 1990 to 2035	3
1.3 Primary energy production and consumption by source, 2009. Redrawn from Annual Energy Review 2009 DOE.	4
1.4 Factors governing the rate of global fossil-fuel carbon emissions (a) Global population; (b) Per capita GDP; (c) primary energy intensity (E^* /GDP: left hand scale) and economic productivity of energy (GDP/E^* : right hand scale); (d) carbon intensity of the energy mix; the horizontal lines are emission factors of individual carbonaceous fuels [5]	7
1.5 Fossil-fuel carbon emissions and primary power in the 21st century for for IPCC IS92a and WRE stabilization scenarios.(a) Carbon emissions; (b) primary power and (c) carbon-free primary power. Coloured areas are gas, oil, coal, nuclear and renewable components of IS92a from the energy economics model of Pepper et al.[5]	9
1.6 Primary Energy Flow by Source and Sector,2009 (quadrillion Btu) [21].....	10
1.7 Monthly world oil production and prices, 2002–2010 [6].....	11
1.8 World Rare earth element productions and its price changing with time.....	14
1.9 Graph of world extractable and technical potentials for the various renewable energy sources [23]	20
1.10 The production costs of electricity from coal, gas, oil, wind, nuclear and solar by increasing order	21
1.11 (a) Comparison of energy payback time and (b) energy return on investment for different commercial rooftop PV systems [20, 24].....	23
1.12 Best research cell efficiencies from 1975 to 2009 [27]	24
1.13 (a) Solar cell efficiency record change as a function of cell area, (b) Solar cell efficiency records as a function of cell area [28].....	25
1.14 (a) Module price and efficiency estimates are compared according to the PV technology [28] (b) market share change of crystalline silicon and thin film solar cells [29]	27

1.15 Cost breakdown for Silicon solar (a) modules and (b) systems [30].....	28
2.1 Solar spectrums at different air-mass condition	32
2.2 Cross-section of a p-n junction solar cell	35
2.3 (a) Schematic of the cross-section of a conventional p-n junction solar cell and (b) its energy-band diagram.....	36
2.4 Current- voltage characteristic of a solar cell under illumination	38
2.5 Band gap change with variation in sulfur concentration in (a) Titanium Oxide and (b) Ge Oxide [54,143].....	45
2.6 Possible energy-critical elements are highlighted on the periodic table [21].....	46
2.7 Crystal structures of Ni ₃ S ₂ , NiS, Ni ₃ S ₄ , and NiS ₂ from different perspectives. Blue and yellow balls are represented as Ni and S atoms, respectively [2].....	50
2.8 Phase diagram of Ni-S [136]	51
2.9 (a) Reduction, (b) Oxidation process of a species in solution [127].....	55
2.10 Pathway of a general electrode reaction [127].....	56
2.11 Variables affecting the electrode reaction [127].....	56
2.12 Schematic of V570 Spectrophotometer	57
3.1 Cyclic voltammetry of solutions containing (a) 0.5 M Na ₂ S ₂ O ₃ and (b) 0.013 M NiSO ₄ at pH 4.7. The solution temperature is 60°C. Reduction of S to S ²⁻ is observed around -0.3 V and Ni ²⁺ to Ni reduction around -0.7 V	63
3.2 Cyclic voltammetry of a solution containing 0.013 M NiSO ₄ , 0.5 M Na ₂ S ₂ O ₃ , and 8.8×10 ⁻⁴ wt% gelatin. The solution temperature is 60°C and solution pH 4.7. The reduction potential for S to S ²⁻ is between -0.5 and -1 V	64
3.3 Arrangement of the deposition cell.....	65
3.4 Size of S particles measured by zeta potential as a function of solution pH	68
3.5 Effect of gelatin amount on the film composition. Sulfur percentage in the film composition decreases with increase in Gelatin amount in the solution	69

3.6 Scanning electron microscopy images of Ni ₃ S ₂ films as a function of deposition potential from solutions containing 0.013 M NiSO ₄ and 0.5 M Na ₂ S ₂ O ₃ . The solution temperature is 60°C and solution pH 4.7. Deposition potentials are (a) -0.7 V, (b) -0.6 V, (c) -0.5 V, (d) -0.4 V, and (e) -0.3 V	71
3.7 X-ray diffraction of NiSx films as a function of deposition potential from solutions containing 0.013 M NiSO ₄ and 0.5 M Na ₂ S ₂ O ₃ . The solution temperature is 60°C and solution pH 4.7. All of the films has peaks belonging to the FTO and Ni ₃ S ₂ phase	72
3.8 X-ray diffraction of NiSx films as a function of deposition temperature from solutions containing 0.013 M NiSO ₄ and 0.5 M Na ₂ S ₂ O ₃ . The solution pH is 4.7 and deposition potential -0.4V. The films deposited at 40°C and 60°C are Ni ₃ S ₂	73
3.9 Scanning electron microscopy images of NiSx films as a function of deposition temperature from solutions containing 0.013 M NiSO ₄ and 0.5 M Na ₂ S ₂ O ₃ . The solution pH is 4.7 and deposition potential -0.4V. Deposition temperature is (a) 50°C, (b) 60°C, and (c) 70°C.....	74
3.10 X-ray diffraction of NiSx films as a function of pH from solutions containing 0.013 M NiSO ₄ , 0.5 M Na ₂ S ₂ O ₃ , and 8.8×10 ⁻⁴ wt% gelatin. The solution temperature is 60°C and deposition potential -0.4 V. The film deposited at pH 4.7 shows the most intense Ni ₃ S ₂ peaks. The film deposited at pH 2.73 is largely amorphous.....	75
3.11 Scanning electron microscopy images of NiSx films as a function of Ni/S ratio in the solution. The solution pH is 4.7, solution temperature 60°C, and deposition potential -0.4V. The Ni/S ratio is (a) 0.013, (b) 0.02, and (c) 0.04	76
3.12 X-ray diffraction of NiSx films as a function of Ni/S ratio in the solution. The solution pH is 4.7, solution temperature 60°C, and deposition potential -0.4V. All of the films are Ni ₃ S ₂	77
3.13 Intensity ratio of the (110) to (101) plane coming from Ni ₃ S ₂ films deposited at different Ni precursor concentrations	78
3.14 EDS mapping of (b) S and (c) Ni to demonstrate the compositional uniformity of the film. For comparison, (d) mapping of Sn, which comes from the FTO substrate, is shown.....	79
3.15 pH increase with time in a solution containing 0.1 M NiSO ₄ , 0.5 M Na ₂ S ₂ O ₃	80
3.16 Scanning electron microscopy images of NiSx films as a function of temperature of the solution. The solution pH is 3.9,	

deposition potential $-0.4V$ solution temperature is (a) 50, (b) 60, and (c) 70 (d) 80	81
3.17 Effect of pH on the film structure. The deposition solution contained 0.02 M $NiSO_4$, 0.4 M $Na_2S_2O_3$ and 0.5 M Na Lactate. Solution temperature is set $50^\circ C$. $-0.4V$ is applied for 30 minutes. Solution pH was adjusted between (a) 3.9, (b) 3.5, (c) 3.1 and (d) 2.6 by H_2SO_4	82
3.18 Effect of temperature on the film morphology. 0.02 M $NiSO_4$, 0.4 M $Na_2S_2O_3$ and 0.1 M Tartaric acid solution with pH 2.15 is prepared. Deposition time was 30 min. $-0.2 V$ applied to the cell. Indium doped Tin oxide coated glass substrate (ITO) is used as a working electrode instead of FTO Temperature of the solution was (a)50, (b)60, (c)70, (d)80 $^\circ C$	83
3.19 XRD of sample deposited at 0.02 M $NiSO_4$, 0.4 M $Na_2S_2O_3$ and 0.1 M Tartaric acid solution with pH 2.15 at $60^\circ C$. Deposition time was 30 min. $-0.2 V$ applied to the cell. Indium doped Tin oxide (ITO) coated glass substrate is used as WE	84
3.20 XRD pattern of the $1.4\mu m$ film oxidized at $550^\circ C$ for 3 hours	85
3.21 Secondary electron image from SEM and Ni,O,S elemental compositional ratio from EDS	86
3.22 Transmittance spectra is from the samples before oxidation and deposited at presence of Lactate complexing ion. Thicknesses of the samples are $2.4\mu m$, $0.6\mu m$, $0.35\mu m$, It demonstrates films are opaque and coverage becomes very poor below $0.6\mu m$	87
3.23 Transmittance spectra of the samples having $0.7\mu m$ thickness. Samples are deposited from 0.013M $NiSO_4$, 0.5M $Na_2S_2O_3$, 8.8×10^{-4} wt% Gelatin solution at pH 4.7 Then oxidized at air for 3 hours at $400^\circ C$, $450^\circ C$, $500^\circ C$, $550^\circ C$	88
3.24 Transmittance spectra of $1.4\mu m$ films deposited at the same conditions Samples oxidized at air for 3 hours at $400^\circ C$, $450^\circ C$, $500^\circ C$, $550^\circ C$	89
3.25 Transmittance spectra of the $1.2\mu m$ film after oxidation at different temperatures	90
3.26 Plot of $(Ah\nu)^{1/2}$ vs $h\nu$ of the $1.4\mu m$ film oxidized at (a) $550^\circ C$ and (b) $600^\circ C$ (c) the plot of $(Ah\nu)^2$ vs $h\nu$ of the $1.4\mu m$ film oxidized at $550^\circ C$	91
4.1 Phase diagram of the Ni-S- H_2O system at $25^\circ C$ [142]	95

LIST OF TABLES

Table	Page
1.1 World reserves, world production of rare earth elements [141]	13
2.1 Material requirements for terrestrial solar cells [42]	40
2.2 The fractional bond ionicity, f_i , for selected semiconductors	42
2.3 Effect of polarity of covalent bonding on band gap of compounds [46]	44
2.4 Band Gap Values for Several Metal Oxides, Sulfides	47
3.1 Effect of Gelatin on Zeta-potential of Sulfur Particles	67

CHAPTER 1

INTRODUCTION

1.1 History of energy consumption

Social and economic vitality of communities rely on energy. Types of energy sources have changed the consumption patterns throughout history. Figure 1.1 shows the history of energy consumption in the US [1]. Wood was the main form of energy until 1850s. Wood is replaced by coal as a predominant energy source in the late 19th century by the invention of coal burning steam engine and its widespread practical uses. This ignited the meteoric increase in the global energy consumption. Since 1950s petroleum products has become dominant which accelerated the rise of energy consumption by fueling industrial growth and transportation, increasing population growth, prolonging human lifetime, supplying fertilizers, and powering agricultural equipments. Overall energy consumption pattern by petroleum, coal and natural gas being preeminent form of energy has been fairly stable since 1970s and we have designed our communities for fossil fuels.

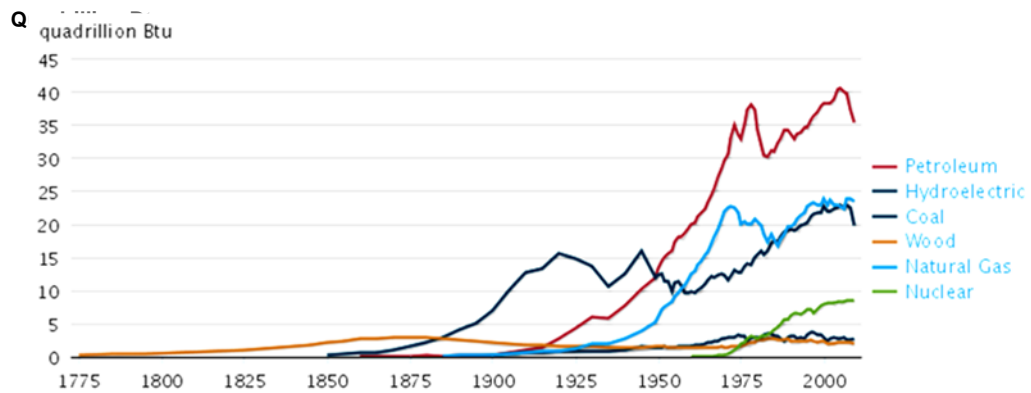


Figure 1.1 History of energy consumption in the US 1775-2009 [1]

According to International Energy Outlook 2010 released by US Energy Information Administration, total world consumption of marketed energy in 2007 is 495 quadrillion Btu, which is 16.5 TW [2] Figure 1.2 shows the history and projections for the world marketed energy consumption from 1990 to 2035. The same report also states that world GDP rises by an average of 3.2 percent per year from 2007 to 2035 which results in world energy demand increase by 49 percent, or 1.4 percent per year, from 495 quadrillion Btu in 2007 to 739 quadrillion Btu in 2035. This analysis is brilliantly named as “the terawatt challenge” by Dr. Smalley. As we look to the future there will be many severe challenges for humans to sustainably produce enough energy to meet that 24.7 TW demand of world.

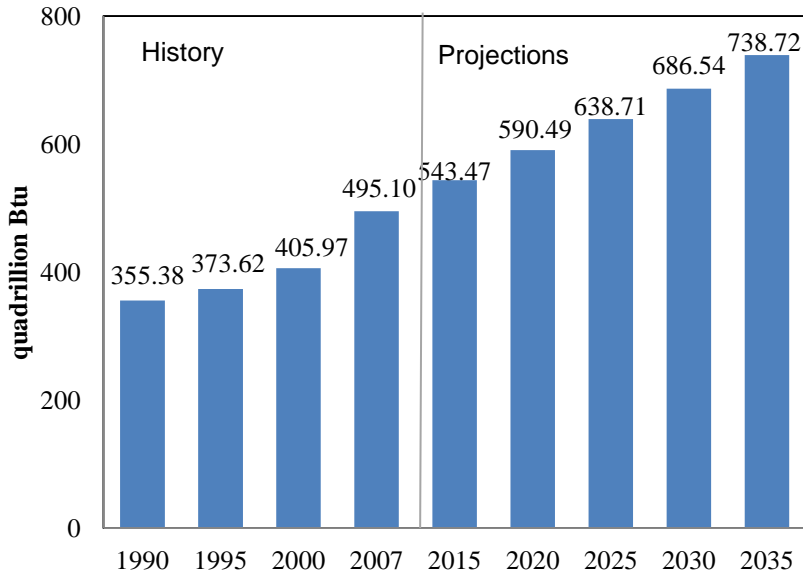


Figure 1.2 World marketed energy consumption from 1990 to 2035

The drivers will be created by population growth, economic growth, ever tightening environmental constraints, increasing climate change issues and pressure for limits on carbon dioxide emissions, geopolitical impacts on energy availability and the energy marketplace, a changing energy resource base, and a need for low emissions transportation.

The most widely used scenarios for future world energy consumption have been those developed by the Intergovernmental Panel on Climate Change. The energy consumption rate (\dot{E}) in this scenario is related to three fundamental factors. These factors are global population (N), globally averaged gross domestic product (GDP) per capita (GDP/N), the energy consumed per unit of GDP (\dot{E}/GDP).

$$\dot{E} = N \times \left(\frac{GDP}{N}\right) \times \left(\frac{\dot{E}}{GDP}\right)$$

Assumptions here are the global population is projected to increase by 0.9% per year to 9.4 billion by 2050 and GDP/N is projected to increase at the historical average rate of 1.4% per year to \$15,000 per capita by 2050. Also if technology continues to improve in energy production, distribution and end use chain, then the global average energy intensity is projected

to decrease at approximately the historical average rate of 0.8% per year from 0.29 W/(\$)per year in 2001 to 0.20 W/(\$) per year by 2050 [5]. As a result even the decrease in energy intensity the world energy consumption rate would grow by 1.5% per year from 13.5 TW in 2001 to 27 TW in 2050 due to population growth and economic growth.

1.2 Energy Market

1.2.1 Fossil Fuels

Over the past decade the three major fossil fuels (petroleum, coal and natural gas) together provided an average of 87% of total US primary energy use, which is indicated in Figure 1.3 [3]. Nuclear power accounted for 8.5% of primary energy, and the remainder of the energy supply came mostly from unsustainable biomass, with a relatively small contribution from renewable sources. If there is no significant change in current laws, regulations, and policies, projects, then world would still significantly rely on the three major fossil fuels through at least 2035 [3].

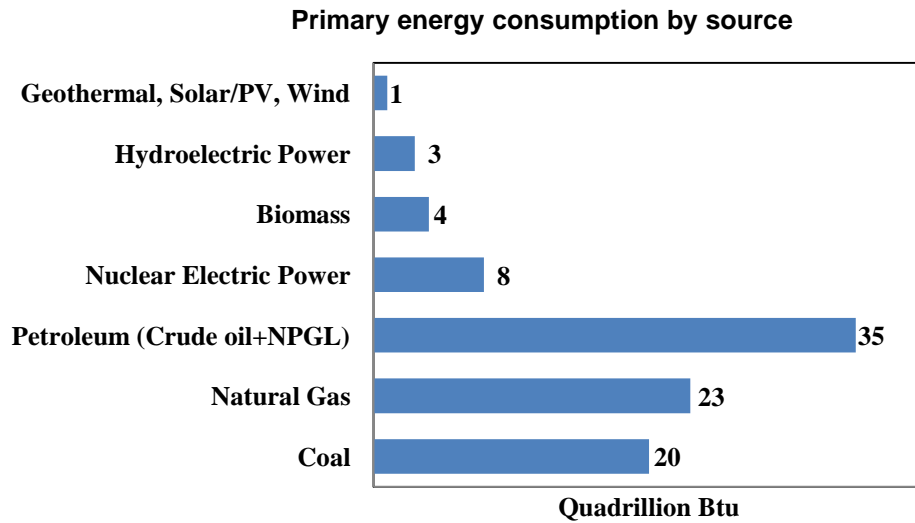


Figure 1.3 Primary energy production and consumption by source, 2009. Redrawn from Annual Energy Review 2009 DOE

Projected global energy demand could be met, in principle, from fossil energy resources, since many sources indicate there are plenty of fossil energy reserves, particularly coal to supply this energy at some reasonable cost. However, consumption of fossil energy at that rate will produce energy security, national security, environmental security, and economic security issues.

First and the most important issue is environmental consequences of atmospheric CO₂ accumulation. When fossil fuels are burned to convert chemical energy to forms of energy in daily use, CO₂ will release. CO₂ absorbs and emits infrared radiation coming from sun light. When a molecule of carbon dioxide absorbs heat energy, it goes into an excited state and by releasing the energy it absorbed it becomes stable again. The released energy will go back to the earth or reflected into space which results in warming the globe. The rate at which carbon is emitted (as CO₂) by energy production is calculated by the equation (1.1):

$$M_c = N(GDP/N)(\dot{E}/GDP)(C/E) \quad (1.1)$$

Product of Population (N), GDP per capita (GDP/N), primary energy intensity (\dot{E}/GDP) Watts/ \$ yr⁻¹, and carbon intensity (C/E) kgC/Watt yr are determined as the contributing factors for carbon dioxide emission rate. Figure 1.4 shows the relative contributions of each factor in the equation by using historical data for 1990 and before, and IPCC scenarios for post 1990. According to IS92 scenario population will reach to 11.3 billion by 2100. Per capita global mean GDP is expected to continue to rise at a rate of 1.6% per year. Energy efficiency and structural changes in the economy governing the material content of economic growth will reduce primary energy intensity at a rate of 1% per year. In the past two centuries, the energy mix has shifted from being wood to coal to oil and now more to natural gas. This shift has decreased carbon emission factor, since energy mix has higher H/C ratio and producing more water and less CO₂ per unit of heat released than does coal. Carbon emission factor is expected to decrease further

if the carbon free energy sources are massively used, ~10 TW by 2050. Although the optimistic decline of the last two factors, i.e. 10 TW carbon-free power by 2050 and sustained 1% per year improvements in energy intensity, overall carbon emission will increase from 6 Gt per year in 1990 to 20 Gt per year by 2100, under the assumption that no regulations are made, which is IS92a scenario.

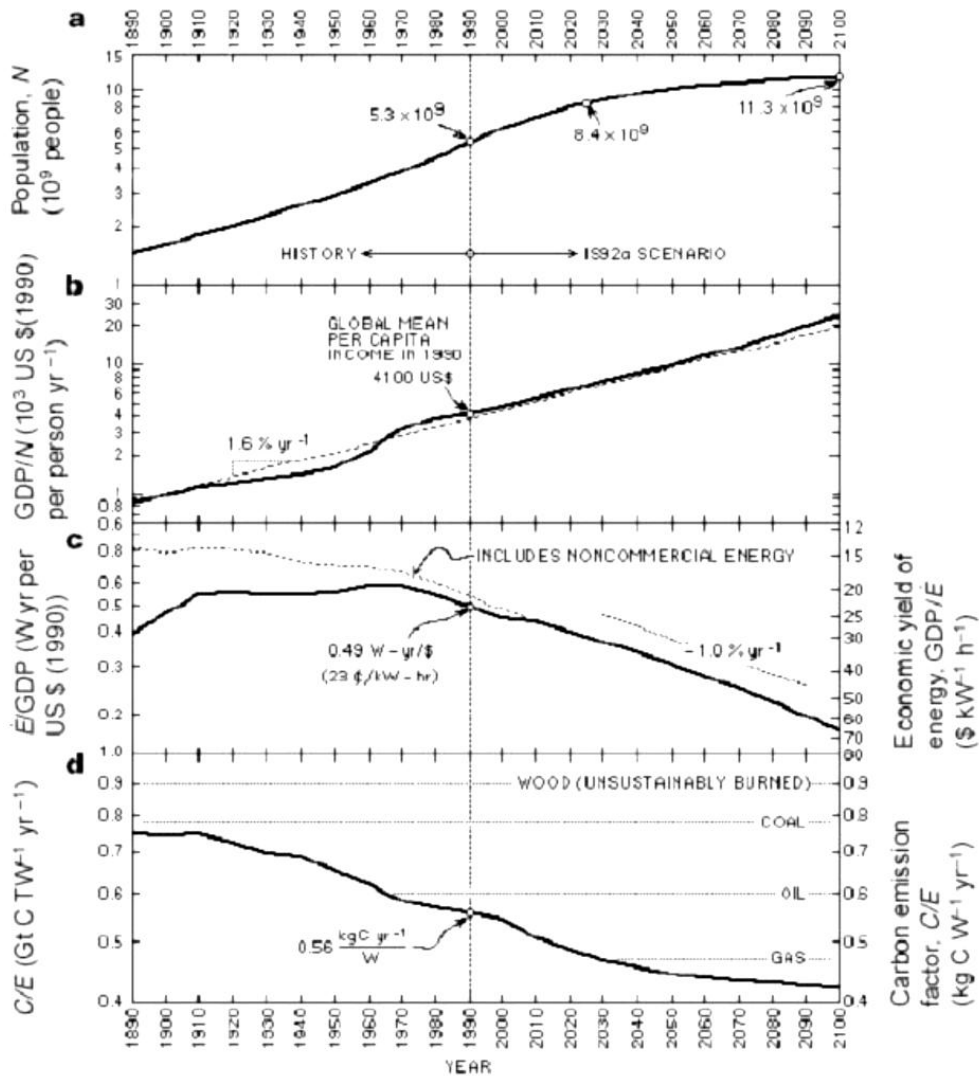


Figure 1.4 Factors governing the rate of global fossil-fuel carbon emissions (a) Global population, (b) Per capita GDP, (c) primary energy intensity (E'/GDP : left hand scale) and economic productivity of energy (GDP/E' : right hand scale), (d) carbon intensity of the energy mix; the horizontal lines are emission factors of individual carbonaceous fuels [5]

What can be said certainly is that due to anthropogenic sources the atmospheric CO_2 concentrations are increasing and without severe intervention will continue to increase. Figure 1.5a shows carbon emission and the curves represent allowable emission levels over time which ultimately stabilize atmospheric CO_2 at 750, 650, 550, 450 and 350 p.p.m.v. computed for the Wigley, Richels and Edmonds (WRE scenarios) stabilization paths. It takes time to reach

the stabilization goals and depends on cumulative carbon emissions. This is why all of the stabilization paths follow the IS92a emissions at first and reduce after some time. Figure 1.5b shows primary power levels required to meet total energy demand with gas, oil, coal, nuclear and renewable components. WRE lines show the allowable power from fossil fuels for different stabilization scenarios. In order to meet the energy demand the area between WSE lines and IS92a line should be met by renewable sources. This is illustrated in Figure 1.5c by graphing carbon-free primary power required for IS92a and CO₂ stabilization scenarios.

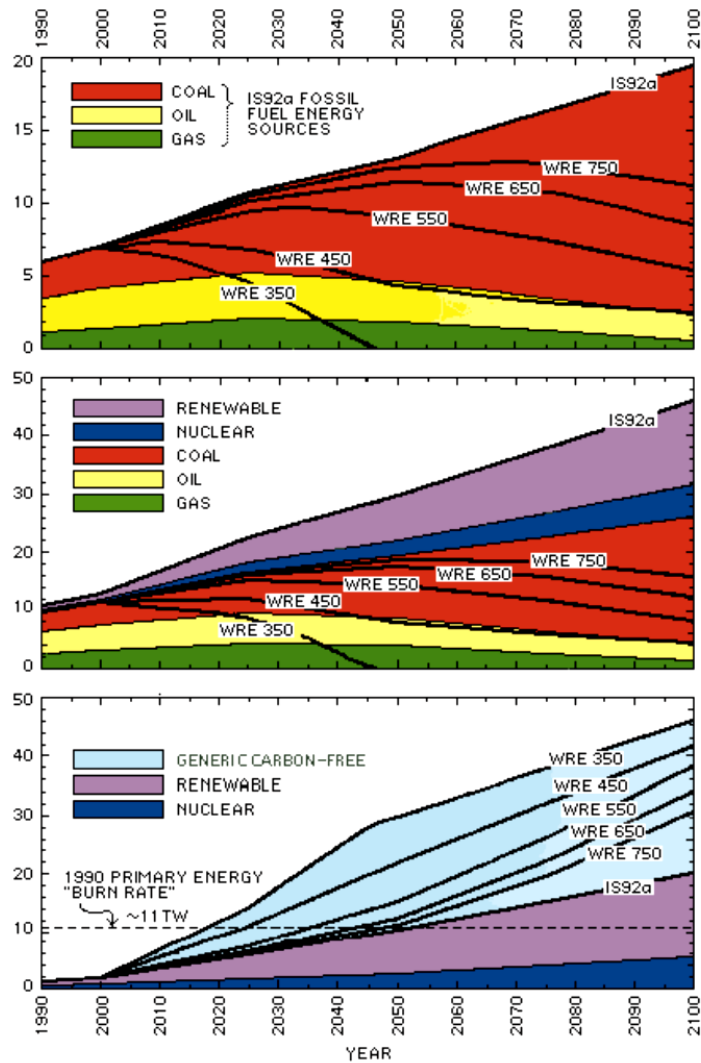


Figure 1.5 Fossil-fuel carbon emissions and primary power in the 21st century for for IPCC IS92a and WRE stabilization scenarios. (a) Carbon emissions, (b) primary power and (c) carbon-free primary power. Coloured areas are gas, oil, coal, nuclear and renewable components of IS92a from the energy economics model of Pepper et al.[5]

As a result, in order to stabilize the atmospheric CO₂ levels at WRE 750 level we need to deploy carbon-neutral energy sources even larger than the entire present-day energy supply from all sources combined. Clean and sustainable energy supply remains as the most important challenge in the 21st century.

In addition to environmental issues, energy security, national security, and economic security are other visible problems that are being faced for communities relying on fossil fuels to meet their energy demand. Today world economic and societal infrastructure is fully dependent on cheap fossil fuels. Figure 1.6 shows how much we become dependent on cheap fossil fuels. 97% of transportation, 88% of industrial, 94% of resident and commercial, 65% of electric power energy comes from fossil fuels [21].

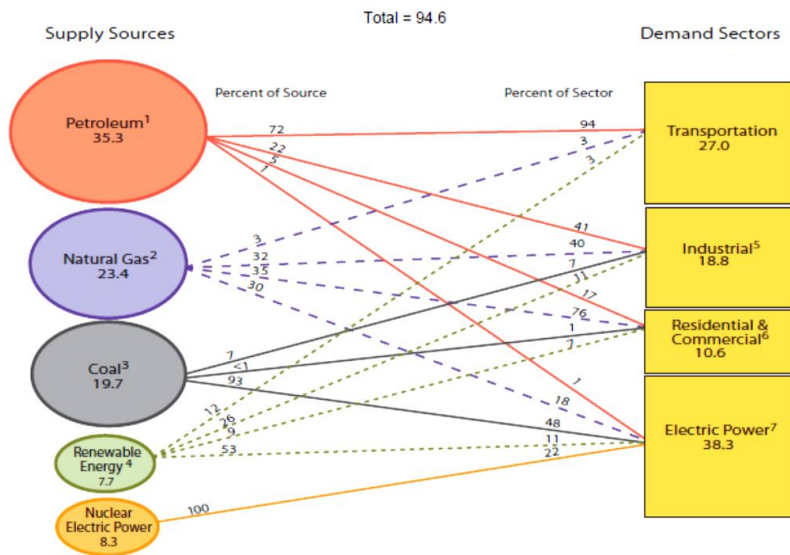


Figure 1.6 Primary Energy Flow by Source and Sector, 2009 (quadrillion Btu) [21]

Among all types of fossil fuels, petroleum instability is the most important issue in terms of energy security and economic security, since it reached its peak at 2007. Figure 1.7 shows that world production flattened in the vicinity of 85 million to 86 million bpd, suggesting that all-time peak-oil production has already occurred [6]. The International Energy Agency (IEA) World Energy Outlook 2008 report released in November concludes that “Current global trends in energy supply and consumption are patently unsustainable, the sources of oil to meet rising demand, the cost of producing it and the prices that consumers will need to pay for it is extremely uncertain.” [7]

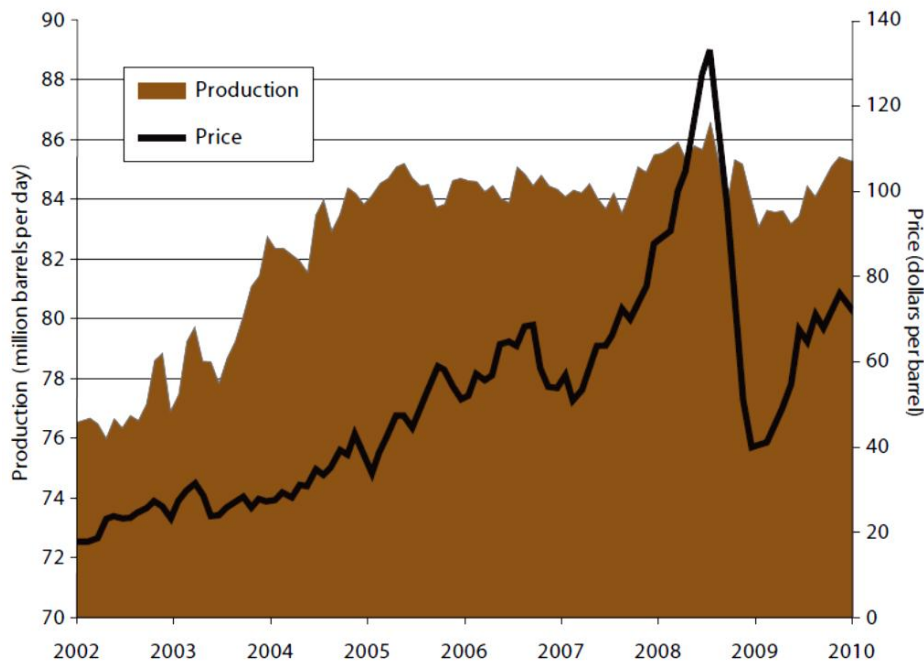


Figure 1.7 Monthly world oil production and prices, 2002–2010 [6]

There are four reasons that make oil very important for economic vitality of communities [8]. First one is its being key raw material for gasoline, diesel, jet fuel, industrial oils, many chemicals, and most plastics which makes it essential for the most basic functions of industrialized world. As well as being fuel for modern agriculture, transportation and manufacturing system, it is used as raw material for agricultural chemicals. As a result all sectors in global economy will be seriously affected by instability in oil supply and price. Second one is that considering the current rate of consumption there are no substitutes for oil at this moment. Third one is global economy in terms of governmental and firm relationships depend on predictability of oil price and availability. Last one is stated at the 2005 report on peak oil for the U.S. Department of Energy and it claims that nearly all future world oil production growth depends on supplies from OPEC. Natural gas is also problematic in long term alternative since

significant gas import dependency in Europe and expensive production from unconventional sources.

1.2.2 Alternative energy sources and requirements

Alternative sources of secure, clean and sustainable energy are required due to population growth, economic growth, environmental constraints, geopolitical impacts on energy availability and the energy marketplace. Alternative energies can be divided into two groups: First group contains substitutes for existing petroleum liquids, such as ethanol, biodiesel, bio-butanol, coal to liquids, tar sands, oil shale from biomass and fossil feed stocks. Second group is alternative technologies to generate electricity and store power. These technologies including but not limited to wind, solar to electricity, solar to thermal, tidal, biomass, fuel cells and batteries.

Extensive physical requirements, resource use trade-offs, and material scarcity are making the development of alternative energy technology much more complex than simple monetary metrics or carbon footprint calculations. The discussion of this issue is biased by politics, basic science is ignored and the magnitude of the problem is not appreciated. In order to claim the promise of any particular alternative energy form the factors coming into play should be discussed first [9].

1.2.2.1 Material Input Requirements

Scalability, cost and feasibility of the prospective alternative is limited by the input to that alternative energy. Contrary to popular belief, input is not all about money. It includes resources and energy needed. In terms of resources, its availability and geographical distributions are things should be considered before diverging to an alternative energy path. Table 1.1 below shows some technologies vastly depending on rare earth materials.

Table 1.1 World reserves, world production of rare earth elements [141]

Raw Material	Fraction of Today's Total World Production Emerging Technologies (selected)		Emerging Technologies (selected)
	2006	2030	
Gallium	0.28	6.09	Thin-layer photovoltaic, integrated circuits, white LEDs
Neodymium	0.55	3.82	Permanent magnets, laser technology
Indium	0.4	3.29	Displays, thin-layer photovoltaic
Germanium	0.31	2.44	Fiber-optic cable, infrared optical technologies
Scandium	Low	2.28	Solid oxide fuel cells, aluminum alloying element
Platinum	Low	1.56	Fuel cells, catalysts
Tantalum	0.39	1.01	Microcapacitors, medical technology
Silver	0.26	0.78	Radio-frequency ID tags, lead-free soft solder
Tin	0.62	0.77	Lead-free soft solder, transparent electrodes
Cobalt	0.19	0.4	Lithium-ion batteries, synthetic fuels
Palladium	0.1	0.34	Catalysts, seawater desalination
Titanium	0.08	0.29	Seawater desalination, implants
Copper	0.09	0.24	Efficient electric motors, radio-frequency ID tags
Selenium	Low	0.11	Thin-layer photovoltaic, alloying element
Niobium	0.01	0.03	Microcapacitors, ferroalloys
Chromium	Low	Low	Seawater desalination, marine technologies

So far it has been easy to provide the volume of alternative energy sources and energy demanded for its production since only 7% of the total energy consumption comes from renewable energy. However this will not be the case in the large scale production, when it comes to contribute sufficient amount of energy to replace fossil fuels. Demand will increase for most of the materials, and even reach beyond the total production capacities for Gallium, Neodymium, Indium, Germanium, Scandium, Platinum, and Tantalum. The graph below shows the world rate production and price of rare earth elements. Also the reserves of rare earth materials mostly located and produced in China which will threat the energy independence of

other countries which is similar to the case for now dependency on Middle East for oil. Since China is the both primary consumer and leading producer we see a falling trend in the rare earth elements prices in Figure 1.8 [22]. Although it is not shown in the graph, the price of most REE rose significantly at 2007 due to increase in Chinese consumption and Chinese government export control. This lead USA to restart processing of its REE mines again. As a result energy technologies depend on rare earth materials will not cure energy security concerns.

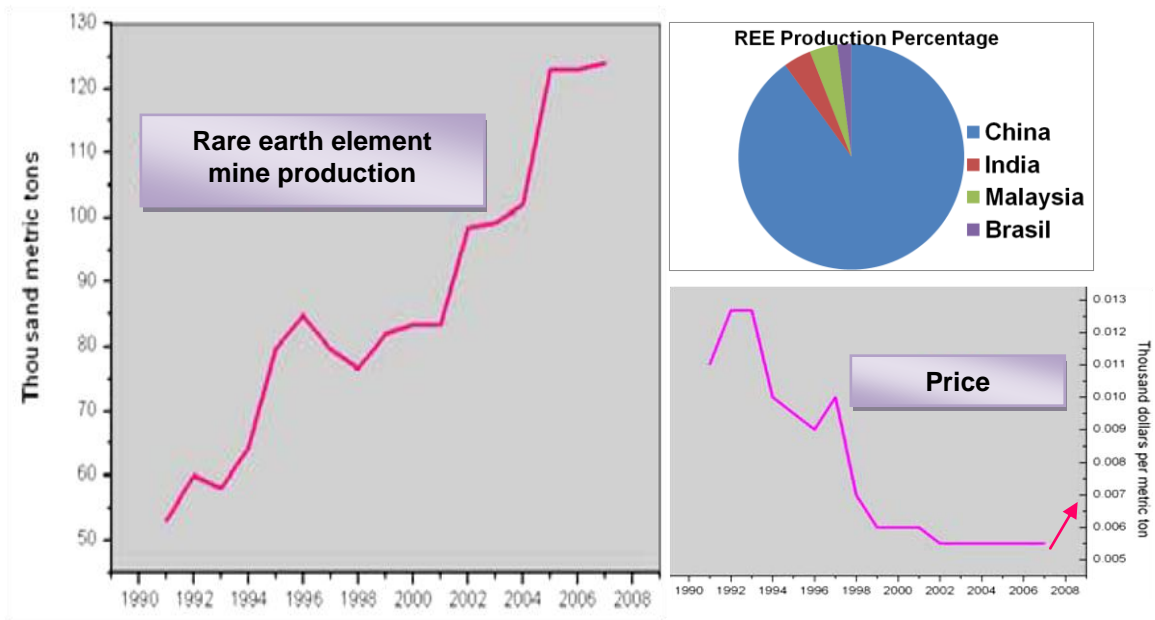


Figure 1.8 World Rare earth element productions and its price changing with time

One can claim that these elements can be replaced during the development of that particular technology with some performance trade-offs, but attempting for an alternative energy technology without consideration of long term availability of the material will simply risk the supply disruptions. Factors that influence the price of Al, Cd, Co, Cu, Fe, Ni, Pb, Rare Earth Elements, and Zn are stated as ,scarcity , supply-demand balance, stocks and rate of use,

actual or anticipated supply disruption, earnings, market performance and expectations, investment level, globalization, governments, geopolitics, growth at the report of USGS [10].

1.2.2.2 The law of receding horizons [11]

Often it is considered that break-even point of an alternative energy with oil will be the turning point that make alternative as competitive. Break-even point is calculated by assuming the cost of input of an alternative energy would remain stable, even go lower with the technology development while the price of oil will be higher. It is often ignored that for alternative energy major part of input is constituted by oil. This makes oil price rise leads to increase in production cost of an alternative energy.

1.2.2.3 Energy return on investment (EROI) and energy payback time (EPBT)

EROI is the ratio of the amount of energy produced from the system to amount of energy put to energy production system. If the ratio is equal to or less than 1 than system is called energy sink. In order to maintain current structure of industrial society a prospective alternative energy system should have at least 5:1 ratio, which means amount of source input cannot exceed 20% of energy produced [12]. Energy payback time (EPBT) is introduced since EROI doesn't include time which is also an important factor. EPBT is the time required for an energy system to generate an amount of energy equal to the total energy that is consumed during its production.

1.2.2.4 Energy Density

Energy density can be defined as energy stored per unit of mass or per unit volume. This definition has been effective in our choice of oil over coal or wood since oil has much higher energy density compared to other fossil fuels. Low energy density means it will require larger amount of source when compared to high energy density material. As a result energy density is important in terms of land and source.

1.2.2.5 Intermittency

Current energy system is structured according to continuous flow of energy but some promising alternative energies such as wind and solar cells are producing energy intermittently. System integration is necessary to balance demand, availability and production of energy. Approaches to solve this problem are storing or grid system.

1.2.2.6 Scalability and Timing

Alternative energy forms are expected to supply required amount of energy at the time needed and replace fossil fuels seamlessly in contrast to difficulties in growing energy demand and greenhouse gas emission stabilization. Even if an alternative energy technology promises to meet the expanding demand, transferring a technology from laboratory demonstration to large commercial scale takes at least 20 years. Also scalability comes into play when we compare the projected production rates with increasing demand rate and depletion of petroleum.

I will discuss alternative energy types, which are expected to supply 10-20 trillion watts of power, their limitations and strengths in the light of factors that I have listed above, i.e. scalability and timing, intermittency, energy density, energy return on investment (EROI), the law of receding horizons, material input requirements.

1.2.3 Substitutes for existing petroleum liquids

In order to keep current structure of our large scale, centralized energy system some substitutes are tried to push forward ,such as ethanol, biodiesel, biobutanol, dimethyl ether, coal to liquids, tar sands, oil shale, both from biomass and fossil feedstock. These are usually referred as clean substitutes but some of them, such as coal to liquids or tar sands are usually dirtier than petroleum. Also it is reported that 2.1 million bpd increase in the production of tar sands will not even make up half of depletion of oil which is estimated to be 4.8 million bpd [15]. Algae based diesel, cellulosic ethanol, biobutanol are demonstrated in small scale and they are based on 'production', instead of 'extraction' as in petroleum. Production requires construction

of equipments and manufacturing process, and these involve prompt resources and input energy and this constrains the scalability and timing. Target ethanol production is set to 36 billion gallons, which is equivalent to 890,000 bpd gasoline, by 2022 [9]. Annual energy outlook projects the increase in gasoline demand as 930,000 bpd by 2022 which will be higher than production of ethanol [16]

1.2.4 Carbon free alternative energies

1.2.4.1 Nuclear Power

In order to establish if this type of carbon free energy source can be scalable to 10 TW or higher we need to make some simple calculations. According to the data from EIA, at 2010 world nuclear net electricity generation is 0.3TW [14].

In order to increase the world nuclear electricity net generation to 10 TW by using 1GW reactor capacity power plants until 2050, we need to build 10,000 new power plants. This number is huge, and at least one power plant with 1GW capacity should be built every other day continuously in the next 50 years. Even if we built power plants with this enormous rate, there is a resource scarcity problem since the proven reserves and the resource base of all terrestrial uranium combined is enough to provide only 10 years of operation for the 10,000 necessary nuclear power plants [13]. Plutonium based power plants and reprocessing to eliminate scarcity problem is another possibility but it needs to be evaluated thoroughly.

1.2.4.2 Carbon Sequestration

In this process CO₂ emitted from a power plant will be captured and then sequestered in deep ocean or geological reserves. In addition to its adverse effect on ecology (increase in acidification of ocean), keeping leak rate of reservoirs below 1% for centuries restrict the areas to be used as reservoirs. Also we usually think coal as being so abundant that supply constraints will not appear for many decades or even centuries. However a report by the National Academy of Sciences at 2007 claims that "Present official US estimates of coal reserves are based upon methods that have not been reviewed or revised since their inception

in 1974, and much of the input data were compiled in the early 1970s. Recent programs to assess reserves in limited areas using updated methods indicate that only a small fraction of previously estimated reserves are actually minable reserves.” [17].

1.2.4.3 Tidal energy

The energy in all the currents, all the tides, and all the waves on our planet combined is much less than 10–20 TW needed [13].

1.2.4.4 Biomass Energy

Biomass-based fuels depend on seasonal harvests of crops which makes it vulnerable to adverse climatic change. By being land and water intensive, it becomes not scalable to terawatt energy demand of future. This type of alternative energy is inefficient since it relies on energy storage of plants by photosynthesis and by doing it they store only <1% of the total incident energy that they receive from sunlight. The production of 3TW of power requires 600 million hectares of land [18], so in order to produce 20TW from biomass the total amount of land required will be 31% of the total land area on earth covered by energy farms. These farms should be devoted to producing biomass to meet the carbon-free energy demand requirement, which would be unrealistic in a world with a growing population and food demand.

1.2.4.5 Wind Energy

According to the National Renewable Energy Laboratory study in the 1990s, if windmills are sited at optimal spacing to prevent obscuration of one another (4%–5% spacing) and nothing is excluded other than environmentally sensitive lands or urban areas, a significant amount of electricity could be produced. But adding up class three and four rated lands of earth with practical site constraints, there is a potential of 2-4 TW [13]. In order to meet 10-20 TW demand, immense far offshore wind mills have to be built, which will bring transmission issue of the produced energy demand areas. Another big problem with the wind turbines is the intermittency and demands an accompanying energy storage system. Also an essential

component of the turbine is permanent magnet is made from neodymium which is a rare earth material.

1.2.4.6 Hydroelectric Energy

The total feasible hydrological energy potential of the planet is approximately 1.5 TW [13], most of which is currently exploited to a large degree. Although this is a very attractive renewable resource, we cannot meet requirement for 10-20 TW of carbon-free power primarily through the exploitation of hydroelectricity. Hydroelectricity is a very attractive renewable resource

1.3 Solar Energy

From the 1.2×10^5 TW of solar energy that strikes the earth's surface but a practical siting-constrained onshore terrestrial global solar power potential value is about 600 TW, which is much larger than current and projected energy consumption [13]. So among renewable energy resources, solar energy is the largest exploitable resource since it can provide more energy in 1 hour to the earth than all of the energy consumed in a year. This makes solar energy to be the best candidate for future energy supplies in terms of capacity. Comparison of world extractable and technical potentials for the various renewable energy sources is shown in Figure 1.9. Basically, there are three different ways to use solar energy. First, solar energy is converted to heat conversion by focusing sunlight by concentrators to heat this spot up to 3000°C which will transfer heat to a thermal storage medium. Although this technology currently has the potential to provide electricity that is competitive in price with that generated from fossil energy in the long term, it needs large areas in the sun belt to work which makes it a limited global energy potential on the 10-20 TW scale. Second, solar energy is converted to chemical energy through the photosynthetic process to obtain alternative fuels. Fuel may be in the form of sugar and other carbohydrates to be used as biomass for conversion to secondary fuels such as liquid ethanol and methane. Photosynthesis is relatively inefficient, so biomass farms require extremely large areas per unit of output energy produced. Also water is split by the

photosynthetic process with artificial molecular assembly in order to produce fuel in the form of hydrogen. Third, solar energy can be converted to electricity. The actual land area that is required to produce 20 TW of carbon-free power from solar energy is 0.16% of the earth's surface assuming an overall 10% conversion efficiency of the amount of solar energy that is incident on the land (day/night, seasonal, and latitude averaged). For US, producing 3 TW at 10% efficiency would require covering 1.7% of the land in the U.S, which cannot be underestimated. In this research, solar electricity generated by light-induced voltage, i.e. photovoltaic (PV) effect will be explored and this technology is discussed in detailed in the next section.

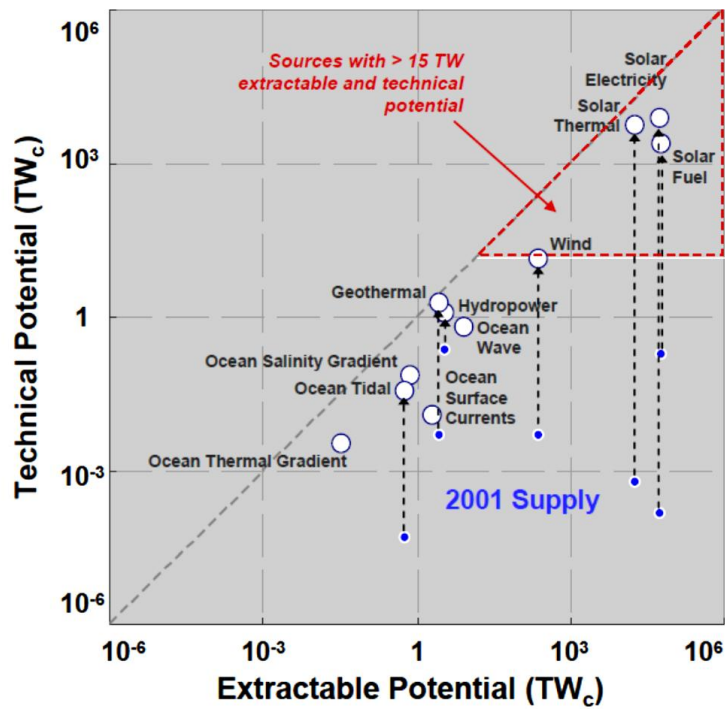


Figure 1.9 Graph of world extractable and technical potentials for the various renewable energy sources [23]

1.3.1 Photovoltaics

1.3.1.1 Evaluation of technology

Since solar cells has the highest potential to meet energy demand in terawatt scale , we need to evaluate it further in terms of material input availability, scalability and timing, intermittence, the law of receding horizons, energy return on investment (EROI), and energy density. First issue, the most popular one, is the high cost per watt of electricity produced. Figure 1.10 shows the production costs of electricity from coal, gas, oil, wind, nuclear and solar by increasing order. Also it is generally projected that solar cell cost become lower and lower where as oil price becomes higher and higher. Although technology is developing to decrease the cost of the cell, the production is dependent on oil which means increase in oil price will also increase the production cost of solar cells (the law of receding horizons) since the economy is interpenetrated with oil price.

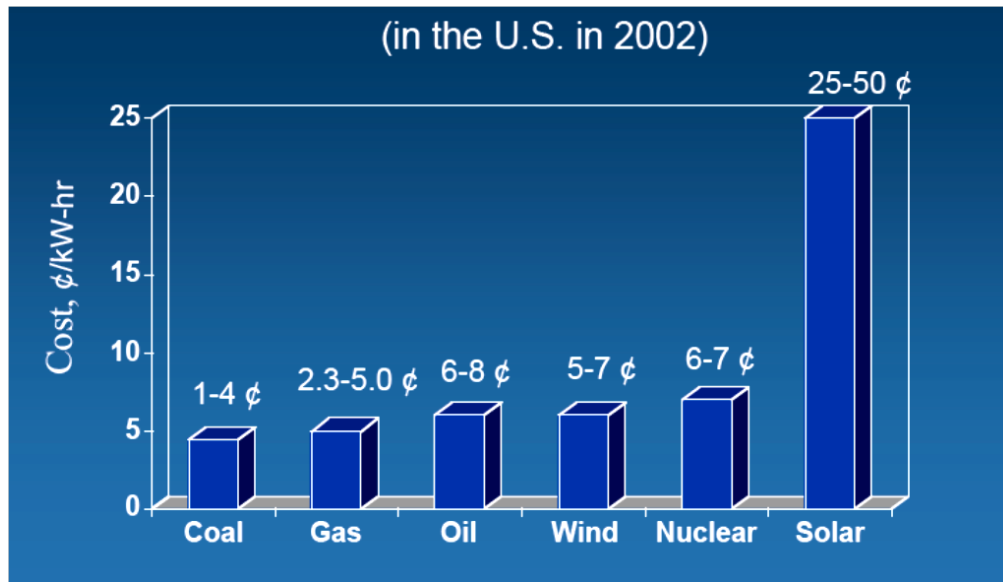


Figure 1.10 The production costs of electricity from coal, gas, oil, wind, nuclear and solar by increasing order

Material input availability is another issue which may become more important than cost when TW scale production is considered. This will be discussed in the following section. Contrary to public belief only 0.25 TW of power could be generated when 10% efficient solar cells are installed to every home rooftop in US [13]. As a result meeting the energy requirement in urban areas from solar panels is possible by installing panels to the outside of the cities which will bring transmission issues. In view of the intermittency, if solar energy is to be a major primary energy source, it must be stored and dispatched on demand to the end user. Another very important factor that determines the feasibility of an alternative energy is energy return on investment (EROI) and energy payback time. The value of EPBT depends on three factors: (i) the efficiency of the photovoltaic system; (ii) the amount of illumination (insolation) that the system receives; and (iii) the manufacturing technology to produce the solar cells. The efficiency and insolation can be measured without extensive effort. However, when it comes to manufacturing technology there are different ways to manufacture solar cells. One way is deposition of thin film semiconductors. But the most common way is to cut wafers from silicon ingot which can be single or multi crystalline cells, and both being a highly energy intensive process. This is not a straight calculation to do, because today's PV industry generally recrystallizes "off-grade" silicon from the microelectronics industry, sometimes referred as scrap, and estimates for the energy used to purify and crystallize silicon vary widely. So the EPBT results differ according to data source. Figure 1.11 shows the EPBT and EROI estimates from NREL for rooftop PV systems. 4 years for systems using current multicrystalline-silicon PV modules, 3 years for current thin-film modules, 2 years for anticipated multicrystalline modules, and 1 year for anticipated thin-film modules [20]. EROI graph drawn from according to system energy payback times for several different photovoltaic module technologies. Assumptions are 1700 kWh/m²/yr insolation, 75% performance ratio for the system compared to the module. and life expectancies of 30 years [24].

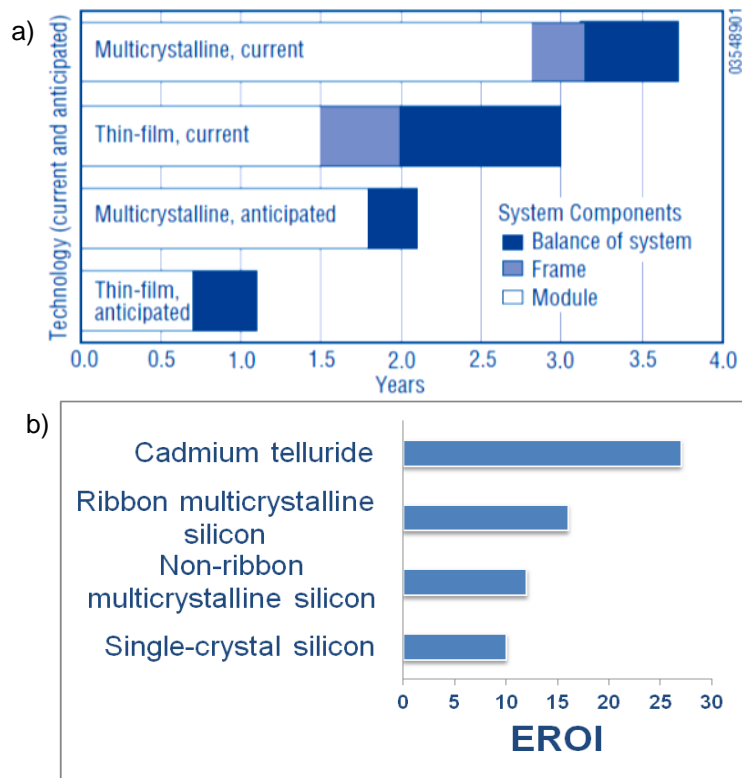


Figure 1.11 (a) Comparison of energy payback time and (b) energy return on investment for different commercial rooftop PV systems [20, 24]

1.3.1.2 Current PV market

US photovoltaic industry has been growing with an average 30% per year. Photovoltaic cell and module shipments in US reached to 1.3GW in 2009 [25]. Also the world-wide installed capacity of the solar photovoltaic power has increased from 331 MW in the year 2001 to 16.7 GW in 2010 [26]. The drivers for this industry are raising energy cost, increased subsidies by the governments, energy security and environmental concerns; and technology development.

Photovoltaic cells can be classified in four different classes by product type and they differ in efficiency and cost. Figure 1.12 below shows the best research cell efficiencies changing with time [27]. Crystalline Si is one type of cells that has three subtypes, single crystalline, polycrystalline and ribbon Silicon with changing efficiencies 24%, 20%, and 16%, respectively. Thin film is other cell type that is made from different semiconductors such as,

Cu(In, Ga)Se (CIGS), CdTe, and amorphous Si. Their efficiencies are around 12%. Third type of solar cells is multijunction which include a reflective (mirror) or refractive device (lens) that gather and concentrate sunlight on to the cell. Its efficiency is around 36%. The last type is organic cells which is named as emerging PV and has 4% laboratory efficiency.

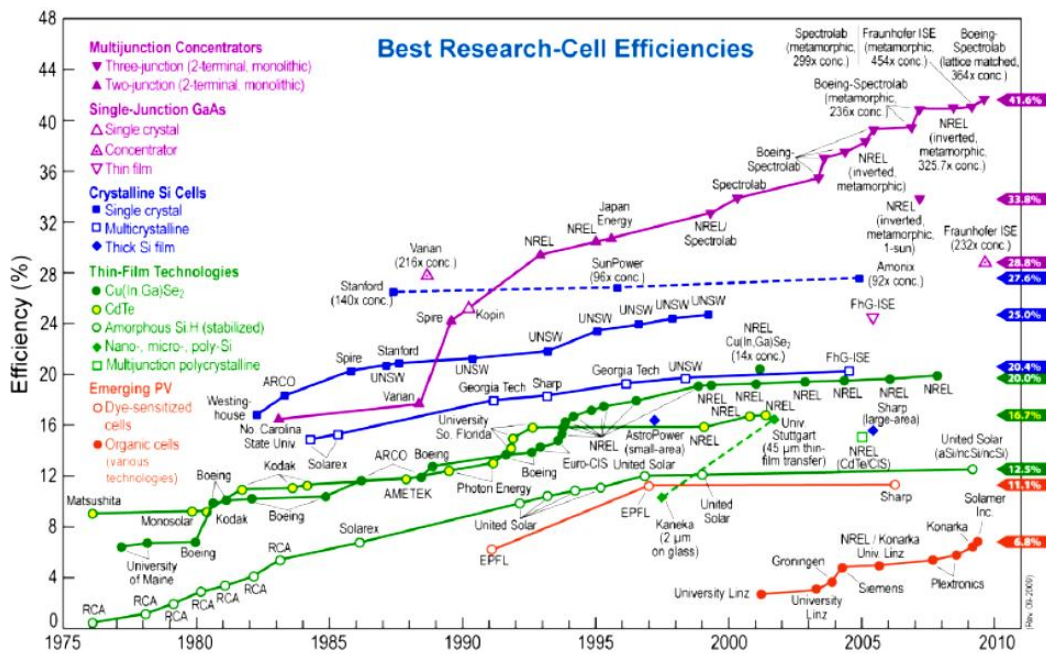


Figure 1.12 Best research cell efficiencies from 1975 to 2009 [27]

We also should keep in mind that solar cell efficiencies tend to decrease with increase in the area. Solar cell efficiency record change as a function of cell area is shown in Figure 1.13.a. As a result in addition to laboratory cell efficiency the commercial module efficiency increase with time should be checked which is demonstrated in Figure 1.13.b.

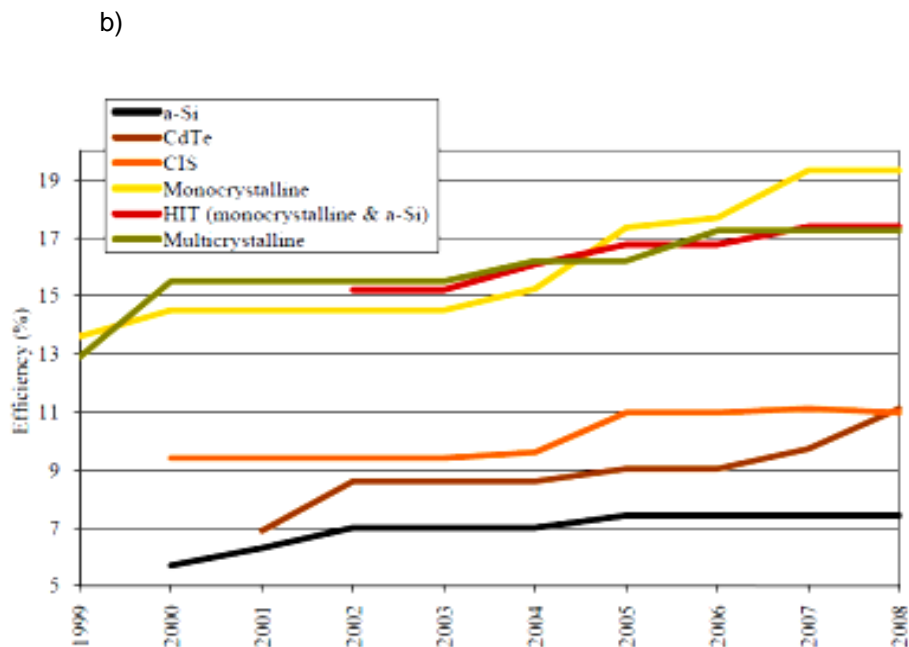
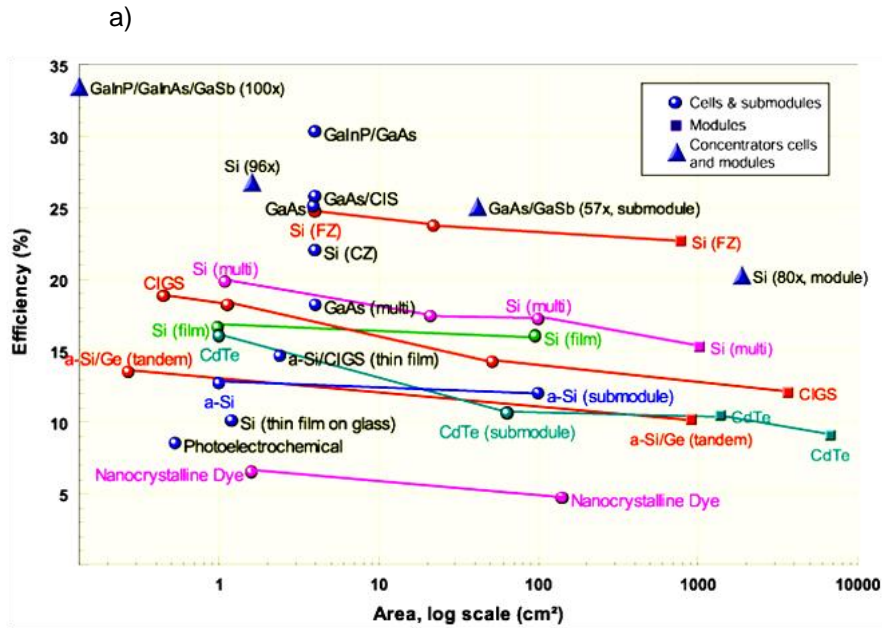


Figure 1.13 (a) Solar cell efficiency record change as a function of cell area, (b) Solar cell efficiency records as a function of cell area [28]

Crystalline Si has the 80% of the market share. Although thin film solar cells started to increase their share, the market is still dominated by crystalline Si solar cell. Also crystalline silicon cells are getting some of the lost market share from thin-film cells/modules since 2007 (

Figure 1.14) Concentrator solar cells are also started to increase their market share. Although crystalline Silicon, CdTe, CIGS and concentrated solar cell market is growing steadily, there are still fundamental problems exist for the current technologies which prevents them contributing world energy production in TW scale. Issues with the commercial PV technologies will be discussed in the next section.

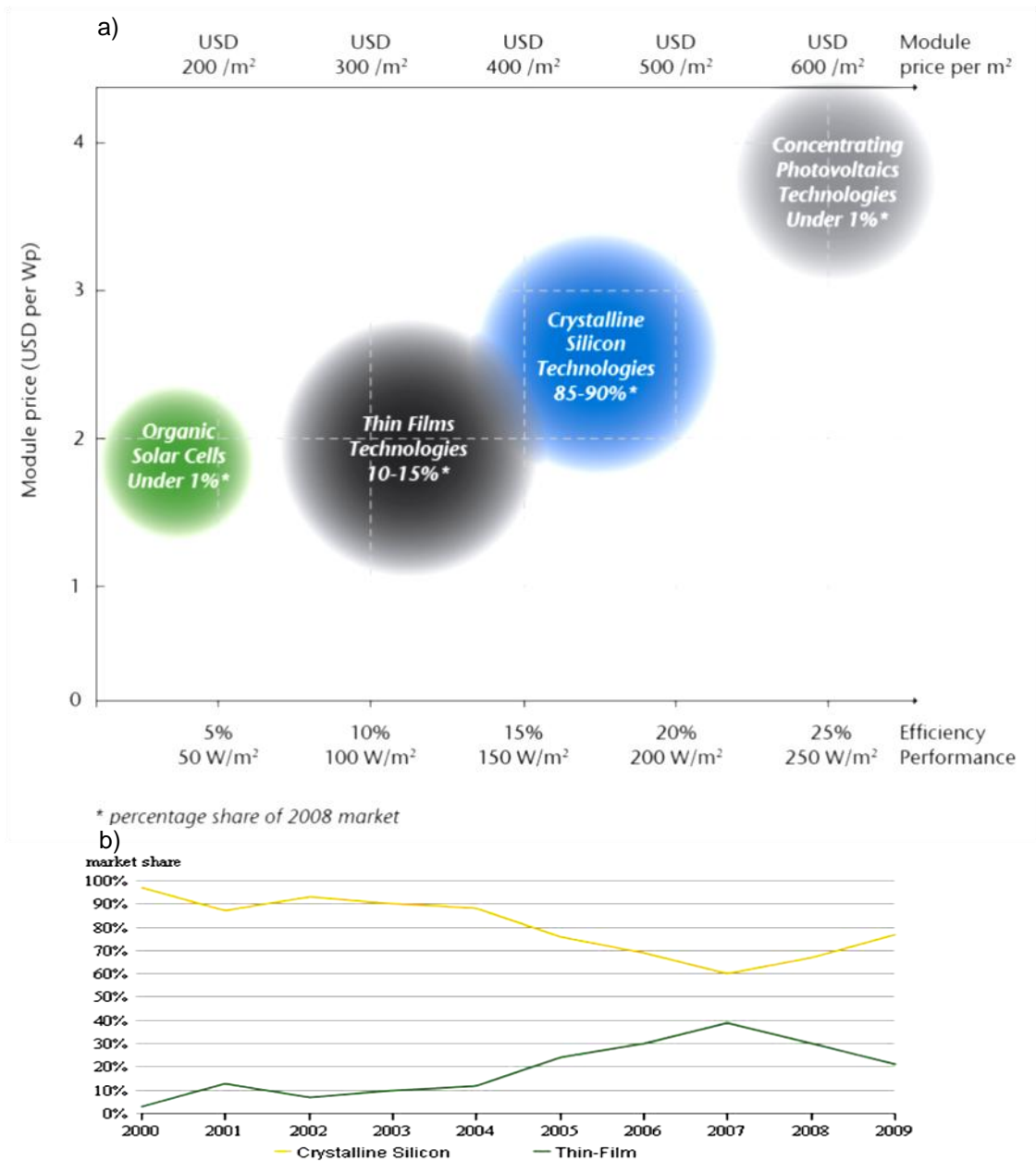


Figure 1.14 (a) Module price and efficiency estimates are compared according to the PV technology [28] (b) market share change of crystalline silicon and thin film solar cells [29]

1.3.1.3 Issues of commercial PV technologies

1.3.1.3.1 Crystalline Si solar cells

Since physics of this type of solar cells is similar to that of microelectronics, technical knowhow has already developed. As a result, improvements in the conversion efficiency side are not expected to be tremendous. Variation in the cost of cells and modules are shown in the Figure 1.15 [30]. Cost of the module dropped below \$3.0 for the first time in 2009. Although the technology works similar to microelectronics industry, the economics of the two industries are different. Focusing on process development and production scale-up have decreased the cost only linearly.

If we analyze the cost of a module and system 50% is the Si material cost due to highly energy intensive Si purification process, crystallization of Si and material waste during cutting into wafers. Also Si is a 1.1eV indirect band gap material which is smaller than optimum band gap of single junction cells 1.4eV.

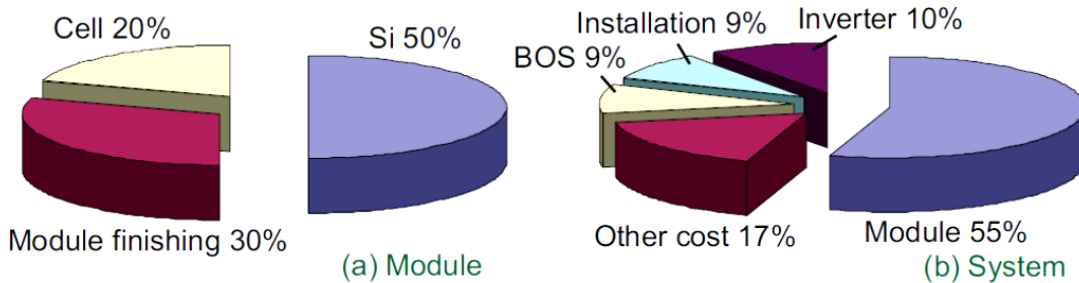


Figure 1.15 Cost breakdown for Silicon solar (a) modules and (b) systems [30]

Solar cell market were using scrap low cost wafer of microelectronics industry and this was limiting the supply of Si. Also there is inflation in the polysilicon price due to explosion in demand of Si, insufficient number of expertise companies, and capital and time investment during building of new plants.

1.3.1.3.2 Thin film solar cells

CdTe and CIGS are examples of this type of solar cells. The advantages of these cells are they require lower energy input compared to Si solar cells during production, and very low materials consumption per m^2 , automated monolithic series connection of cells such as laser scribing, and large-area deposition. There are fundamental problems that can prevent these technologies to skyrocket and they are; scarcity of In, Te and toxicity of Cd. Indium and tellurium have been estimated to limit total thin-film capacity to between 100 GW for CdTe (Feltrin & Freundlich 2008) and 30 TW for CIGS/CIS (Zweibel 2005) based on different estimates of rare metal supply. Indium has substitutes, but they usually lead to losses in production efficiency or product characteristics. Gallium can be used in some applications as a substitute for indium in several alloys. Also The United States has no primary indium or gallium production capacity, and most reserves are located in other countries. Semiconductor and electronics products and metal alloys are competing uses for tellurium. The tellurium required for CdTe PV has driven a fourfold price increase in the past 5 years; the market price increased from \$50/kg in 2004 to more than \$225/kg in August 2008.

1.3.1.3.3 Multijunction Concentrated Solar Cells

These are the highest efficiency and the most expensive solar cells. Due to their high cost they are used in special applications like concentrator solar cells.

1.4 Research Objective

Cost and energy input in silicon solar cells on one side and scarcity of In and Te in CIGS and CdTe thin film solar cells on the other side remain as two major challenges for terawatt-scale photovoltaic. Alternative photovoltaic materials that feature material abundance, low extraction and processing costs, and reasonable efficiency have to be found. In this respect, Ni-oxysulfide compounds are promising semiconductors because they have low extraction cost and high potential for terawatt-scale photovoltaic [31]. Depending on the stoichiometric ratio, the band gap of Ni-S can be adjusted from 0.35eV [32] to 1.3eV [33]. Electrochemical deposition

allows direct deposition on conducting substrate for good electrical contact and precise control of film thickness, in addition to low cost, low temperature, large area, and mature technology [34]. The objectives of this research are listed as follows:

1. Stabilizing the electrochemical deposition solution
2. Optimizing the variables of electrochemical deposition of Nickel sulfide for better quality films
3. Characterization of the compound and morphology of Nickel sulfide films by using SEM, XRD
4. Oxidizing sulfide films to replace some of the sulfur with oxygen in the structure in order to obtain Nickel oxysulfide compound with adjustable band gap
5. Optical characterization of mixed compound.

CHAPTER 2
BACKGROUND
2.1 Solar Cells

2.1.1 History of Solar Cells

Solar cells are basically electronic devices that convert photon energy from the sunlight to electricity. The conversion process is made possible by the photovoltaic effect, which was discovered by Becquerel in 1839. He observed a voltage between electrodes in an electrochemical cell when it was illuminated [36]. Although the first demonstrated solar cells in 1883 which were using Se semiconductor covered with a thin Au layer, over the next sixty years selenium and thallos sulfide solar cell efficiency remained at less than 1 % [37]. Then Si-technology emerged in the 1950s as a revolution. Solar cells with efficiency of ~6 % were developed in 1954 by Chapin, Fuller and Pearson at Bell laboratories [38] and their single-crystal Si based solar cells have been the basis of the photovoltaic device.

2.1.2 Solar cell device physics

Sun releases an enormous amount of radiant energy into the solar system. Temperature of the photosphere (surface) layer of sun is around 5800K which makes us approximate sun as a black-body radiator at this temperature. The Sun emits electromagnetic radiation, i.e. light in various wavelengths ranging from ultraviolet (UV (<400 nm)) to infrared (>800 nm). Solar radiation spectrum is illustrated in Figure 2.1 Solar spectrums at different air-mass condition Figure 2.1 [35]. Dashed curve shows extraterrestrial spectrum of sun's radiant energy at 5800K.

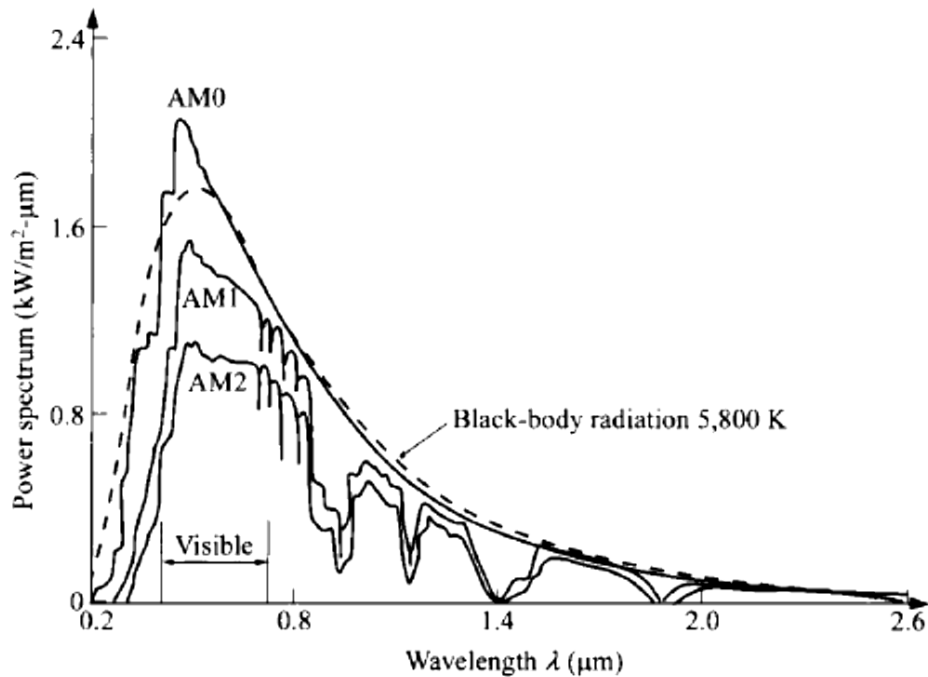


Figure 2.1 Solar spectrums at different air-mass condition

When solar radiation gets through earth's atmosphere it is attenuated due to scattering and absorption by air molecules, dust particles in the atmosphere. The degree of attenuation depends mostly on the travel distance of sunlight through the atmosphere. As a result solar radiation is redefined according to distance it traveled. Ratio of actual path length of sunlight to path length of sunlight when it is at zenith is called optical air mass. Air mass is calculated by the angle of the sun to the zenith according to the equation (2.1),

$$\text{Air mass} = (\cos\theta)^{-1} \quad (2.1)$$

AM 0 is described as the spectrum of solar radiation outside the earth's atmosphere. AM1 corresponds to the radiation of solar when it is at zenith, i.e. θ is zero. Solar radiation intensity and spectral distribution depends both on the location on earth and the position of the sun in the sky. In order to specify a standard in solar cell testing at different locations at earth, AM1.5 radiation ($\theta=48.2^\circ$) is selected. The actual irradiance is 827 W/m^2 at AM1.5. 1000 W/m^2 is close

to maximum irradiance received at earth's surface so peak power (watt) of a cell is expressed under conditions of AM1.5 $1000\text{kW}/\text{m}^2$.

Other than path that sun light traveled, local atmospheric and surface conditions are other factors that affect the actual amount of solar radiation reaches on a solar cell. Solar radiation can be divided by three components as direct, diffuse and albedo. Direct component of solar radiation is the sunlight that directly reaches to the solar cell. Diffuse component is sunlight reaching to solar cell after scattered in atmosphere. Sunlight reaching to solar cell after scattering from earth's surface is called albedo component of solar radiation. The total of these three components is called global radiation. Although it is written that world is exposed to several thousand times the total primary power demand, the difficulties come with the diffuse nature of solar energy and its being in wrong place at wrong time, not due to its shortage. The best locations on earth have a mean annual solar irradiance of $250\text{-}275\text{ W}/\text{m}^2$ on a horizontal surface and taking into account observed cloudiness [39]. This is a low power density in order to meet the demand of concentrated power demands in cities. Solar irradiance integration for a period of time is called solar irradiation.

Solar photovoltaic energy conversion is a one step conversion of light energy to electrical energy. Light is made up of energy packets, photons, and its energy depends on frequency of the light. When the light shined on a semiconductor it can be reflected, transmitted or absorbed. Transmittance is just passing through the semiconductor which occurs if the photons have energy lower than the energy band gap (E_g) of the semiconductor. Depending on the incident angle of the photon and the surface structure of the semiconductor some of the photons are reflected from the surface of the semiconductor. Transmitted and reflected light don't contribute to the generation of power in the solar cells. If the energy of a photon is sufficient to excite electrons (having energy higher than band gap of semiconductor) it is absorbed in the material and electrons go up to energy level in the conduction band and electron hole pair is generated. When the energy of a photon is higher than the band gap, the

difference between photon energy and E_g of semiconductor, is excess and wasted as heat through excitation of the lattice vibration. Normally when light is absorbed and electrons excited to higher energy states within the material they quickly relax back to their ground state. However, in a photovoltaic device built in potential difference separate electrons and holes before they can relax and drives them to the external circuit.

The length of a photon traveled before being absorbed depends on photons wavelength. The shorter wavelength of a photon, the closer to the surface it is absorbed and the longer wavelength photon is absorbed in a region further away from the surface. This is illustrated in Figure 2.2 . The degree to which photons are absorbed in the semiconductor is related to the optical properties of the semiconductor, such as the energy band structure. The indirect band gap semiconductor has a smaller absorption coefficient than a direct band gap semiconductor. This means solar cell with indirect band gap semiconductor absorber layer needs to be much thicker than direct band gap semiconductor in order to absorb the same amount of photons. Average photon absorption is the highest in the region close to the surface when solar irradiance spectra and band structure of semiconductor is considered.

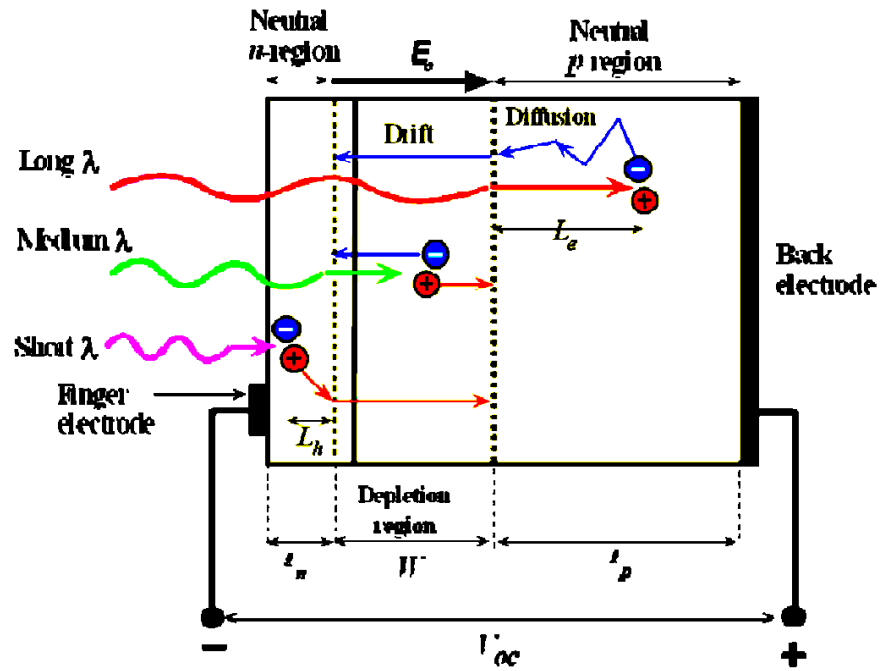


Figure 2.2 Cross-section of a p-n junction solar cell

All conventional photovoltaic devices are based on the p-n junction. A schematic of the cross-section of a conventional p-n junction solar cell and its energy-band diagram are shown in Figure 2.3.a and Figure 2.3.b, respectively. The charge carriers induced by light i.e. electron-hole pairs, is separated by two transport mechanisms. Drift is one of these mechanisms which is induced by internal electric field built in the depletion region. Diffusion by carrier concentration gradient in n and p regions is another charge separation mechanism. Since most of charge carriers are generated in the region close to the solar cell surface, separation of those carriers by internal electric field should be closer to surface as well in order to reduce the recombination of charge carriers. After separation, the charge carriers are finally collected at the corresponding metal contacts by diffusion.

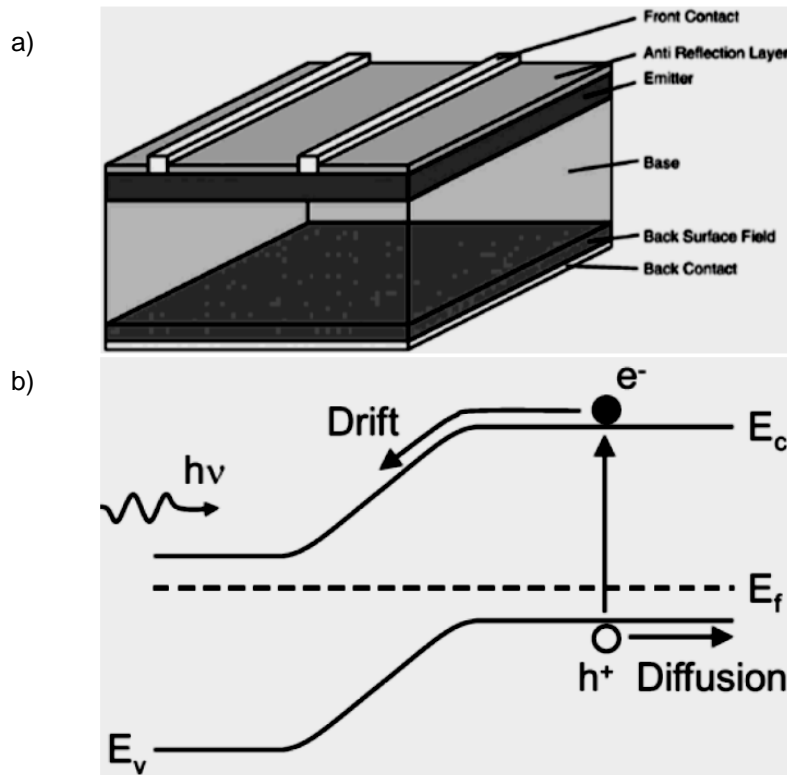


Figure 2.3 (a) Schematic of the cross-section of a conventional p-n junction solar cell and (b) its energy-band diagram

2.1.3 Important parameters in solar cells and device requirements

The performance of solar cells can be simply demonstrated by four device performance parameters including short-circuit current (I_{sc}), open-circuit voltage (V_{oc}), fill factor (FF), and conversion efficiency (η); and one cost parameter which is dollar per peak watt ($\$/W_p$).

The short circuit current is current through the solar cell when the voltage across the solar cell is zero. The short-circuit current is due to the collection of light-generated carriers. For an ideal solar cell, the short-circuit current and the light-generated current are equal. Therefore, the short-circuit current is the largest current that can be drawn from the solar cell. The short-circuit current depends on some factors such as the area of the solar cell, the number of photons (the power of the incident light source); the spectrum of the incident light, which is specified as AM1.5; the optical properties (absorption and reflection) of the solar cell, the

collection probability of the solar cell, which mostly depends on the surface passivation and the minority carrier lifetime in the base. To remove the dependence of the solar cell area, it is calculated as the short-circuit current density (J_{sc}) rather than the short-circuit current. The diffusion length and surface passivation become the most important parameters when solar cells of the same material type are compared. Under an AM1.5 spectrum laboratory silicon solar cells have measured short-circuit currents of over 42 mA/cm^2 , and commercial solar cell have short-circuit current densities between about 28 mA/cm^2 and 35 mA/cm^2 [40].

When a cell is operated in open-circuit, there is no current flow in the circuit. The voltage between two terminals of load is called open-circuit voltage, V_{oc} . So V_{oc} is the maximum voltage available from a solar cell. Solar cell junction is biased with the light-generated current and V_{oc} is the amount of forward bias on the solar cell. V_{oc} depends on the saturation current of the solar cell and the light-generated current. I_{sc} changes slightly but the saturation current can vary by orders of magnitude since I_0 depends on recombination in the solar cell. As a result open-circuit voltage becomes a measurement of the amount of recombination in the device. In order to give an idea, high quality single crystalline solar cells have open-circuit voltages of up to 730 mV under one sun and AM1.5 conditions, while V_{oc} of multicrystalline silicon commercial devices are around 600 mV [40].

Although the short-circuit current is maximum current and the open-circuit voltage is the maximum voltage from a solar cell, at both of these points the power from the solar cell is zero. The fill factor, FF, is the ratio of the maximum power from the solar cell to the product of V_{oc} and I_{sc} . It determines the maximum power from a solar cell in conjunction with V_{oc} and I_{sc} . Geometrically, the FF is a measure of the squareness of the I-V curve and it is the largest area of a rectangle that will fit in the I-V curve. FF's for Silicon laboratory device, typical commercial solar cell and GaAs solar cell are 0.85, 0.83 and 0.89 respectively. All terms described above are shown in Figure 2.4.

$$FF = \frac{I_m V_m}{I_{sc} V_{oc}} \quad (2.2)$$

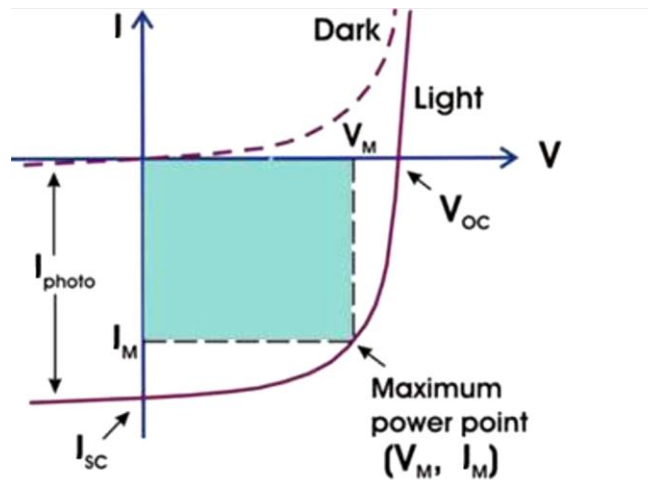


Figure 2.4 Current- voltage characteristic of a solar cell under illumination

Maximizing output power, i.e. $FF \cdot I_{sc} \cdot V_{oc}$, requires large I_{sc} and V_{oc} . V_{oc} increases with band gap, i.e. increase built in potential, while I_{sc} increases with small band gap to absorb as much as photons as possible. As a result 1.4 eV is found to be the optimum band gap for single junction solar cells [41].

The efficiency the ratio of energy output from the solar cell to input energy from the sun. The efficiency depends on the performance of the solar cell spectrum, intensity of the incident sunlight and the temperature of the solar cell. Therefore, conditions under which efficiency is measured are controlled at 25°C and AM1.5 ($1000\text{W}/\text{m}^2$) in order to compare the device performance. The equation for efficiency is given as 2.3.

$$\eta = \frac{I_{sc} V_{oc} FF}{P_{in}} \quad (2.3)$$

Since the amount of received sunlight changes with time; the power supplied varies. To accommodate the variation in power production, peak watt term (Wp) is used. Peak Watt is the amount of power that a PV module is able to supply when it receives 1000 W/m^2 of solar irradiance. The ultimate comparison of PV should include the cost. That is possible by simply dividing total capital cost for the device by the Wp it can produce.

After describing the important parameters the device requirements can be specified. High carrier mobility, good crystal quality for high minority carrier lifetime, direct band gap for high absorption coefficient, 1.4 eV for single-junction cells, ability to control conduction type, ability to control conductivity, and finally cheap and abundant source of materials with a non-energy intensive production process are required for PV device.

2.2 Solar cell absorber materials

Table 2.1 lists the desired properties and commercial semiconductors that satisfy them [42]. As a most widely used semiconductor, Si is abundant and non-toxic but it requires high amount of energy to purify it from quartz to semiconductor grade silicon. Covalent bonding crystalline Si makes Si wafer production process expensive and energy intensive, since directionality of covalent bonding cause solution methods result in degradation of electrical properties of these materials. Crystalline Si band gap is indirect which requires higher thickness in the wafers to absorb more sun light and this again results in a cost increase. Also it is hard to cut through the wafers from ingots. The current wafer thickness is $\sim 200 \mu\text{m}$ and decreasing it to $100 \mu\text{m}$ or less needs advanced wafer cutting and handling technologies since they will be very weak and will need mechanical support. String ribbon process is developed to decrease the amount of Si by half in production of crystalline Si wafer, but it is not capable of achieving the same electrical performance as conventional wafer technology. Typically a cut wafer have a conversion efficiency of 15-16% of the incoming light into electricity where as string ribbon solar cells have 13-14% efficiency. Also the overall thickness varies during manufacturing process as a result not every strip can be used in solar cells. In addition to these drawbacks, the radiating

area/gram of crystal is high, which makes the growth process thermally very inefficient and high energy density, eventually offsetting the reduced silicon use/expense. In order to reduce the cost of cells, PECVD is used to produce amorphous Si. This has very poor electrical properties compared to crystalline Si due to inherent property of covalent bonding in Si causes any atomic misalignment leading to strained bond or dangling bond. As a result defect density becomes high and carrier mobility drops to $1 \text{ cm}^2\text{V}^{-1}\text{s}^{-1}$ compared to $450 - 1,500 \text{ cm}^2\text{V}^{-1}\text{s}^{-1}$ in sc-Si.

Most III-V group compounds such as GaAs, InGaAs etc. are direct band gap semiconductor and can achieve higher efficiency thin film solar cell. But their drawbacks are scarcity of most group III and V elements, and high processing cost. But these kinds of solar cell have wide application in the spacecrafts due to their high efficiency.

Table 2.1 Material requirements for terrestrial solar cells [42]

Material Requirement	Material Meeting Requirement
Abundant material	Si
Low-cost materia	CdTe, CIGS
Low-cost synthesis	CdTe, CIGS
Non-toxic material	Si, CIGS
Stable material	Si, III-IV, CdTe, CIGS
High mobility	Si, III-IV, CdTe, CIGS
High carrier lifetime	Si, III-IV
Suitable band gap	III-IV, CdTe, CIGS
Control of conduction type	Si, III-IV, CdTe, CIGS
Control of resistivity	Si, III-IV, CdTe, CIGS

CdTe and CIGS satisfy low cost processing due to their non directional type of bond, i.e. ionic bond. These materials fail in terms of meeting abundance, low cost material and non-toxicity requirements. Although these chalcogenides have shown some promising properties, it is important to develop systematic design principles that accelerate the discovery of novel materials with lower cost and higher efficiency to satisfy the need for wide-range photovoltaic

deployment .In addition to cost, we must also consider abundance and environmental impact of the elemental components. These criteria should be improved for current thin film absorber materials, e.g. the scarcity and high cost of indium and gallium in $\text{Cu}(\text{In,Ga})(\text{S,Se})_2$ based cells and the high toxicity of cadmium in CdTe based cells [44].

2.2.1 Solar Cell Material Requirements

Requirements that should be met by a perfect semiconductor for single junction solar cell are being abundant for TW scale deployment; low cost, energy efficient synthesis; having 1.4 eV direct band gap, low carbon emission during fabrication; minimum environmental impact; and being stable under terrestrial conditions. Meeting all requirements by a single semiconductor remains a challenge. As a result, for a third generation solar cell a suitable material should be abundant, synthesized by wet chemistry and have excellent and controllable electrical properties. Systematic approach should be followed to seek a material which can be produced with soft chemical methods without introducing defects during manufacturing. This approach includes evaluation of bonding types in materials to relate production process and electrical properties of materials.

Most semiconductors are covalent or mixed covalent and ionic. Ionic solids are compounds composed of atoms having large electronegativity differences, i.e. strongly electronegative group (VI and VII) with strong electropositive counterpart. Complete charge transfer condition is called closed shell model. In an ionic bond cation gives electron to the anion; this then creates an electrostatic attraction between cation and anion resulting in a very strong ionic bond. Since the ionic bonding is based on Coulombic interactions it is non-directional which is due to a positive ion attracts adjacent negatively charged ion in all directions equally, thus bond angle is not rigidly fixed. This bonding flexibility has an effect on structure of material and it allows small atomic misalignment to be accommodated in the crystal without introducing a defect [42].

Covalent bonds are formed by sharing of valence electrons between neighboring two atoms. Such sharing nature of bonds is highly directional resulting in rigidly fixed bond angle and length. The bonding in Group IV semiconductors (Si, Ge) is covalent with equal sharing of outer electrons. Each silicon atom is bonded to 4 other silicon in a tetrahedral covalent bond, which determines the diamond cubic crystal structure. This leads to any atomic misalignment in the Si network strains bond. A dangling bond is created when the misalignment is large. Carrier mobility and minority carrier lifetime in inorganic semiconductors having only covalent type of bonding like Silicon are easily degraded by any atomic misalignment, strained and dangling bonds.

In many compounds that form covalent solids the electrons are not shared equally between atoms and this leads to partial ionization and mixed ionic and covalent bonding. This type of bonding is present in group III-V (GaAs) and group II-VI (CdTe) compounds since sharing of outer electrons are unequal [43]. This makes most inorganic structures more complex than metals or semiconducting elements. We can also observe this phenomenon in ionic solids. When ions have high polarizability due to high average quantum number, the electric field of adjacent ions changes the ion size, induces dipole and this leads to interpenetration of electron clouds. In order to estimate degree of ionicity, a theory of fractional band ionicity developed by Phillips. Fractional band ionicity is given in Table 2.2 for selected semiconductors and in most of them bonding is described by combination of ionic and covalent [43].

Table 2.2 The fractional bond ionicity, f_i , for selected semiconductors

Semiconductor	$f_i(\%)$
Ge	0
Si	0
SiC	17.7
GaAs	31
GaP	32.8
InAs	35.9
ZnS	62.3
CdTe	65.7
CdS	67.9

In order to achieve production of perfect semiconductors by solution techniques, the semiconductor should have high degree of ionicity which will make it resilient in terms of manufacturing conditions by allowing small atomic misalignment to be accommodated without introducing an electronic defect. Although ionic bonding is desirable in terms of getting better crystallinity by wet chemical methods, the band gap of semiconductor increases when the ionic character of its bond increases. This can be explained as increase in localization of electrons near nucleus makes those electrons more difficult to become a mobile charge carrier. Also highly ionic I- VII compounds are soluble in water. So there is a trade-off between ionic and covalent bonding in the desired inorganic semiconductor. In this regard, semiconducting transition metal chalcogenides stand out as most promising inorganic semiconductor materials for 3rd generation solar cells whose band gap is tunable by changing its stoichiometry and ratio of covalent-ionic bonds. According to inorganic nomenclature chalcogen refers to group 16 elements in periodic table including oxygen, sulfur, selenium, tellurium and polonium, and metal chalcogenides refers to their compound with metals. The name is generally considered to mean "ore former" from the Greek *chalcos* "ore" and *-gen* "formation". Metal chalcogenides range from common oxides, sulfides and selenides to complex compounds containing different chalcogen compounds in changing proportions. Among all the chalcogens we are particularly focused on sulfides and oxides since they are abundant in nature. The characteristics of metal sulfides and oxides will be discussed first.

2.2.2 *Metal Sulfides and Oxides*

Almost all metal sulfide minerals are crystalline solids. Representation of these solids is usually done by ionic modeling that considers ions as charged species with particular radius. Although oxides that show constancy of average interatomic distance for a particular ion from one structure to another, sulfides doesn't show constancy of ionic radii since sulfides doesn't sufficiently ionic in character. Sulfur has higher average quantum principal number than oxygen

which increases its polarizability in ionic compound. This result in more covalent bonding in sulfides, in other words ionicity is higher in oxides. Bond length of sulfur is also higher than oxygen which is inversely proportional to bond strength. As a result, stronger metal sulfide covalent mixing and the larger size of sulfide ion distinguish sulfide compounds from oxides [4].

When ionic character of a single bond increases, the electrons are becoming more and more localized near one nucleus, which makes it more difficult to free that electron to become a mobile charge carrier (conducting). This translates to a larger band gap in an extended solid (Table 2.3) [46].

Table 2.3 Effect of polarity of covalent bonding on band gap of compounds [46]

Material	Lattice Parameter, Å	ΔEN	E_g , eV (λ , nm)
Ge	5.66	0.0	0.66 (1900)
GaAs	5.65	0.4	1.42 (890)
ZnSe	5.67	0.8	2.70 (460)
CuBr	5.69	0.9	2.91 (430)

Although the lattice parameters of the compounds listed above are essentially the same, increase in polarity of covalent bonding (increase in ionic character of the bonds) resulted in increase in band gaps. Since the band gap, E_g , decreases with increase in bond strength and increase with charge transfer (ionicity), generally oxides have higher band gap than sulfides.

Ternary semiconductors exhibit more flexible properties arising from their enhanced chemical and structural freedom. In order to obtain optimum band gap there are three ways that can be followed. One is cation alloying of M_xS_y which has band gap higher than 1.4eV with N_aS_b which has band gap lower than 1.4eV to get a structure which will have $M_{x-z}N_zS_y$. Second approach is to use mixed-valence metal oxides. A transition metal has multiple valences in its oxides due to the unpaired electrons in its d shell. For example, Cu has a 2+ valence in Cu_2O which has a direct band gap of ~2.0 eV [69], whereas the valence of Cu in CuO is 1+. By mixing Cu_2O and CuO in the right ratio, a 1.4-eV band gap can be obtained. The same approach can

be used to other metal oxides. Third way is creating new structure with anion substitution. Specifically it is combining M_xS_y with O and getting a ternary compound of $M_xS_{y-z}O_z$. Since generally sulfides of a metal have band gap below 1eV and most metal oxides have band gaps well above 2 eV. Combining oxides and sulfides to match the solar spectrum for maximum efficiency, the semiconductor would ideally have a direct band gap of 1.4 eV for single-junction cells [47]. Figure 2.5 is an example of band gap engineering with changing sulfur concentration in Titanium Oxysulfide and Ge Oxysulfide material [54,143].

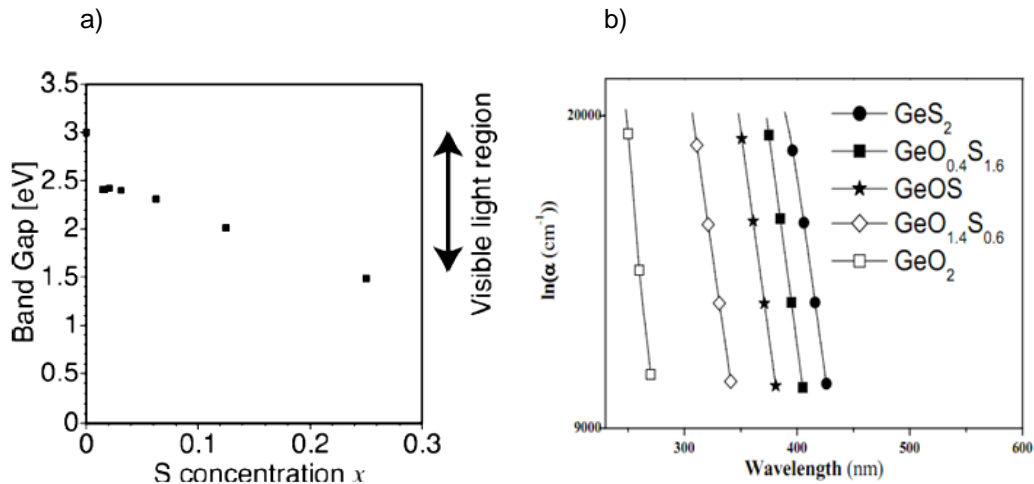


Figure 2.5 Band gap change with variation in sulfur concentration in (a) Titanium Oxide and (b) Ge Oxide [54,143]

Among these three ways anion alloying is studied in this project. The reasons behind standing away from first two routes are, doping of cation alloyed compound with another metal becomes problematic since structure will be very complex to control with three different metals existing in one structure, and large scale production of thin films from this type of compound may include sulfur deficient places which will result in metalized region that will short the device.

Producing oxysulfide compound is not an easy task however, due to complex bonding interactions in sulfides. The outer electron configuration of sulfur (3s23p4) causes a possibility

of more diffuse and more delocalized bonding in sulfides than in oxides. The degree of delocalization depends on the composition of sulfide and on its stereochemistry. For example, metal-metal interactions in metal sulfide influences bond distances and radii values of metal-sulfur bonds [74]. As a result, each sulfide has a different sulfur ion bond length and brings difficulties in terms of theoretical predictions.

Prospective metals for the metal oxysulfide compound are selected according to their abundance, and band gaps of their sulfides and oxides. Material Research Society released a report that shows the critical elements in terms of energy. These include rare earths, elements occurring in a few economic deposits worldwide, elements produced by one or more countries which are subject to manipulation. These elements will be subjected to special action by US to insure their availability such as market interventions, efficiency use of materials and recycling. These elements are highlighted in the Figure 2.6.

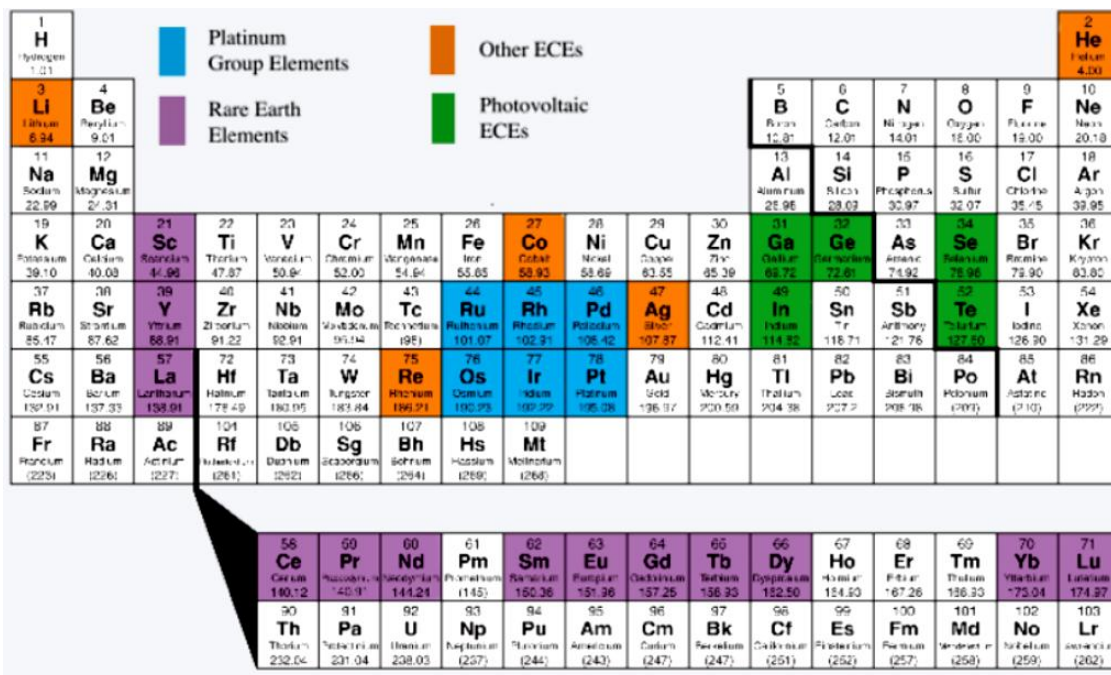


Figure 2.6 Possible energy-critical elements are highlighted on the periodic table [21]

It can be inferred from Figure 2.6 that Se and Te are not promising elements for utilization of chalcogen anions in photovoltaic applications. Transition metal oxides and sulfides (excluding energy critical elements) such as Ti, Cr, Fe, Ni, and Cu, W are investigated in terms of their typical band gap. After an exhaustive literature search, Table 2.4 is compiled, which lists the band gap values and reserves for several metal oxides and sulfides. It should be noted that the reported band gap values, conduction type, and direct or indirect transitions for metal oxides and sulfides change and show dependence of deposition condition. For example for CuO, it varies between 1.2–1.9 eV [57, 58, 59, 60, 61], which reflects huge effect of structural variations on optical properties and our limited knowledge about these materials.

Table 2.4 Band Gap Values for Several Metal Oxides, Sulfides

	Ti	Ni	Cu		Fe	W
Sulfide	TiS ₂ ^[64] 0.3±0.2eV	NiS ^[67] 0.45eV	Cu ₂ S ^[68] 1.2eV		FeS ₂ ^[70] 0.95eV	WS ₂ ^[71] 1.3eV
Oxide	TiO _{x=1-2} ^[65] 0-3.5eV	NiO ^[63] 3.8eV	CuO ^[69] 1.4eV	Cu ₂ O ^[69] 2.0eV	Fe ₂ O ₃ ^[63] 2.2eV	WO ₂ ^[72] 2.6eV
Oxy-sulfide	TiO _{1.5} S _{0.5} ^[66] 1.5eV	-	-		-	-
World Reserve (tons)	690x10 ⁶ [73]	76x10 ⁶ [73]	630x10 ⁶ [73]		87x10 ⁹ [73]	2.9x10 ⁶ [73]

Although Cu, Ni, Fe, Ti and W seem to be promising to form desired compound according to the Table 2.4 above, we need a detailed inspection of properties of each metal compound.

CuO seems to have 1.4 eV direct band gap but its crystal structure is monoclinic. Monoclinic crystal structure leads to a poor microstructure which degrades mobility of the semiconductor. Also its resistivity is high ($1.26 \times 10^3 \Omega\text{cm}$).

Transition-metal dichalcogenides (TMDC) like MoS₂ and WS₂, are all semiconductors of great interest as absorbers for thin-film solar cells due to their band gaps in the range of 1–2

eV and the extraordinarily high absorption coefficients, exceeding 10^5 cm^{-1} . Their problem however is low photoactivity mainly caused by crystallization in the molybdenite structure. This means that the building units of the TMDCs are two-dimensional, strongly bonded S-Me-S layers, which are weakly bonded to each other by van der Waals forces along the c-axis of the unit cell. This is similar to layer-type materials graphite. The semiconductor tungsten disulfide (WS_2) reported as an absorber layer for thin-film solar cells by Jäger-Waldau et al. with an efficiency below 1% (<0.31%) [28]. The photoactivity is poor due to their intrinsic properties like low defect formation energy, especially sulfur vacancies that generates lattice defects during the growth which leads to recombination centers [56].

Pyrite ($E_g=0.95\text{eV}$) has been studied as a solar energy material due to its environmental compatibility and its very high light absorption coefficient. But it has been long time from the time pyrite was used as a rectifier in early radios, and some of its semiconducting properties were investigated. From these studies it is concluded that pyrite was a difficult material to study because of its inherent stoichiometric problems. It is hard to control stoichiometricity of film. Iron sulfide (FeS_2) has unavoidable metallic secondary phases and surface defects coexisting near the FeS_2 thin-film surfaces and grain boundaries that limit its open-circuit voltage [75].

As a result, among the prospective transition metal chalcogenides listed in Table 2.4, Nickel Sulfide and oxide will be discussed in this thesis.

2.3.3 Nickel Sulfides and Oxides

Nickel sulfide compounds present several stoichiometry, and they are stable under different thermodynamic conditions. Also, in the presence of O_2 , the sulfur atoms can be quickly replaced by O atoms to form nickel oxide. Thus, nickel sulfides display a complex behavior and more detailed and systematic studies are required to understand their properties [76]. A number of NiS_x minerals with different Ni/S ratios have been reported, the four nickel sulfides that have relatively higher stability than other forms are millerite (NiS), vaesite (NiS_2), nickel rich

compound heazlewoodite (Ni_3S_2), and polydymite (Ni_3S_4) [75]. Ni_3S_2 has a stable rhombohedral structure [77, 78, 79], NiS a hexagonal structure [80, 81, 82]; and Ni_3S_4 and NiS_2 cubic structures [83, 84, 85, 86, 87, 88]. The crystal structures of Ni_3S_2 , NiS , Ni_3S_4 , and NiS_2 are illustrated in Figure 2.7. In Figure 2.7 a, heazlewoodite Ni_3S_2 has a rhombohedral (nearly cubic angle 89.4 and $a=4.09$) structure [77], where S atoms form a slightly distorted body-centered cubic array with Ni atoms occupying the distorted tetrahedral interstices. At temperature above 556 °C, it converts to $\text{Ni}_{3+x}\text{S}_2$, with an fcc structure and in this phase a substoichiometric number of metal atoms are randomly distributed in a cubic close packed structure of sulfur atoms with vacancies. [92]. Figure 2.7 b millerite (NiS) is shown. It has a hexagonal structure, where three Ni atoms form a triangle and five S atoms locate in the corners of a square pyramid. In Figure 2.7, polydymite Ni_3S_4 has two types of Ni atoms and one type of S atoms, $\text{Ni}^{\text{I}}\text{Ni}^{\text{II}}_2\text{S}_4$, in a cubic structure. In Figure 2.7, pyrite NiS_2 has a cubic structure, where the Ni atoms occupy the sites in the face centered-cubic sublattice.

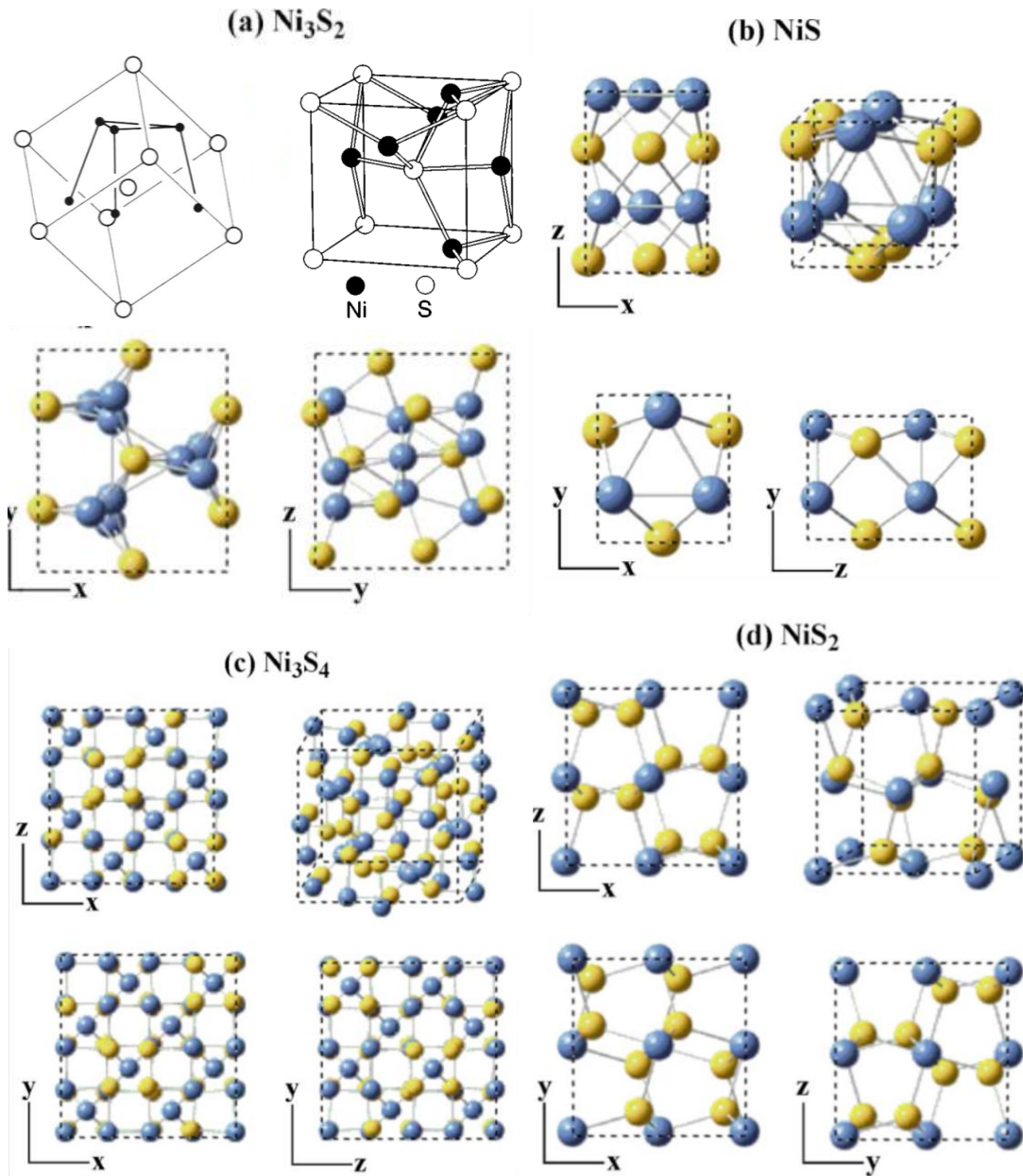


Figure 2.7 Crystal structures of Ni_3S_2 , NiS , Ni_3S_4 , and NiS_2 from different perspectives. Blue and yellow balls are represented as Ni and S atoms, respectively [2]

The phase relations of Nickel Sulfides in the range of Ni_2S to NiS are shown in the Figure 2.8 [136]. Rhombohedral Ni_3S_2 decomposes to $\text{Ni}_{3\pm x}\text{S}_2$ cubic phase which consists of nickel-rich β_1 and sulfur-rich β_2 phases around 833K in evacuated environment. $\text{Ni}_{3\pm x}\text{S}_2$ is a

structure with an fcc structure and in this phase a substoichiometric number of metal atoms are randomly distributed in a cubic close packed structure of sulfur atoms with vacancies [136].

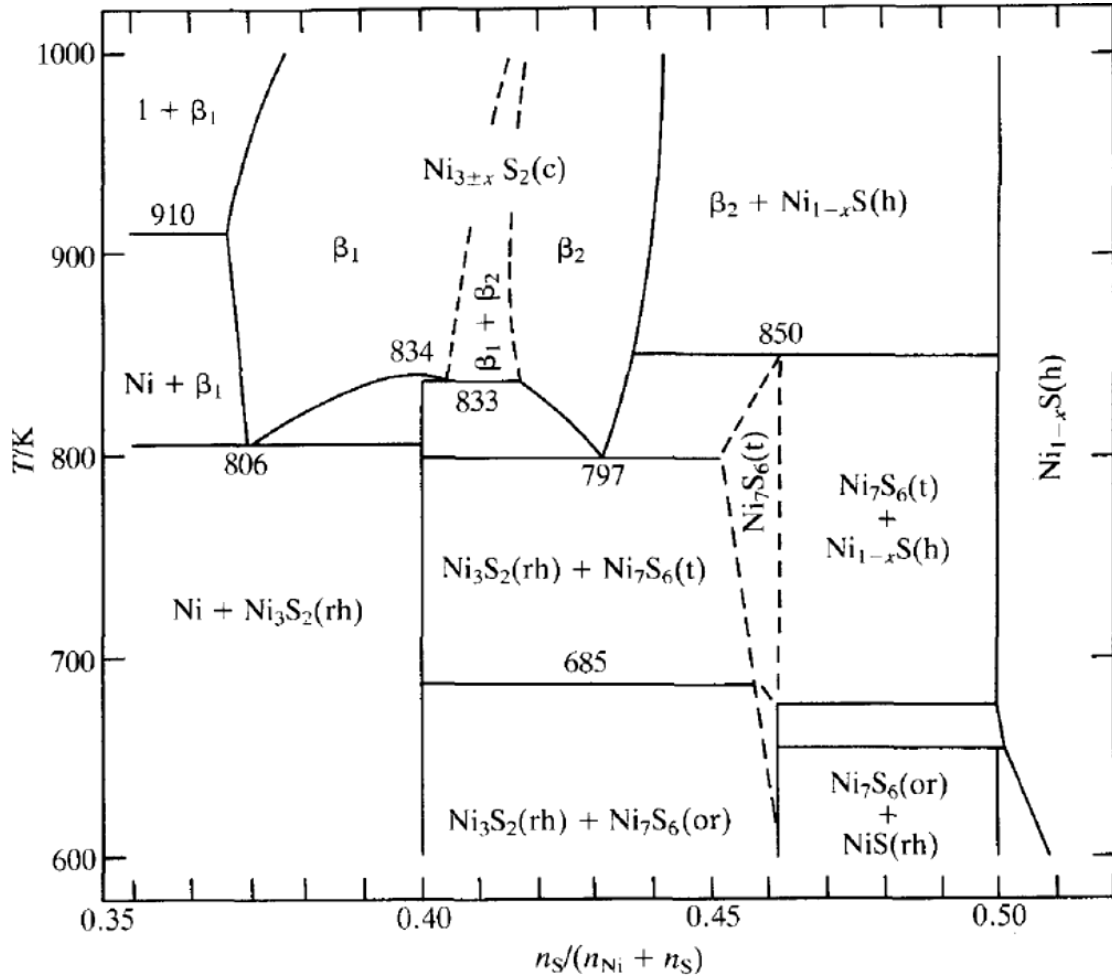


Figure 2.8 Phase diagram of Ni-S [136]

The electronic structure analysis indicates that all Ni-S bonds are strongly covalent. The reported bandgap for NiS is 0.8 eV [93] and 0.35 eV [94] by different groups. Similarly, the bandgap for NiS₂ is 0.33 eV [95] and 1.3 eV [96], respectively. NiS_x is a degenerate semiconductor with almost metal-like conductivity [90]. The bandgap for Ni₄S₃ is 0.35 eV [97]. Examining the charge distribution reveals metallic as well as fairly strong covalent bonding in

Ni₃S₂ [89]. Therefore, the properties of these films are scattered around from metallic to semiconducting, depending on the Ni/S ratio in the film.

Nickel sulfide (NiS) films prepared by solution growth on glass [98] or polymer substrates [99] by Pramanik et al. Anuar et al. electrodeposited (NiS) [100]. Other methods for Nickel Sulfide film deposition are successive ionic layer adsorption and reaction (SILAR) [101], laser ablation [102] and hydrothermal (Ni₃S₂, NiS) [103] soft solution-processing (NiS, Ni₃S₂, NiS₂, Ni₃S₄) [104] and CVD methods (NiS, NiS₂, Ni₇S₆) [105, 106, 107, 109].

Nickel oxide (NiO) is a NaCl-type transition metal oxide semiconductor. Nickel oxide is a high band-gap semiconductor with the absorption edge in the UV region and no absorption in the visible region. The reported optical band-gap of NiO ranges from 3.4 eV [110] to 4.3 eV [111] (direct band gap) depending exactly on how the location of the band edge is defined: location of the first absorption feature, midpoint of the first rise, or where the maximum slope of absorption extrapolates to zero [111]. The presence of Ni³⁺ ions in the oxide lattice causes absorption in the visible region [112]. The presence of Ni³⁺ ions can be explained by Ni₂O₃ is present as a minority phase that could not be detected by XRD, presence of nickel vacancy caused two adjacent divalent nickel ions become Ni³⁺ due to charge transfer process or stoichiometry of the film is NiO, but excess oxygen together with the hydrogen may be present in the film as OH groups [113]. Nickel oxide thin films have been prepared by various techniques such as, vacuum evaporation [114], electron beam evaporation [115], rf-magnetron sputtering [116, 117], anodic oxidation [118], chemical deposition [119, 120, 121], atomic layer epitaxy [122], sol-gel [123]; and spray pyrolysis (SPT) [124, 125, 126].

2.3 Deposition Methods

NiS_x films have been prepared by several techniques. Vapor-phase techniques include chemical vapor deposition, either thermal [128], photochemical [128], or low pressure metallorganic [129], and physical vapor deposition such as pulsed laser ablation [130]. Vacuum processes are atom by atom or molecular by molecular at below atmospheric pressure on a

solid state substrate. Since it is achieved in a closed ambient, roll to roll processing is not applicable. On the other side, more uniform and higher quality film can be produced than solution-based methods. Beside vacuum deposition, solution based deposition is also largely used for Nickel Sulfide thin film synthesis. Compared to vacuum deposition, the advantages of solution-based depositions are low temperature, atmospheric pressure, low cost and large scale capability. But film uniformity and quality are some of problems faced by manufacturer. Solution-based techniques include chemical bath deposition using both acidic and alkaline solutions. Alkaline solutions contain NiSO_4 and thioacetamide ($\text{C}_2\text{H}_5\text{NS}$) [94], while acidic solutions contain NiSO_4 and sodium thiosulfate ($\text{Na}_2\text{S}_2\text{O}_3$) [93]. Ionic layer-by-layer deposition is also solution-based with an alkaline solution containing NiSO_4 and Na_2S [101]. Hydrothermal growth is another solution-based technique with $\text{Ni}(\text{NO}_3)_2$ and elemental S as the precursors [104].

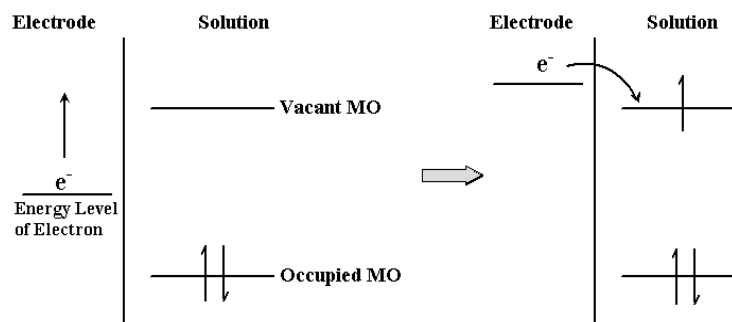
In addition to low cost and mature technology, electrodeposition has several advantages over other solution-based techniques discussed above. Electrodeposition requires a conducting substrate and the good electrical contact between film and substrate is important in photovoltaic devices. It also allows precise and in-line control of the film thickness [131]. In principle, each electron transfer in an electrochemical process leads to a chemical reaction. Therefore, the internal quantum efficiency in an electrochemical process is 100%, although resistive loss in external circuits brings down the overall efficiency. Therefore, electrochemistry significantly reduces the electricity input into a semiconductor production. Electrodeposition of NiS_x was studied by Anuar et al. [96] in a solution containing nickel tartrate ($\text{C}_4\text{H}_4\text{NiO}_6$) and $\text{Na}_2\text{S}_2\text{O}_3$. Recently, Sun et al. [132] used a periodic potential reversal technique to deposit NiS films.

2.3.1 Electrochemical deposition

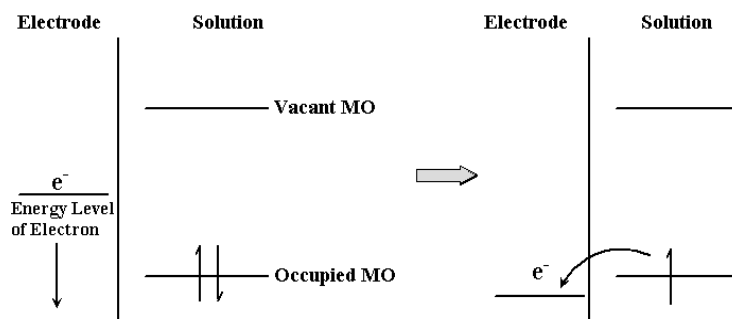
An electro-deposition is carried out by passing an electric current between two or more electrodes separated by an electrolyte. This deposition takes place at the electrode-electrolyte interface. Three electrodes electrochemical cell is usually used for electrodeposition. These

electrodes are working, counter and reference electrode. Selection of electrode materials depends on the purpose. Pt due to its inert nature, graphite and glass carbon can be used as a counter electrode. The reference electrode has stable and well-known potential. The basis of reference electrode is defined by setting standard hydrogen reduction potential as 0 V. In research facilities saturated calomel electrode (SCE) and silver chloride electrode are used due to its low cost and easy manipulating. The working electrode should be a conductive material such as metal, semiconductor. The conductivity of the working electrode affects the reaction rate. Also good adhesion between the substrate and deposited material is another parameter in selection of working electrode.

The overall electrochemical reaction in a cell consists of two independent half-reactions. Most of the time one is interested in the half-reaction occurring at the working electrode (WE). The potential of the working electrode is observed or controlled with respect to a reference electrode (RE). Since the reference electrode has a constant makeup, its potential remains fixed. Figure 2.9 shows how reactions are controlled by the potential applied to the working electrode. When negative potential is applied to the working electrode, energy of electrons in working electrode is increased. At certain potential, electrons will transfer to the vacant electronic states of the species in the solution. Therefore, a cathodic current is formed by flow of electrons from working electrode into solution. The electrons accepted by the species at the surface of the working electrode in the solution are reduced. Similarly, when a positive potential is applied, energy of electrons in working electrode will be lowered. At certain potential, electrons will flow from solution species to working electrode and form an anodic current, which results in the oxidation of the species in the solution. The critical potential, at which the electron flow, i.e. reaction happens, is called the standard potential (E^0) for the related species in the solution.



(a)



(b)

Figure 2.9 (a) Reduction, (b) Oxidation process of a species in solution [127]

An electrode reaction is a heterogeneous reaction since it includes solid and liquid at the interface of electrode and electrolyte. Generally, an electrode reaction includes four steps which are demonstrated in Figure 2.10:

1. Mass transfer (reactive species transferred to electrode surface)
2. Electron transfer at the electrode surface
3. Chemical reactions preceding or follow the electron transfer
4. Other surface reactions, such as desorption or adsorption

Therefore, an electrode reaction will not be only controlled by potential. Many other factors have effect on it as shown in Figure 2.11 [127].

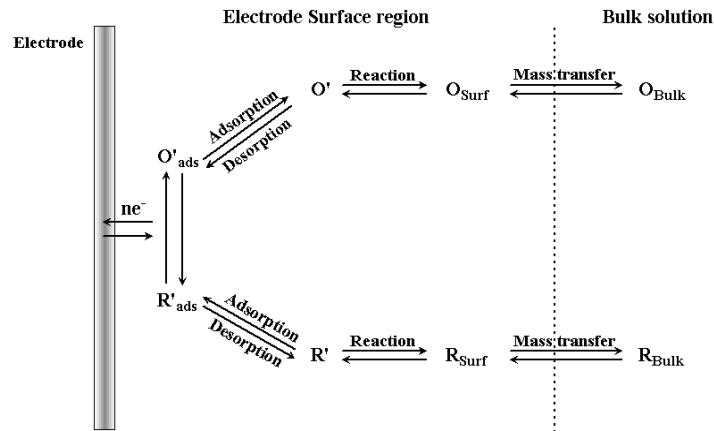


Figure 2.10 Pathway of a general electrode reaction [127]

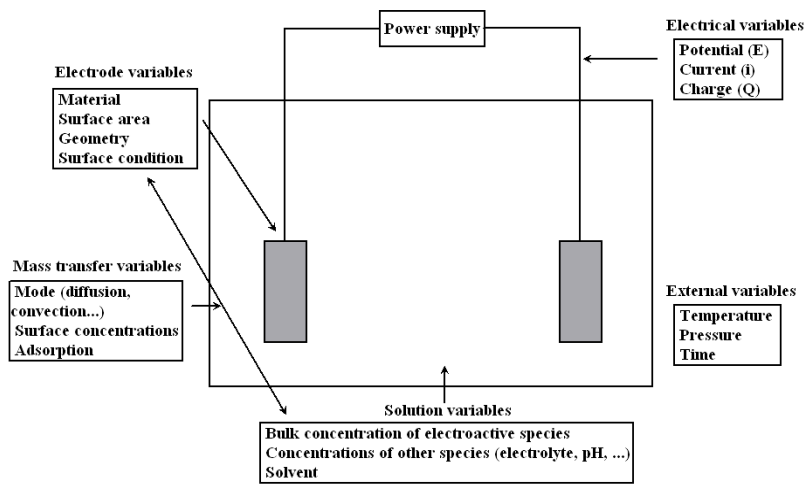


Figure 2.11 Variables affecting the electrode reaction [127]

Nowadays, instead of a two electrode cell (WE and RE), a three-electrode cell is preferable. A counter (or auxiliary) electrode (CE) is placed into the cell and current will flow between working electrode and counter electrode (instead of reference electrode). Reference electrode is placed near the working electrode surface. The device used to observe or control the potential difference between working electrode and reference electrode generally has very high impedance, so that a negligible current is flowing through the reference electrode. Therefore, its potential will remain constant.

2.4 Characterization Methods

2.4.1 UV-Vis transmittance spectrum and band-gap calculation

All UV-Vis transmittance spectra are measured with a V570 Spectrophotometer from Jasco Co. The schematic V570 Spectrophotometer is shown in Figure 2.12.

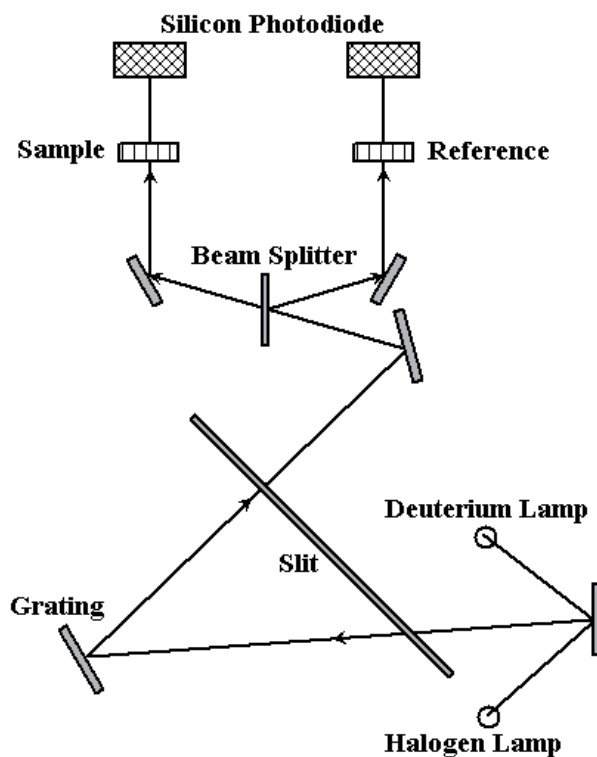


Figure 2.12 Schematic of V570 Spectrophotometer

Light with wavelength of 400 nm-1100 nm is generated by a halogen lamp and a deuterium lamp. Then the light is divided into two equal-intensity beams and one passes through a prepared sample and other through a reference sample. A silicon photodiode is used to record the intensity of the transmitted light.

From a UV-Vis transmittance spectrum, optical properties of as deposited and oxidized Nickel sulfide films are studied. The band-gap of a semiconductor can be calculated with a mathematical treatment of the transmittance data by following equations:

$$I = I_0 \times e^{-\alpha t} \quad (2.2)$$

$$(\alpha h\nu)^n = A(h\nu - E_g) \quad (2.3)$$

I/I_0 is defined as transmittance. in equation (2.2), I is the intensity of the transmitted light, I_0 is the intensity of the incident light, t is the thickness of as-deposited film and α is the absorption coefficient. In equation (2.3), $h\nu$ represents the photon energy, E_g is the band-gap and A is a constant. n depends on the nature of the band-gap . n is $1/3$ for indirect forbidden transition, $1/2$ for indirect allowed transition, $2/3$ for direct forbidden transition, and 2 for direct allowed transition. The intercept of a $(\alpha h\nu)^n$ - $h\nu$ plot with the $h\nu$ axis gives the band-gap of the semiconductor.

2.2.3 X-ray diffraction (XRD)

X-ray diffraction is used to characterize structural properties of as-deposited Nickel sulfide films. All measurements are carried out with a Siemens D-500 powder diffractometer. X-ray diffraction (XRD) is one the most widely and frequently used techniques for crystalline material characterization. The reflection of X-rays from crystalline materials from crystal planes interfere with each other leads to diffraction patterns which provide information about the structure and chemical composition of crystalline materials. Since the XRD pattern is unique for each crystalline material it can be used to identify the crystalline phases in a mixture. XRD patterns of the phases are identified from some standard patterns such as JCPDS (powder diffraction file of organic or inorganic phases) which is available in the software XRD. Thin film X-ray diffraction uses a low angle incidence of X-ray to characterize material up to a specific depth.

2.2.4 Scanning electron microscope (SEM)

Scanning Electron Microscopy (SEM) is a tool for surface morphology characterization. A Hitachi S-3000N scanning electron microscope is used to characterize surface morphology of samples. Generally, a scanning electron microscope consists of an electron gun, an aligning system, and a detection system. SEM technique have great resolution and depth of field for a three dimensional quality of the surface. There are different types of signals that are produced in SEM, and each of them is detected by a specific detector. In this study mainly secondary electron and energy dispersive X-ray was used. Low energy secondary electrons are emitted from the place exposed to the focused electron beam. Intensity of the secondary electrons is measured and difference in intensity creates contrast which enables us to visualize morphology of the sample. Incident electron interaction with the sample also creates X-rays from the sample, and the measurement of the energy and intensity of these X-rays can provide for elemental composition mapping across the specimen which is called energy dispersive X-ray spectroscopy (EDS). SEM is one the most widely used instrument for a rapid characterization of surfaces and interface of solid materials down to the sub-micrometer scale. Also, composition of the surface and micro-structural features formed on materials can be chemically analyzed by coupling SEM with EDS.

2.2.5 Dynamic Light Scattering and Zeta Potential

Dynamic light scattering is a common technique for determining the size distribution profile of small particles in suspension. Monochromatic light is sent into a solution including arbitrarily sized particles and interaction between light and particles results in elastic scattering, which is explained by Mie theory. Scattered light intensity fluctuation with time is processed by autocorrelation function by the software and dynamic information about size is obtained.

A colloidal system is when one of the three states of matter: gas, liquid and solid, are finely dispersed in one of the others. We are interested in solid dispersed in a liquid. The magnitude of the zeta potential gives an indication of the potential stability of the colloidal

system. Zeta potential is not measurable directly but it can be calculated using theoretical models and an experimentally-determined electrophoretic mobility. Zeta potential is calculated from theoretical considerations of directly measured electrophoretic mobility. Classical electrophoresis system is a cell with electrodes at either end to which a potential is applied. Particles move towards the electrode of opposite charge, their velocity is measured by laser velocimetry and expressed in unit field strength as their mobility.

CHAPTER 3
ELECTRODEPOSITION AND CHARACTERIZATION OF NICKEL SULFIDE

3.1 Introduction

Alternative photovoltaic materials that feature natural abundance, low extraction and processing costs, and reasonable efficiency have to be found. In this respect, transition metal chalcogenides such as oxide and sulfide compounds of Ni; attract attention because in addition to the features like abundance and cost, its electronic and optical properties vary dramatically by modifications in its stoichiometry. A number of nickel sulfide thin films with changing stoichiometry have been reported, such as NiS (Millerite, nickel(II) sulfide); NiS₂ (Vaesite, nickel sulfide); Ni₃S₂ (Heazelwoodite, nickel sulfide); and Ni₃S₄ (Polymidite, nickel(II,III) sulfide) [75]. The reported bandgap for NiS is 0.8 eV [93] and 0.35 eV [94] by different groups. Similarly, the bandgap for NiS₂ is differs from one report to another, 0.33 eV [95] and 1.3 eV [96]. NiS_x is a degenerate semiconductor with almost metal-like conductivity [90]. The bandgap for Ni₄S₃ is 0.35 eV [97] according to Anuar et. al. Therefore, the properties of these films are scattered around a range from metallic to semiconductor depending on S/Ni ratio in the deposited compound. Nickel Sulfides has been fabricated by numerous techniques. In addition to its low cost, and mature technology, electrochemical deposition method has many advantages over other methods since it allows direct deposition on conducting substrate and achieves good electrical contact and precise control of film thickness. ECD technique was studied by Anuar et al. [97] in order to deposit Nickel sulfide thin films using bath consisting of Ni-tartrate and sodium thiosulfate. Also H. Sun et al. used periodic potential reversal technique to deposit NiS thin films [133].

In this chapter, as a first stage we report the effect of solution stability and optimum deposition parameters to get uniform, crack free and adhesive Nickel sulfide to FTO (fluorine-

doped tin oxide) substrate. These optimum deposition parameters include 8.8×10^{-4} wt% gelatin as an additive to stabilize colloidal S [133], 0.013/0.5 as the ratio of Ni precursor (NiSO_4) to S precursor ($\text{Na}_2\text{S}_2\text{O}_3$), pH 4.7, 60°C temperature of the solution, and -0.4V deposition potential. After Ni_3S_2 film deposition with desired properties, the thermal oxidation of films at different temperatures is studied. Oxidation 550°C is found to be a temperature where metallic Nickel sulfide film turned to a semiconducting Nickel Oxy-Sulfide compound with band gaps changing with as deposited film structure.

3.2 Experimental

3.2.1 Sample Preparation

3.2.1.1 Preparation of Working Electrode

FTO coated glass is used as working electrode. The FTO film had a typical sheet resistance of $10\Omega/\square$ with a typical dimension of $1 \times 1.5 \text{ cm}^2$. Prior to deposition, in order to remove organic contaminants FTO coated glass electrodes are cleaned by degreasing process which is ultrasonication of sample in alcohol for 15 minutes. After degreasing process, the substrates are rinsed in de-ionized water.

3.2.1.2 Preparation of Solution

Ni_3S_2 thin films are electrodeposited from electrolytic solutions which were prepared by first dissolving bioreagent-grade gelatin (Aldrich) at 60°C in deionized water, and then adding various concentrations of reagent-grade NiSO_4 and $\text{Na}_2\text{S}_2\text{O}_3$. Solution pH was adjusted by adding diluted H_2SO_4 . Also series of deposition solutions prepared using Na Lactate or Tartaric acid as buffering and complexing agents, in order to see their effect on composition and structure of the film.

3.2.1.3 Cyclic Voltammetry of Solution

Cyclic voltammetry is often the first experiment performed in an electrochemical study for the study of electroactive species. CV is a simple and direct method to measure the current flowing through a working electrode as a function of applied potential. CV was performed first in

solutions with a single precursor, 0.5 M Na₂S₂O₃ or 0.013 M NiSO₄. The pH of the solutions was 4.7 and FTO was the working electrode. Electrochemical behavior of Na₂S₂O₃ solution is examined because the solution works as the source of sulfur of the aimed sulfide film. Reduction of S [134] was observed around -0.3 V vs. the Ag/AgCl reference electrode according to the reaction 1:



S²⁻ will react with H⁺ and form H₂S. For the NiSO₄ solution, reduction of Ni²⁺ was observed at -0.7 V:

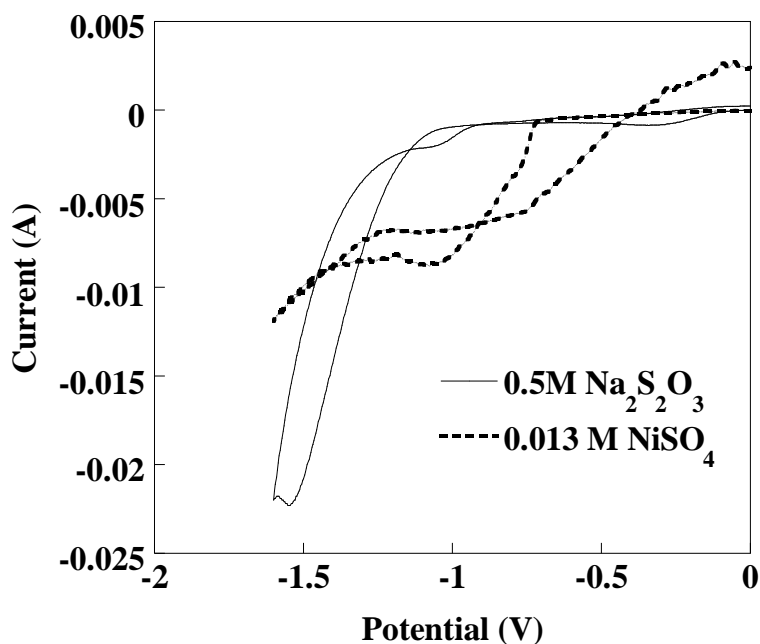


Figure 3.1 Cyclic voltammety of solutions containing (a) 0.5 M Na₂S₂O₃ and (b) 0.013 M NiSO₄ at pH 4.7. The solution temperature is 60°C. Reduction of S to S²⁻ is observed around -0.3 V and Ni²⁺ to Ni reduction around -0.7 V

CV tests were carried out in between 0 and -1.6 V in order to identify solution characteristics and determine the window of deposition potential. Voltammety in a solution containing 0.013 M

NiSO₄, 0.5 M Na₂S₂O₃, and 8.8×10⁻⁴ wt% gelatin is shown in Figure 3.2. The solution temperature was 60°C. A cathodic current increase is observed at -0.5 V. This is due to the reduction of S to S²⁻ (reaction (1)). As the potential goes beyond -1 V, a sharp increase in current confirms the deposition metallic Ni and further negative, H₂ evolves. When the deposition potential is between -0.5 and -1 V, the produced S²⁻ ions react with Ni²⁺ ions leading to a Ni₃S₂ film:

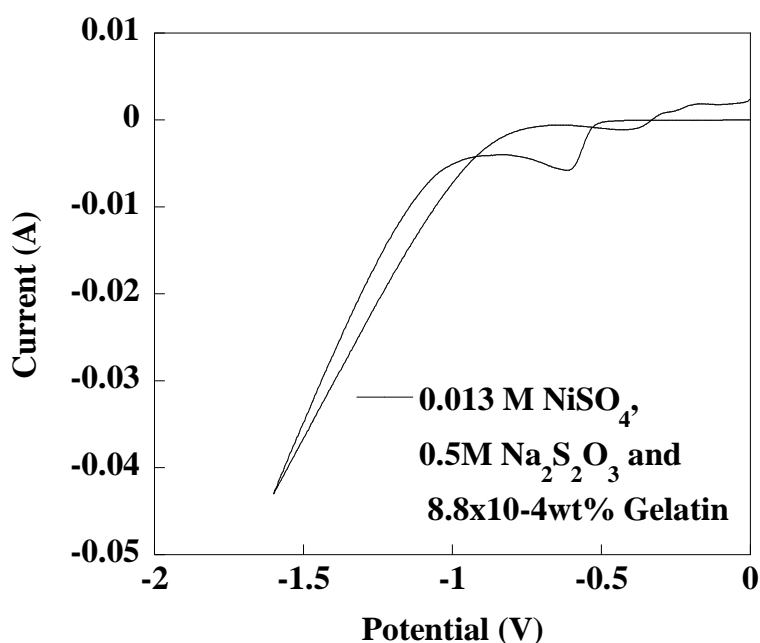


Figure 3.2 Cyclic voltammety of a solution containing 0.013 M NiSO₄, 0.5 M Na₂S₂O₃, and 8.8×10⁻⁴ wt% gelatin. The solution temperature is 60°C and solution pH 4.7. The reduction potential for S to S²⁻ is between -0.5 and -1 V

3.2.2 Deposition Process

Electrochemical experiments were carried out using a Princeton Applied Research VERSTAT II potentiostat and performed in a three-electrode cell with a platinum counter electrode, a silver/silver chloride/saturated sodium chloride reference electrode, and an FTO-coated glass substrate as the working electrode, as shown in Figure 3.3. The solution temperature was controlled between 30°C and 70°C by a Precision 280 water bath during

deposition. Deposition time was 10 minutes and a constant deposition potential was applied. After deposition, films were rinsed with deionized water.

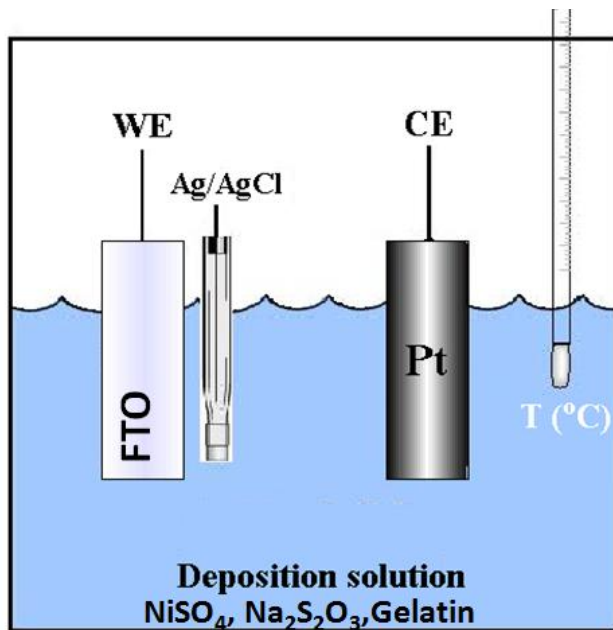


Figure 3.3 Arrangement of the deposition cell

3.2.3 Oxidation

Samples prepared by electrochemical oxidation were oxidized at furnace. Both ends of Silica tube were open to atmosphere. Oxidation temperature changed in between 300-700°C.

3.2.4 Characterization

The size and zeta potential of S particles in the solution was studied with a Brookhaven ZetaPALS zeta potential analyzer. Structural properties of the films were examined using a Siemens D500 X-ray diffractometer (XRD) with a Cu target. The morphology and composition of the films were examined by a Hitachi S-3000N scanning electron microscope (SEM) equipped with an energy dispersive spectrometer (EDS).

3.3 Effect of deposition conditions on Nickel Sulfide film structure

The key of an electrochemical reaction is a proper choice of a number of reaction parameters and it should be noted that an electrode reaction will not be only controlled by a

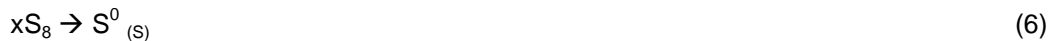
single parameter but by many other factors, which lead a large number of trials to optimize the process, keeping in view the product quality.

3.3.1 Effect of gelatin

Sodium thiosulfate releases thiosulfate and sodium ion in the water [137]:



Thiosulfate is unstable in acidic conditions and follows a dissociation reaction which releases sulfur [137, 138]:



Thiosulfate ion follows three steps during the formation of sulfur particles [139]. First step is called homogeneous reaction in which the formation of molecularly dispersed sulfur occurs. The rate of formation of sulfur is proportional to $(T)^{\frac{3}{2}}(H)^{\frac{1}{2}}$, where (T) and (H) are the total molar concentrations of thiosulfate and hydrogen ion, respectively. These sulfur particles are hydrophobic in nature and they have low zeta potential as well as low surface energy. So they are unstable in high surface tension such as water, especially when the particle size is very small [140]. Second step, which is called condensation, begins in less than 2 min with the formation of nuclei capable of further growth. Growth is favored in order to minimize the contact area between particle and water which result in a continuous increase in particle size. Finally, in the heterogeneous stage in addition to the new molecularly dispersed sulfur formation, old particles continue to grow and coagulate. When they grow larger than critical size they finally settle and cannot take part in the electrode reaction. Settling of sulfur particles creates an unstable solution which in turn causes degrade in the film properties and fluctuations in the results, which is a major concern for final properties of a photovoltaic cell. This can be observed with bare eyes since solution becomes turbid and white particles are either floating on top or

sank to the bottom of the beaker. Takahashi et al. [133] reported gelatin as an effective suppressant for colloidal S particles in CdS deposition, which is adopted for our NiSx deposition. The method proposed by Takashashi et.al., which is basically the addition of gelatin into the solution as a protective colloid. Gelatin, which is having one end that is hydrophilic (polar, or charged) and one that is hydrophobic (nonpolar), will be adsorbed on surface of sulfur particles. Agglomeration tendency of particles are reduced due to electrostatic repulsion between particles.

This can be supported by the difference in zeta potential of sulfur particles in solutions which includes 0 Wt% and 8.8×10^{-4} wt% gelatin amounts. Table 3.1 compares zeta potential of sulfur particles in solution containing with and without gelatin. Both solutions also contained 0.013M NiSO₄, 0.4M Na₂S₂O₃ with pH 4.7.

Table 3.1 Effect of Gelatin on Zeta-potential of Sulfur Particles

Gelatin amount (wt %)	Zeta Potential (mV)
0	-35.9
8.8×10^{-4}	-176.91

The magnitude of the zeta potential gives an indication of the potential stability of the colloidal system. Generally particles having zeta potential between around (+35mV) - (-35mV) are considered to be unstable and tend to flocculate. Beyond $\pm 35\text{mV}$; however, gives particles enough repulsion from other particles surrounding them and makes them stabilized. When 8.8×10^{-4} wt% gelatin added to the bath, zeta potential is increased by 5 times due to adsorption of gelatin on the sulfur particles. This allows us to control size of sulfur particles. Figure 3.4 shows the size of S particles as a function of solution pH. Without gelatin, the mean particle size

increases from ~750 nm to ~1,050 nm with a pH change from 4.7 to 3.3. With gelatin, however, the particle size is much smaller and increases from ~230 nm to ~280 nm in the same pH range. The solutions also contained 0.013M NiSO₄, 0.4M Na₂S₂O₃.

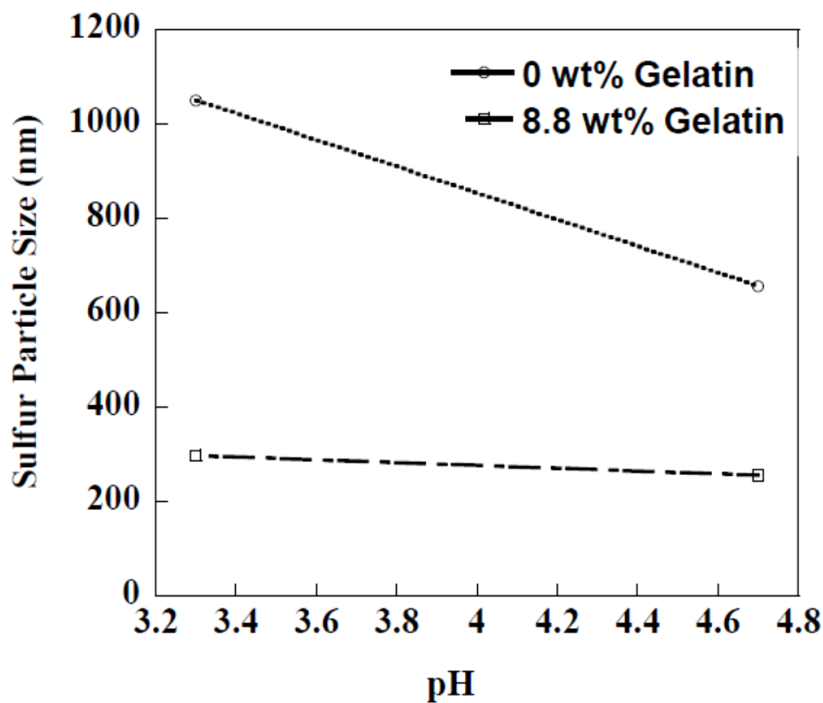


Figure 3.4 Size of S particles measured by zeta potential as a function of solution pH. Solution without gelatin shows increase in particle size with increasing pH. Particle size remains nearly constant with pH in a solution containing 8.8×10⁻⁴ wt% gelatin

Effect of gelatin amount on the film composition is shown in the Figure 3.5. Nickel ratio in the film is proportional to gelatin amount in the solution. Sulfur reduction shifts to more negative than -0.4V with increased amount of gelatin adsorption. Eventually, film becomes fully metallic Nickel when gelatin amount in the solution is 2%.

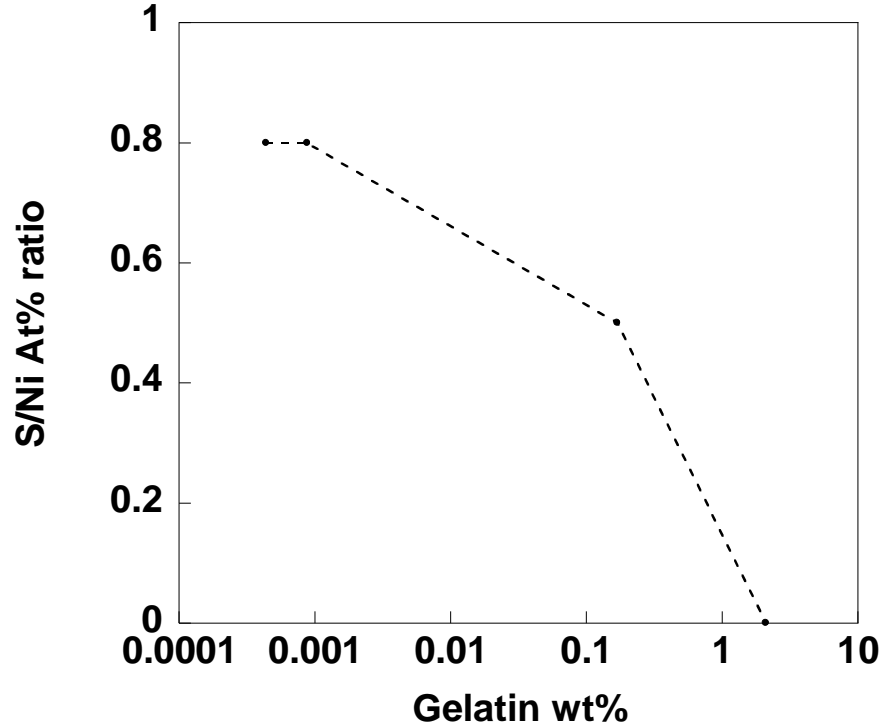


Figure 3.5 Effect of gelatin amount on the film composition. Sulfur percentage in the film composition decreases with increase in Gelatin amount in the solution

3.3.2 Effect of Deposition Potential

In general properties of semiconductor thin films are determined by microstructure and impurities. Electrode reduction rate governs microstructure of the film. Electron transfer rate at the electrode surface, chemical reaction rate between Ni^{2+} and S^{2-} following the electron transfer, mass transfer rate of Sulfur and Ni^{2+} , and other surface reaction rates such as adsorption, desorption, crystallization [127] are factors that affect electrode reduction rate. Potential applied to the cell controls the rate of electron transfer at the electrodes. In order to find out the optimum deposition potential, experiments were carried out potentials at -0.3V, -0.4V, -0.5V, -0.6V, -0.7V. Depositions last for 10 minutes in the solution containing 0.013 M NiSO_4 and 0.5M $\text{Na}_2\text{S}_2\text{O}_3$ and 8.8×10^{-4} wt% gelatin. Solution pH was 4.7 and temperature kept at 60°C. Figure 3.7 shows XRD plots of nickel sulfide thin films deposited at different potentials. Only Ni_3S_2 and FTO peaks were observed and there is no excess metallic film on

the substrates. Although cathodic current was not observed in the CV at potentials -0.3V and -0.4V (see Figure 3.2), homogeneous Ni₃S₂ thin film could be obtained at those potentials with a slow deposition rate. The reason for the observation of zero current at potentials -0.3V and -0.4V in CV is due to very slow increase in reduction rate of sulfur. Film coverage was poor when it is deposited at -0.3V. Best film uniformity and adhesion, and highest intensity Ni₃S₂ peaks are obtained at -0.4V. Due to increased rate of nucleation and growth films deposited at -0.5V, -0.6V and -0.7V didn't stick well to the substrate and peeled off during rinse. When the electrodeposition proceeds with a high growth rate films are more prone to have inclusions and defects which increase the resistivity of the film. As a result, by controlling rate of sulfur reduction we could optimize film uniformity and adhesion on to the substrate. Figure 3.6 shows SEM pictures of the films deposited at different potentials. The films appear granular, which is common for many metal sulfides. The film deposited at -0.7 V appears the densest according to SEM. XRD, however, reveals its almost amorphous structure since there is no clear NiS_x peak in the XRD pattern. Trade-off between deposition rate and film morphology is optimized at -0.4V since the film displays the highest XRD intensity, as well as good uniformity and adhesion to FTO substrate.

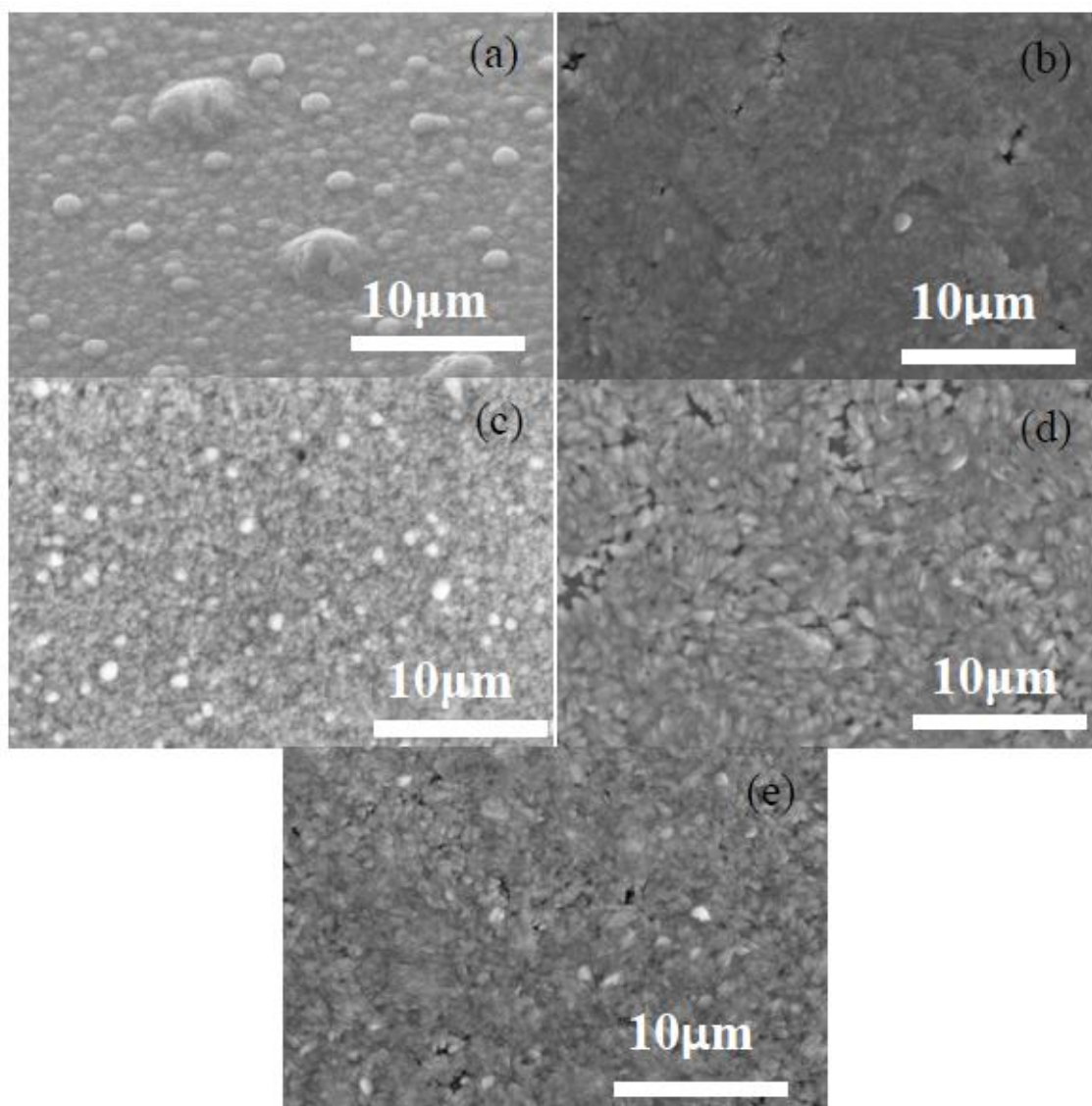


Figure 3.6 Scanning electron microscopy images of Ni_3S_2 films as a function of deposition potential from solutions containing 0.013 M NiSO_4 and 0.5 M $\text{Na}_2\text{S}_2\text{O}_3$. The solution temperature is 60°C and solution pH 4.7. Deposition potentials are (a) -0.7 V, (b) -0.6 V, (c) -0.5 V, (d) -0.4 V, and (e) -0.3 V

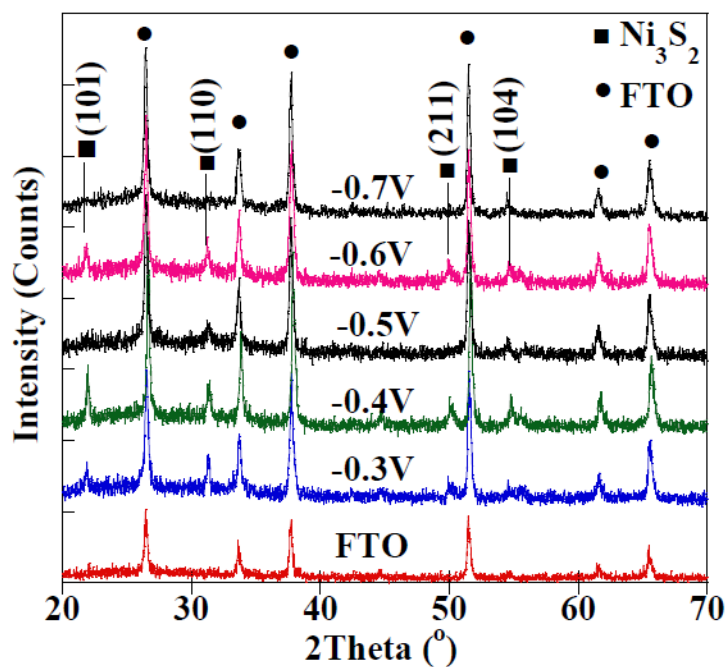


Figure 3.7 X-ray diffraction of NiS_x films as a function of deposition potential from solutions containing 0.013 M NiSO₄ and 0.5 M Na₂S₂O₃. The solution temperature is 60°C and solution pH 4.7. All of the films has peaks belonging to the FTO and Ni₃S₂ phase

3.3.3 Effect of solution temperature

Solution temperature is changed from 40 to 70°C. Temperature increase fostered diffusion of Ni²⁺ ions on to the FTO substrate which increased the deposition rate of the film. Also the higher temperature is, the easier it is to form nuclei and grow grains, which results in higher growth rate. Figure 3.8 shows XRD patterns of the films. The films at 40°C and 60°C shows Ni₃S₂ peaks in addition to FTO peaks. The highest XRD intensity comes from the film deposited at 60°C. There is no NiS_x peaks observed at 50°C, since most of the film peeled off during rinse. The film became almost amorphous at 70°C. SEM images of films deposited at 50, 60, 70°C are shown in the Figure 3.9. Both of films deposited at 50°C and 60°C reveals uniform structure but film at Figure 3.9.b is more crystalline. As the solution temperature was increased to 70°C excess sulfur, i.e. bright white particles on the Figure 3.9.c., is observed on top of films.

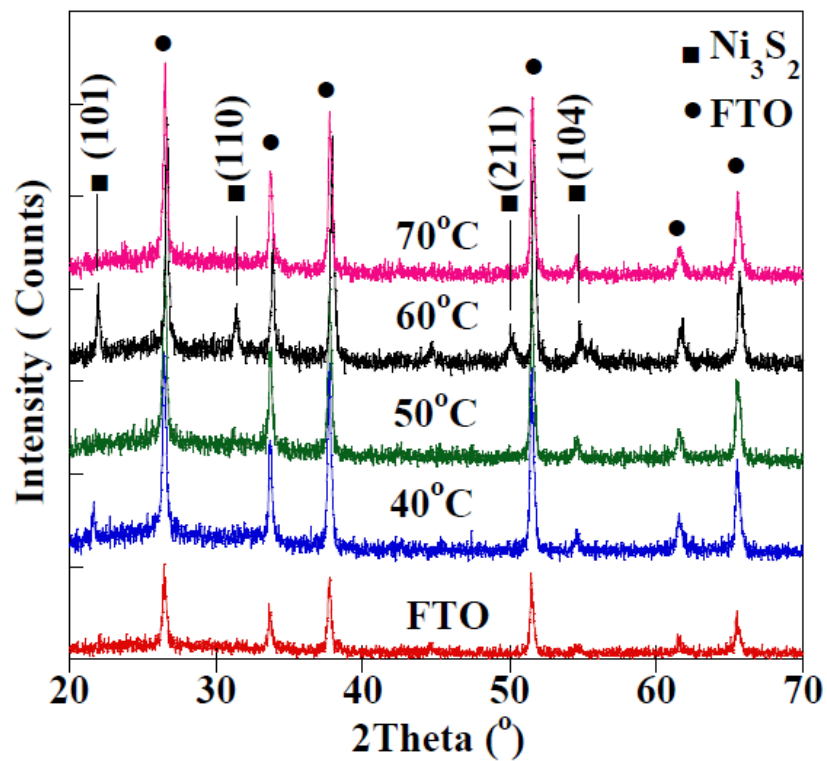


Figure 3.8 X-ray diffraction of NiS_x films as a function of deposition temperature from solutions containing 0.013 M NiSO₄ and 0.5 M Na₂S₂O₃. The solution pH is 4.7 and deposition potential – 0.4V. The films deposited at 40°C and 60°C are Ni₃S₂

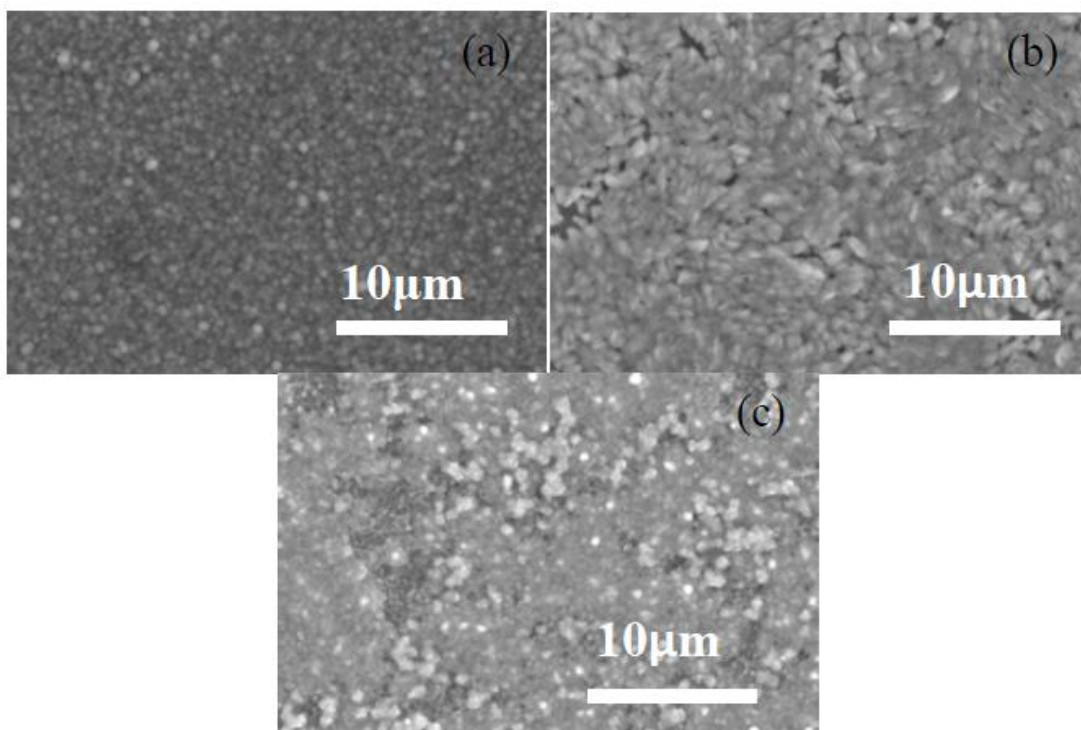


Figure 3.9 Scanning electron microscopy images of NiS_x films as a function of deposition temperature from solutions containing 0.013 M NiSO₄ and 0.5 M Na₂S₂O₃. The solution pH is 4.7 and deposition potential -0.4V. Deposition temperature is (a) 50°C, (b) 60°C, and (c) 70°C

3.3.4 Effect of Solution pH

In addition to deposition potential and solution temperature, pH of the medium plays an important role in the microstructure of film since the equilibrium reaction (5) will be shifted towards sulfur when the acidity of medium is increased. Although there is a higher probability of inter-particle collision between sulfur particles when pH increased, the size of the S particles remains nearly constant with solution pH (Figure 3.4), resulting in a stable solution over a wide range of pH when gelatin added to the solution. However, the microstructure of the films, as well as their uniformity and adhesion to FTO substrate, changes with solution pH. Figure 3.10 shows the effect of solution pH on film quality by comparing the XRD patterns. The films were deposited for 10 minutes at 60°C in solutions containing 0.013 M NiSO₄, 0.5 M Na₂S₂O₃, and 8.8×10^{-4} wt% gelatin. The XRD intensity decreases with increased acidity due to peeling off of the film, as well as inhomogeneous coverage of the film on the substrate. This may be due to

higher number of sulfur particles increased nucleation and growth rate of the film beyond the desired value. The results suggest that the optimum deposition pH is close to 4.7.

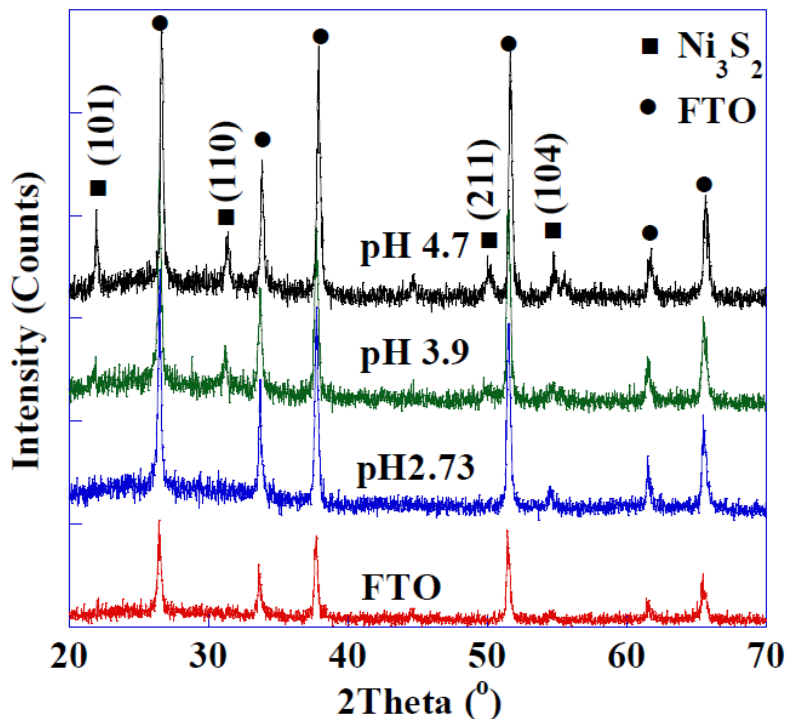


Figure 3.10 X-ray diffraction of NiS_x films as a function of pH from solutions containing 0.013 M $NiSO_4$, 0.5 M $Na_2S_2O_3$, and 8.8×10^{-4} wt% gelatin. The solution temperature is $60^\circ C$ and deposition potential -0.4 V. The film deposited at pH 4.7 shows the most intense Ni_3S_2 peaks. The film deposited at pH 2.73 is largely amorphous

3.3.5 Effect of Ni/S precursor ratio

Generally, crystal growth consists of two steps: nucleation and growth of grain, which mainly depend on concentration of electroactive species. The effect of Ni/S ratio in the solution is studied by keeping the $Na_2S_2O_3$ concentration constant at 0.5 M and varying the $NiSO_4$ concentration from 0.04 M to 0.013 M. All the solutions contained 8.8×10^{-4} wt% gelatin. Films were deposited for 10 minutes at $60^\circ C$ and pH 4.7. At a given temperature, film thickness is mainly determined by the concentration of electroactive species: Ni^{2+} and S. As [S] concentration is kept constant for all depositions, $[Ni^{2+}]$, becomes the dominant factor. As the Ni^{2+} increases, it's easier to form nuclei of NiS_x at the electrode surface, which leads to higher

growth rate. The films deposited at higher NiSO_4 concentrations (0.04 M and 0.02 M NiSO_4) had poor adhesion and poor uniformity. The excessive growth rate is believed to cause poor adhesion to FTO substrate. SEM images of these films are shown in Figure 3.11. The films from 0.02 M and 0.013 M NiSO_4 are similar and they are more compact and crystalline than the film from 0.04 M NiSO_4 .

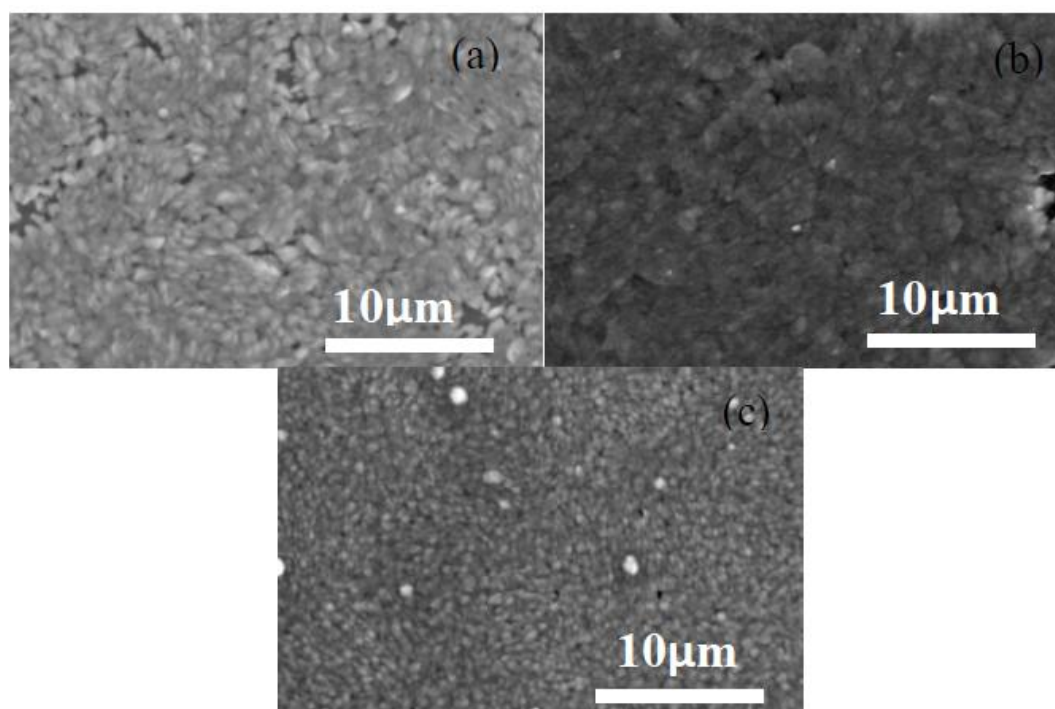


Figure 3.11 Scanning electron microscopy images of NiS_x films as a function of Ni/S ratio in the solution. The solution pH is 4.7, solution temperature 60°C , and deposition potential -0.4V . The Ni/S ratio is (a) 0.013, (b) 0.02, and (c) 0.04

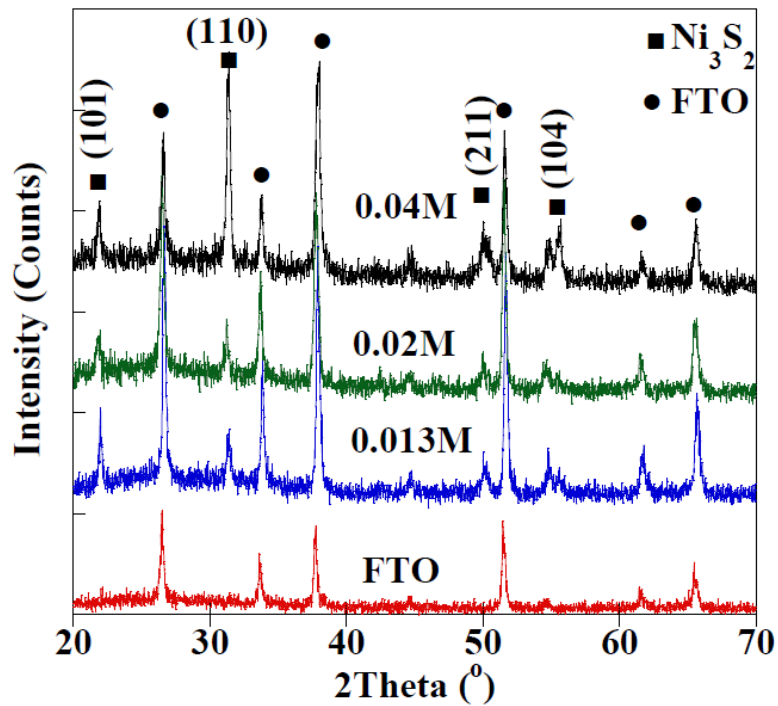


Figure 3.12 X-ray diffraction of NiS_x films as a function of Ni/S ratio in the solution. The solution pH is 4.7, solution temperature 60°C, and deposition potential -0.4V. All of the films are Ni₃S₂

XRD patterns of the films reveal changing intensities of crystal planes with changing Ni²⁺ concentration. Figure 3.13 shows increase in NiSO₄ concentration favors (110) plane growth in the film and this resulted in poor adhesion to the FTO substrate.

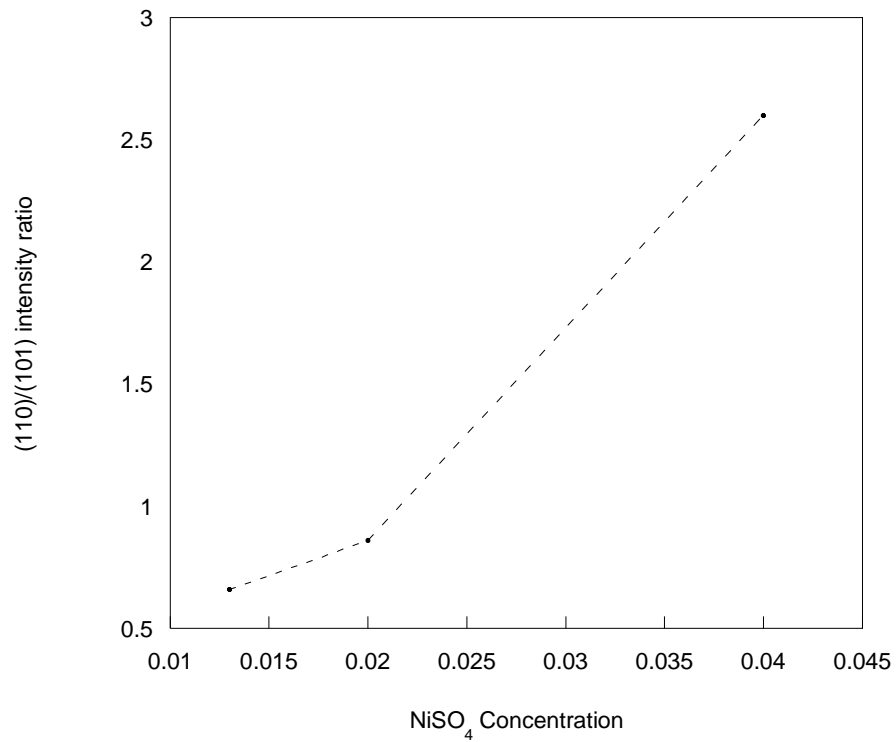


Figure 3.13 Intensity ratio of the (110) to (101) plane coming from Ni₃S₂ films deposited at different Ni precursor concentrations

In order to demonstrate the uniformity of the Ni₃S₂ films, EDS mapping of S and Ni was taken at low magnification, as shown in Figure 3.14. As a reference, EDS mapping of Sn is also presented, which comes from the FTO substrate.

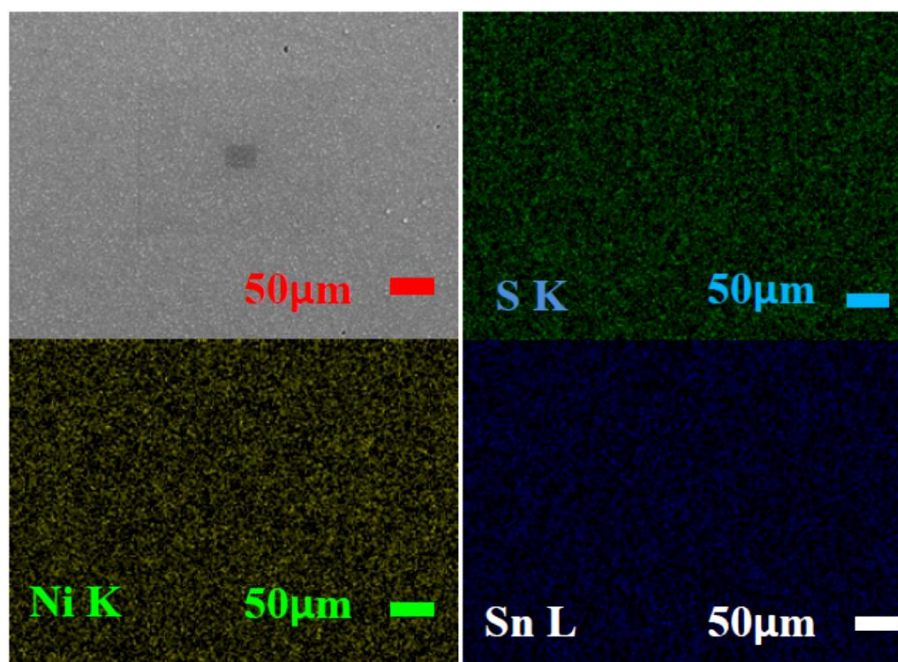


Figure 3.14 EDS mapping of (b) S and (c) Ni to demonstrate the compositional uniformity of the film. For comparison, (d).mapping of Sn, which comes from the FTO substrate, is shown

3.3.6 Effect of Complexing Agents

3.3.6.1 Na Lactate(NaC₃H₅O₃)

Complexing the metal ions with organic ligands changes the structure of the films by favoring growth in some directions and slowing down the others. Ligands, complexing agents should be an electron donating soluble ion to be able to bind to the metal ion and produce a complex ion. As a result metal ion reduction will be suppressed. a sodium salt of lactic acid, Na lactate, is chosen as complexing agent for this study since it is soluble in the aqueous medium and it is shown that had a profound effect on electrodeposition of CuO [135].

Na Lactate can also be used as buffer reagent in order to stabilize solution pH. As stated above, Sulfur colloid formed by Na₂S₂O₃ according to the reaction 7 is not stable in the aqueous solutions.



When the S_8 is depleted, due to settling out as solid sulfur particles, equilibrium shifts right to produce more S_8 which will eventually result in an increase in the pH. pH increase with time in a solution containing 0.1 M $NiSO_4$, 0.5 M $Na_2S_2O_3$ is demonstrated in the Figure 3.15.

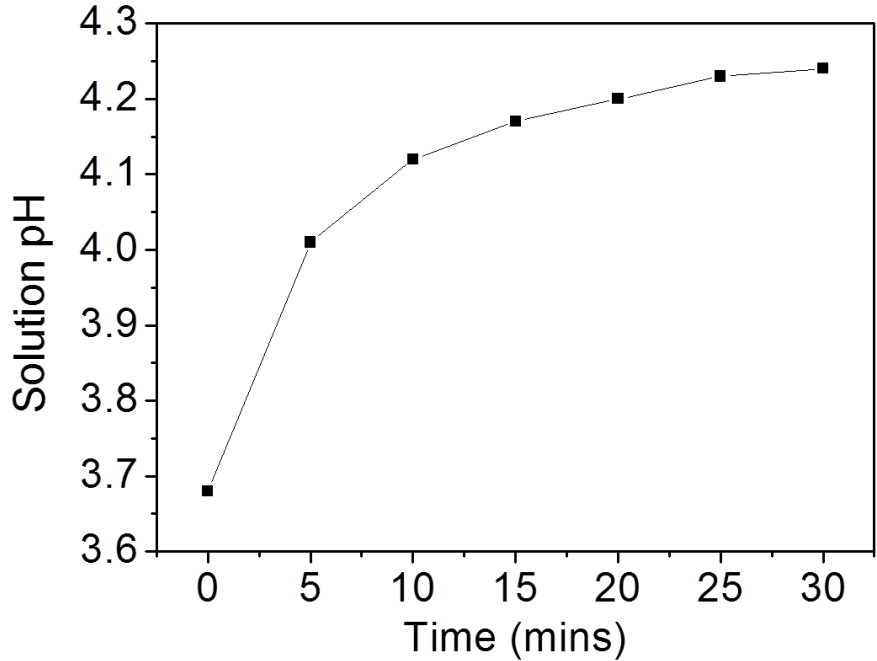


Figure 3.15 pH increase with time in a solution containing 0.1 M $NiSO_4$, 0.5 M $Na_2S_2O_3$

The deposition solution contained 0.02 M $NiSO_4$, 0.4 M $Na_2S_2O_3$ and 0.5 M Na Lactate Solution pH was adjusted to 3.9 by H_2SO_4 and solution temperature is set between 50 – 80°C. - 0.4V is applied for 30 minutes and thickness was about ~1.5 μm . The deposition rate is slow on the order of magnitude when compared to the ones at solutions including gelatin. This is due to chelating effect of lactate ion with Ni ion.

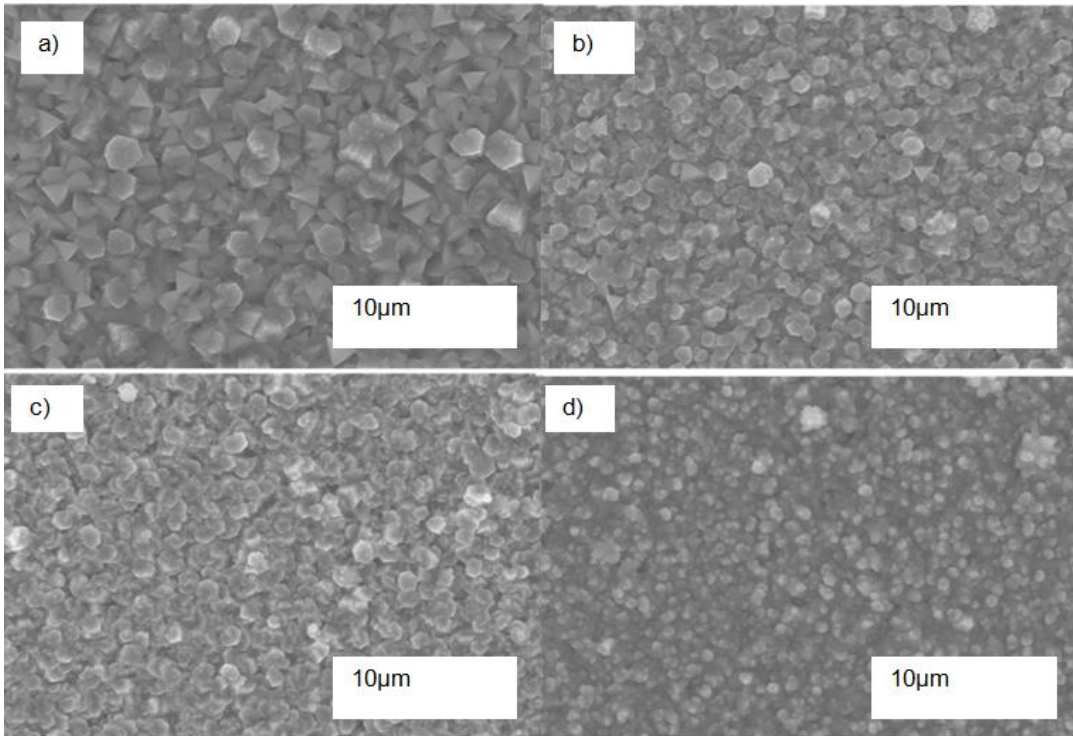


Figure 3.16 Scanning electron microscopy images of NiS_x films as a function of temperature of the solution. The solution pH is 3.9, deposition potential $-0.4V$ solution temperature is (a) 50, (b) 60, and (c) 70 (d) 80

XRD patterns revealed that all films are Ni₃S₂. XRD intensities coming from samples have a decreasing trend with increase in deposition temperature. This indicates that films become more amorphous when deposition temperature is increased.

Also it can be observed from Figure 3.16, decrease in pH below 3.9 degrades the crystallinity of structure. The deposition solution contained 0.02 M NiSO₄, 0.4 M Na₂S₂O₃ and 0.5 M Na Lactate Solution pH was adjusted between 3.9-2.6 by H₂SO₄ and solution temperature is set 50°C. $-0.4V$ is applied for 30 minutes. Stability of metal complex is pH dependent. Lower the pH of the solution, lesser would be the stability of complex since increased number of H⁺ ions are competing with the metal ions for ligand. As a result Ni-lactate compositions release

increasingly more metal ion when pH is more acidic. This will eventually result in reaction rate increase which degraded the film quality in this case.

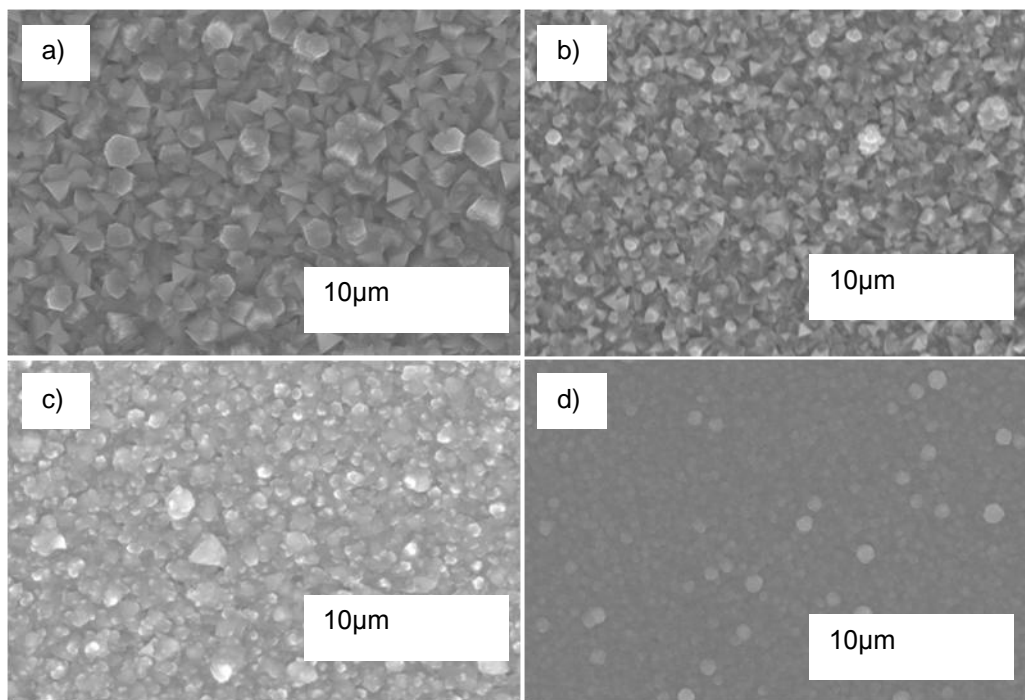


Figure 3.17 Effect of pH on the film structure. The deposition solution contained 0.02 M NiSO₄, 0.4 M Na₂S₂O₃ and 0.5 M Na Lactate. Solution temperature is set 50°C. -0.4V is applied for 30 minutes. Solution pH was adjusted between (a) 3.9, (b) 3.5, (c) 3.1 and (d) 2.6 by H₂SO₄

3.3.6.2 Tartaric Acid

Electrochemical deposition of NiS₂ by using Na Tartrate as a complexing agent is reported by Annuar et al. [96]. In order to confirm its effect Tartaric acid is used in my work to chelate with Ni²⁺ and obtain a Ni-tartrate complex. 0.02 M NiSO₄, 0.4 M Na₂S₂O₃ and 0.1 M Tartaric acid solution with pH 2.15 used for electrochemical deposition. Temperature of the solution was in between 50-80°C. Deposition time was 30 min. -0.2 V applied to the cell. Indium

doped Tin oxide coated glass substrate (ITO) is used as a working electrode instead of FTO due to some eliminate overlapping peaks in XRD of NiS₂ and FTO.

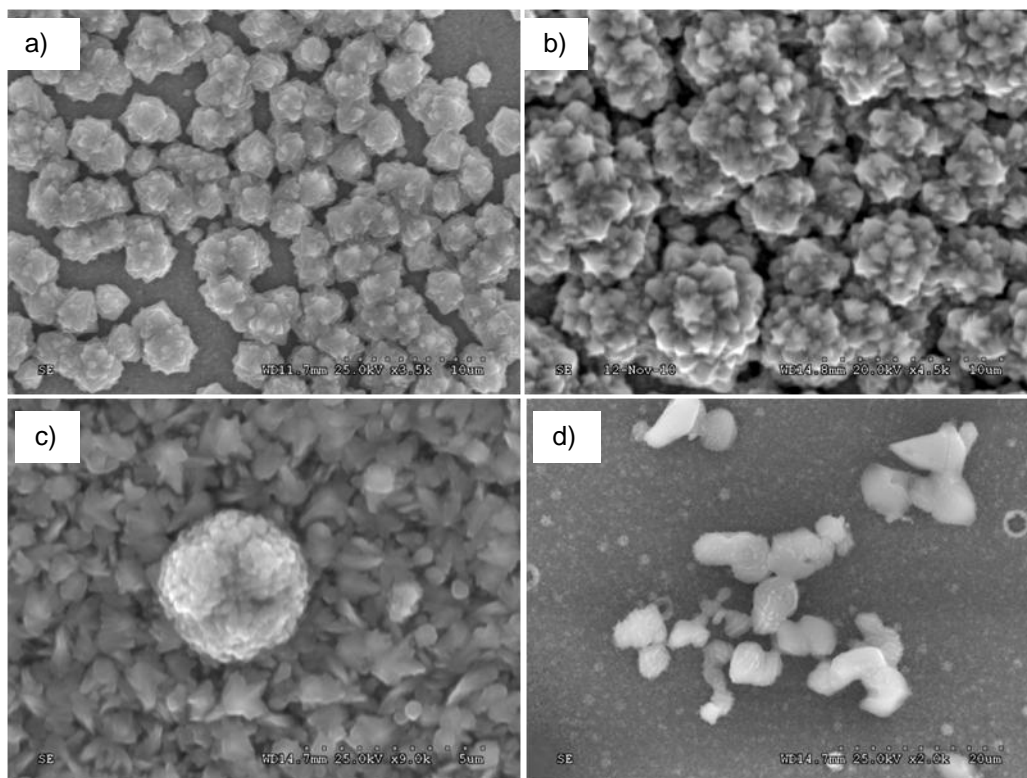


Figure 3.18 Effect of temperature on the film morphology. 0.02 M NiSO₄, 0.4 M Na₂S₂O₃ and 0.1 M Tartaric acid solution with pH 2.15 is prepared. Deposition time was 30 min. -0.2 V applied to the cell. Indium doped Tin oxide coated glass substrate (ITO) is used as a working electrode instead of FTO Temperature of the solution was (a)50, (b)60, (c)70, (d)80°C

The densest structure obtained from the deposition at 60°C according to SEM images on the Figure 3.18. While only existing crystalline phase is NiS₂ according to XRD pattern on Figure 3.19, S/Ni atomic percent ratio obtained from EDS is 1.2. This indicates amorphous metallic Nickel exists in the film.

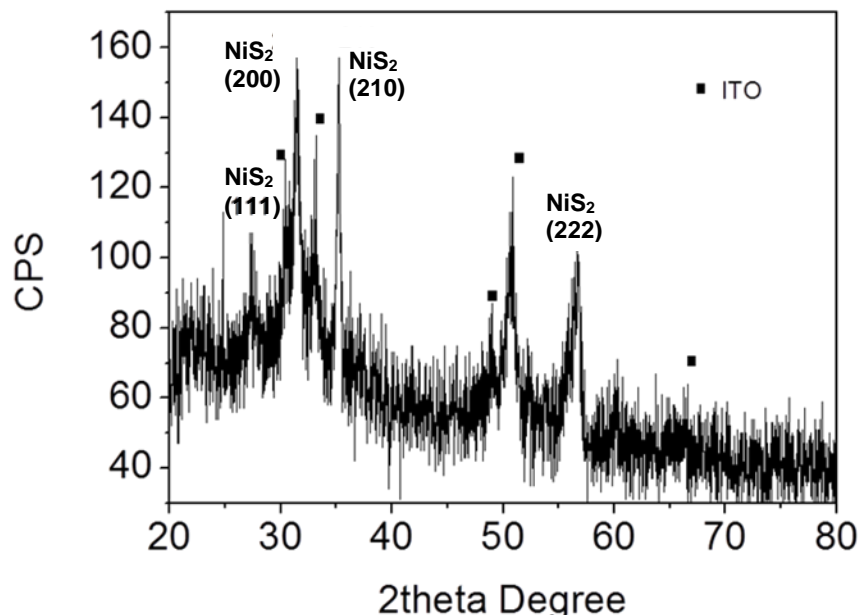


Figure 3.19 XRD of sample deposited at 0.02 M NiSO_4 , 0.4 M $\text{Na}_2\text{S}_2\text{O}_3$ and 0.1 M Tartaric acid solution with pH 2.15 at 60°C . Deposition time was 30 min. -0.2 V applied to the cell. Indium doped Tin oxide (ITO) coated glass substrate is used as WE

3.4 Oxidation of Nickel Sulfide films and its optical properties

Our design strategy for obtaining Nickel Oxysulfide structures is consisted of two steps which are deposition of metal sulfide and then oxidation. After optimizing the conditions for Nickel sulfide film two sets of samples were oxidized in air in order to substitute sulfur with oxygen and from a new structure which is the objective of the present work. Oxidation is progressively proceeding from the surface layers into the deeper layers. The thermally-induced oxidation changes the composition of the Nickel sulfide films.

XRD of the films are measured in order to determine the crystalline phases formed in the film. According to the pattern NiO phase is present in the film and there is two more peaks that are believed to belong to Ni Oxysulfide phase but couldn't be identified since none of them

were matching with the data base. EDS that shows 16% sulfur support Nickel Oxysulfide phase generation (

Figure 3.21). Ni/O/S ratio is around 3/2/1.

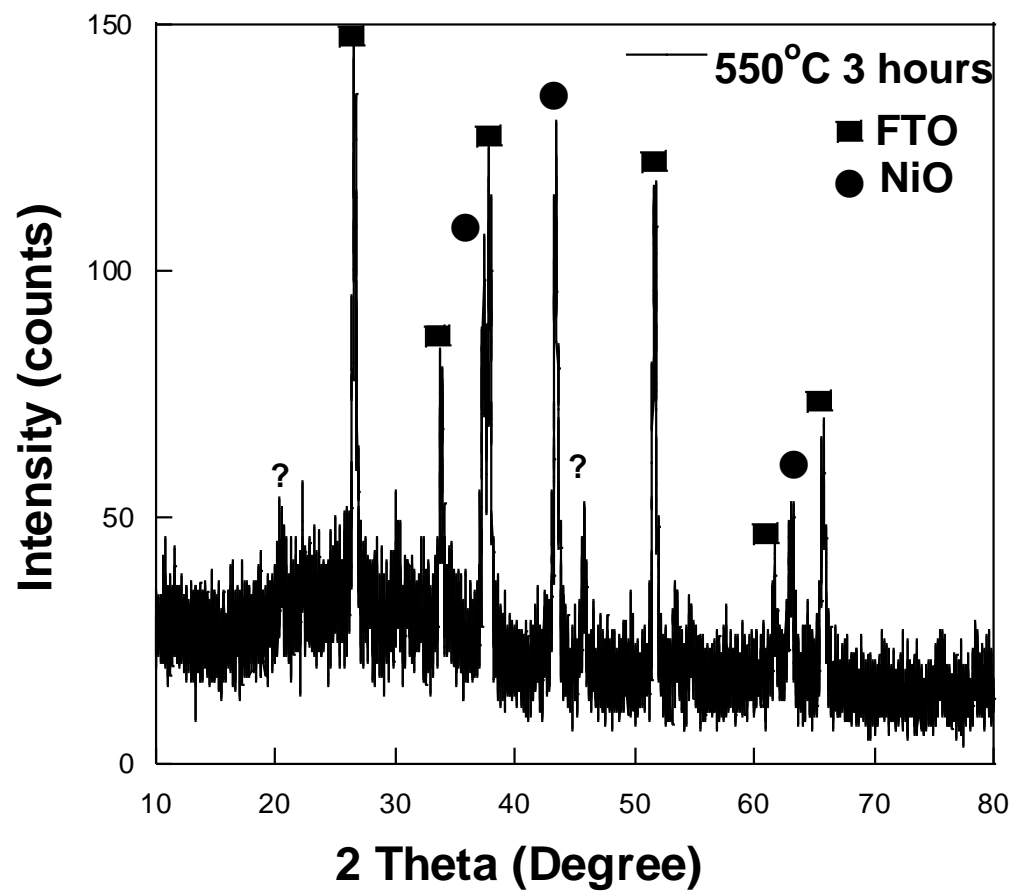
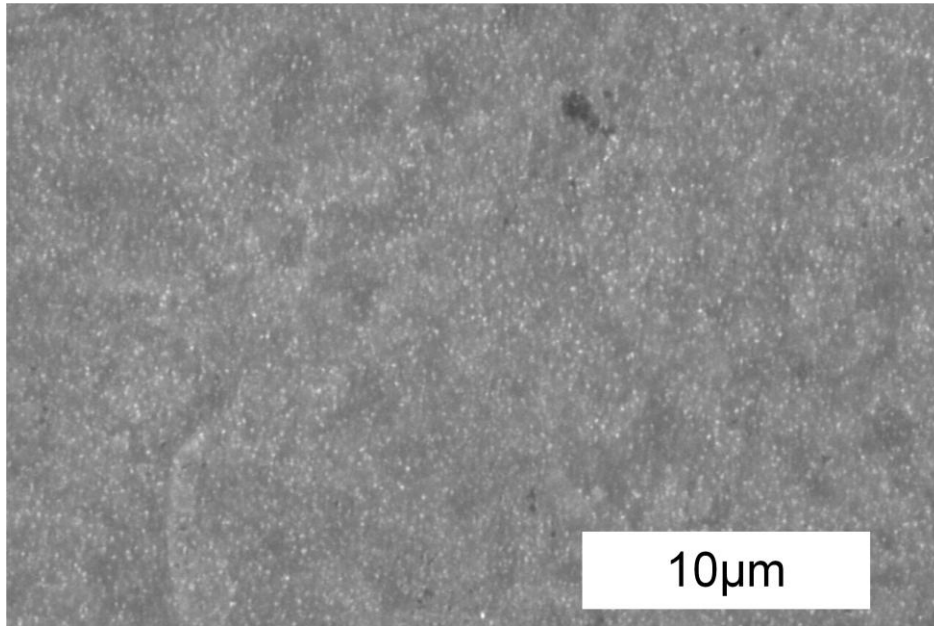


Figure 3.20 XRD pattern of the 1.4 μm film oxidized at 550°C for 3 hours



Ni %	O %	S %
49.4	31.9	16.4

Figure 3.21 Secondary electron image from SEM and Ni,O,S elemental compositional ratio from EDS

Transmittance spectra in Figure 3.22 is from the samples before oxidation and it demonstrates films are opaque since there is no transmitted light for sample with 0.6 and 2.4µm thickness. We can also see coverage becomes very poor due to increase in transmittance to 40% when sample thickness is below 0.6µm.

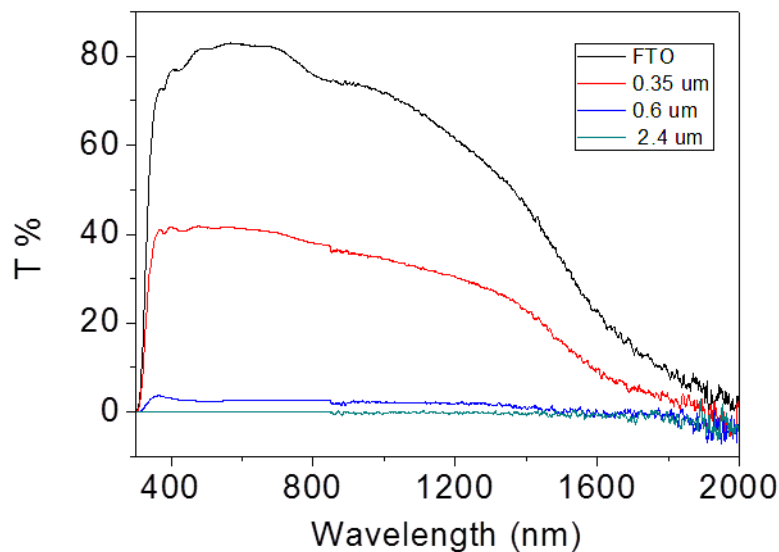


Figure 3.22 Transmittance spectra is from the samples before oxidation and deposited at presence of Lactate complexing ion. Thicknesses of the samples are 2.4 μm , 0.6 μm , 0.35 μm , It demonstrates films are opaque and coverage becomes very poor below 0.6 μm

The first set of samples was deposited at solution including Gelatin. The thicknesses of the films were 0.7 μm and 1.4 μm for different purposes. 0.7 μm samples are selected to study oxidation temperature effect on optical properties and oxidized at air for 3 hours at following temperatures 400°C, 450°C, 500°C, 550°C. Transmittance spectra of these films are shown in Figure 3.23. Temperature has a profound effect on optical properties of material since oxidation reaction rate is exponentially increasing with temperature according to Arrhenius equation.

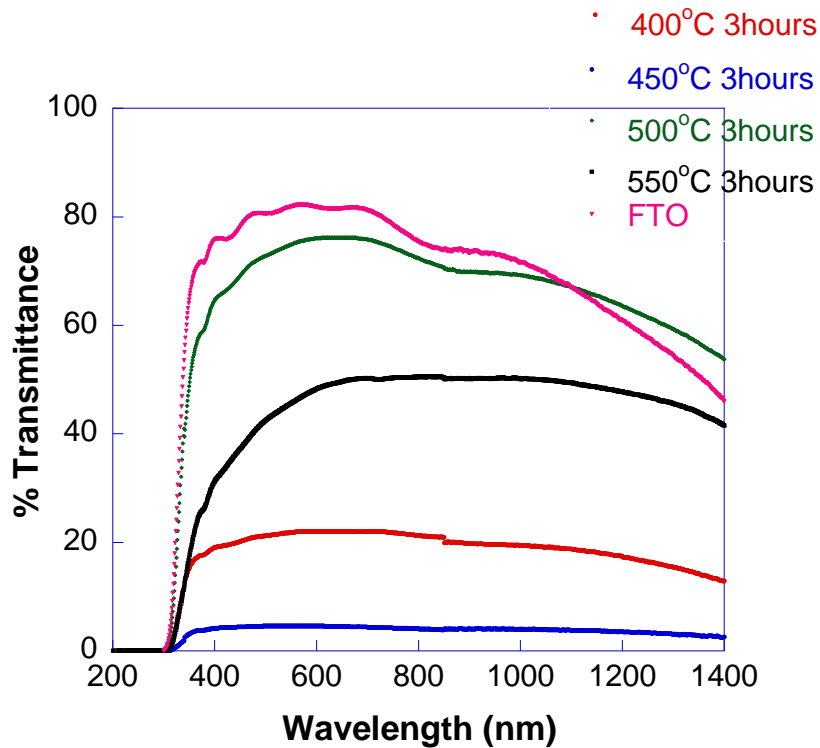


Figure 3.23 Transmittance spectra of the samples having $0.7\mu\text{m}$ thickness. Samples are deposited from 0.013M NiSO_4 , $0.5\text{M Na}_2\text{S}_2\text{O}_3$, $8.8 \times 10^{-4}\text{wt}\%$ Gelatin solution at pH 4.7 Then oxidized at air for 3 hours at 400°C , 450°C , 500°C , 550°C

Sample thickness is increased to $1.4\mu\text{m}$ to fully cover the FTO and oxidized at 550°C for 30 minutes, 1hour, 2hours and 3 hours. Transmittance spectra are shown in the Figure 3.24. Obviously there is a phase and composition change that is responsible from metallic to semiconductor transition. More significant changes are observed after 2 to 3 hours of heating time.

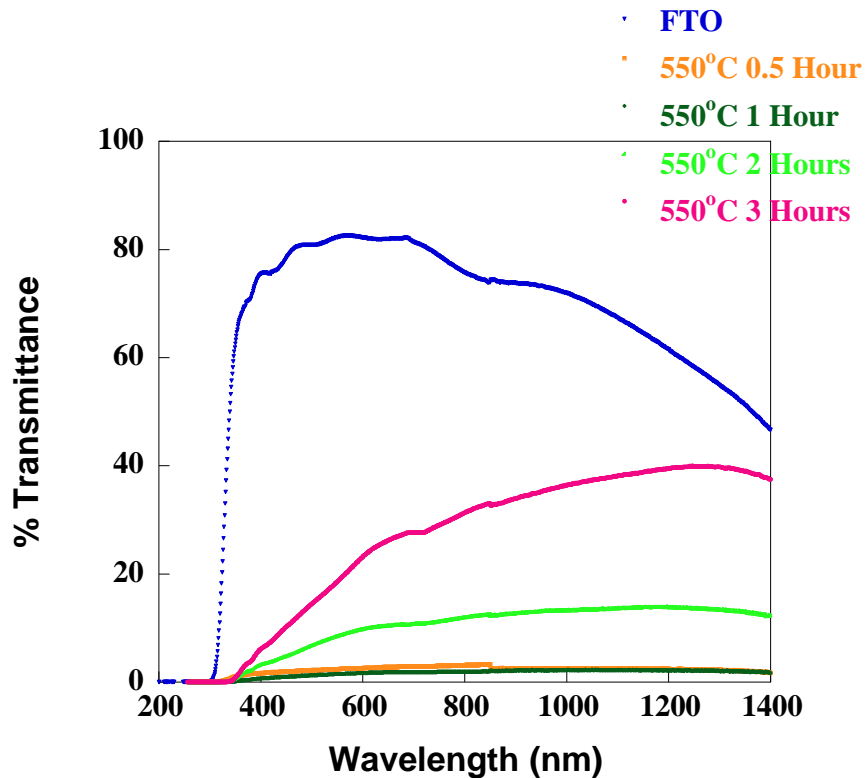


Figure 3.24 Transmittance spectra of 1.4µm films deposited at the same conditions Samples oxidized at air for 3 hours at 400°C, 450°C, 500°C, 550°C

Transmittance spectra of the 1.2 µm film after oxidation above 550°C is shown in Figure 3.25. Glass substrate is softened and changed its shape around 660- 700°C. The band gap energy and transition type was derived from mathematical treatment of the data obtained from the optical transmittance versus wavelength graph. The relationship for near-edge absorption is:

$$A = [k(h\nu - E_g)^{n/2}] / h\nu \quad (3.1)$$

Where ν is the frequency, h is the Planck's constant, and k is a constant. The bandgap, E_g , could be obtained from a straight line plot of $(A h \nu)^{2/n}$ as a function of $h\nu$. Extrapolation of the line to $h\nu$, where the value of $(A h \nu)^{2/n}$ is zero, will give E_g . If a straight-line graph is obtained for $n = 1$, it indicates a direct electron transition between the states of the semiconductor. The transition is indirect if a straight-line graph is obtained for $n = 4$. The straight-line behavior

obtained for indirect transition of the band structure as can be seen from the. The band gap energy and transition type of the film oxidized at 550°C and 650°C were derived and straight-line behavior obtained for indirect transition of the band structure extrapolated to energy axis and intersects the axis at 2.8 eV and 3 eV, respectively and it can be seen from the Figure 3.26 a and b. The direct band gap extraction (Figure 3.26.c) shows 3.5eV and it is believed to belong to FTO since its value matches with direct band gap measurement of bare FTO. The slope of the transmittance versus wavelength is small, i.e. the spectrum is flat, since defects in the film forms interband energy levels. Increase in indirect band gap proportional to oxidation temperature is understandable due to increase in replacement of sulfur with oxygen in the film structure and eventually becoming Nickel Oxide around 650°C.

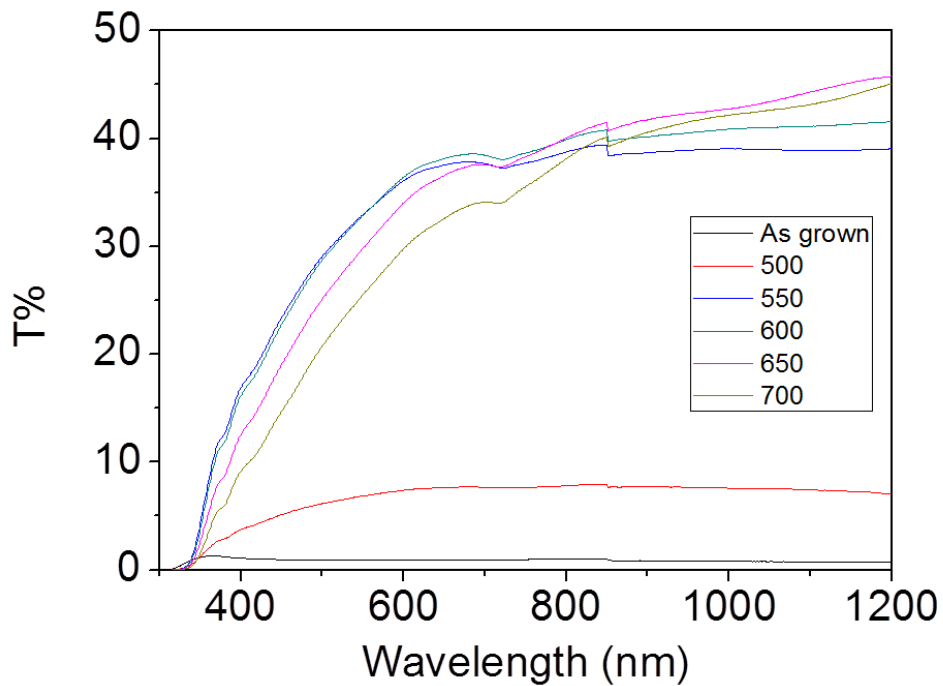


Figure 3.25 Transmittance spectra of the 1.2 μm film after oxidation at different temperatures

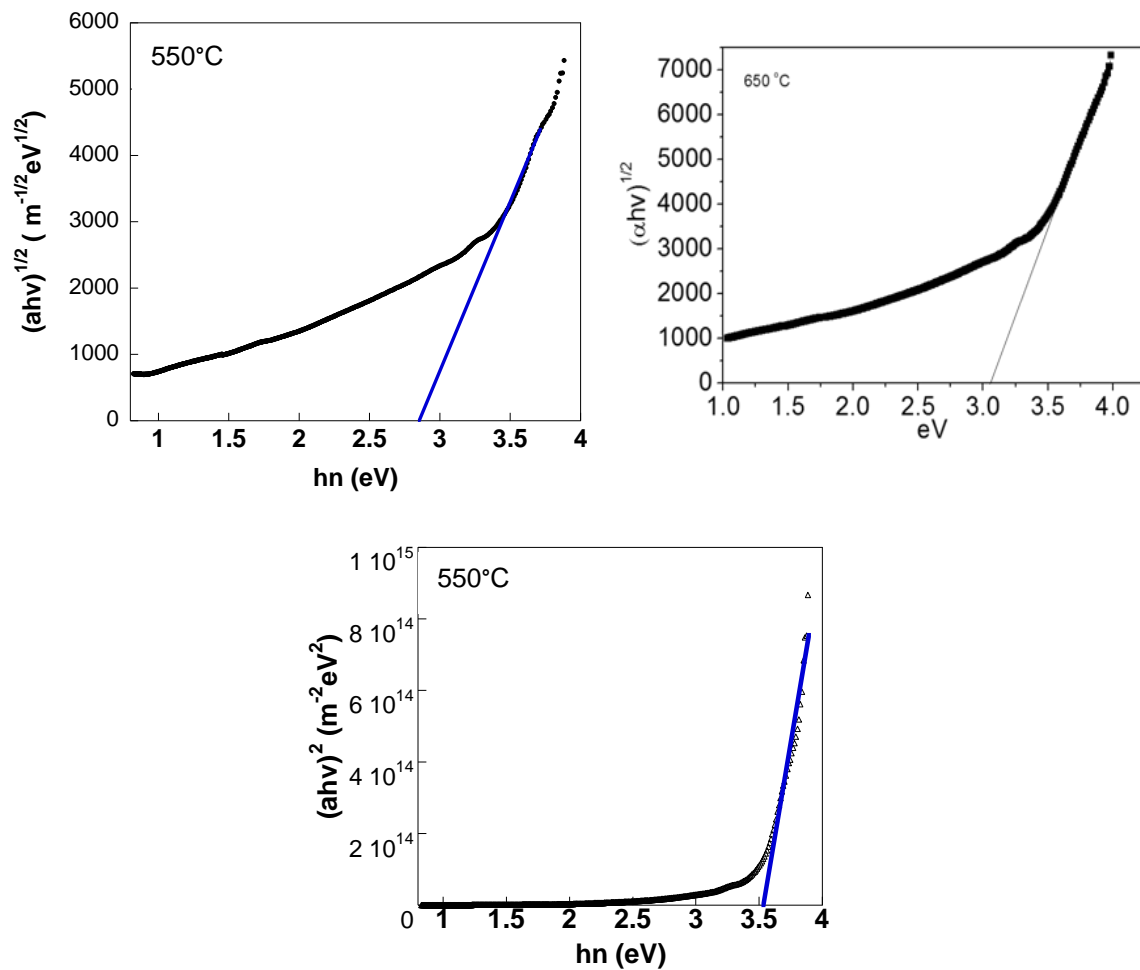


Figure 3.26 Plot of $(Ahv)^{1/2}$ vs $h\nu$ of the 1.4 μm film oxidized at (a) 550°C and (b) 600°C (c) the plot of $(Ahv)^2$ vs $h\nu$ of the 1.4 μm film oxidized at 550°C

3.5 Summary

A study on the NiS_x electrochemical deposition and oxidation of NiS_x films are presented. Ni₃S₂ films have been successfully deposited on FTO substrate with significantly improved film microstructure, uniformity and adhesion. This is accomplished by optimizing the deposition conditions and stabilizing the deposition solution. It is found that 8.8×10^{-4} wt% gelatin is effective in preventing precipitation of colloidal S particles in the acidic solution. The optimum deposition conditions are found to be 0.013 M NiSO₄, 60°C deposition temperature, –

0.4 V deposition potential vs. Ag/AgCl reference electrode, and solution pH 4.7. 500-550°C is found to be a transition temperature from metallic Nickel sulfide phase to a semiconducting cubic NiO and crystalline Nickel oxysulfide with unknown stoichiometry.

CHAPTER 4

CONCLUSION AND FUTUREWORK

4.1 Conclusion

Alternative photovoltaic materials that feature natural abundance, low extraction and processing costs, and reasonable efficiency have to be found. In this respect, transition metal chalcogenides such as oxide and sulfide compounds of attract attention. In addition to low cost and mature technology, electrodeposition has several advantages over other solution-based techniques discussed above. Electrodeposition requires a conducting substrate and the good electrical contact between film and substrate is important in photovoltaic devices. It also allows precise and in-line control of the film thickness.

In this research Nickel chalcogenide is studied because in addition to the features like abundance and cost, its electronic and optical properties vary dramatically by modifications in its stoichiometry. Design of the research included mainly two consecutive steps. First step was deposition of uniform, adhesive, sulfur rich Nickel Sulfide compound thin film. X-ray diffraction, scanning electron microscopy provided insight into the chemical structure and morphology of these new structures. Second step was oxidation of the sulfide film to get nickel oxysulfide compound with desired optical properties. UV-Vis spectrophotometer is used in order to get insight into optical property change with oxidation. Firstly, it is found that 8.8×10^{-4} wt% gelatin is effective in preventing precipitation of colloidal S particles in the acidic solution. The optimum deposition conditions are found to be 0.013 M NiSO₄, 60°C deposition temperature, -0.4 V deposition potential vs. Ag/AgCl reference electrode, and solution pH 4.7. These conditions created Ni₃S₂ films on FTO substrate with significantly improved film microstructure, uniformity and adhesion. Also solutions including tartaric acid or sodium lactate are found to have adverse influence on deposition rate, film uniformity and adhesion. Film compound changed to Ni₃S₂ to

NiS₂ when tartaric acid added to the solution. In addition to Nickel sulfide phase, amorphous metallic Nickel formation is observed in this film. Secondly, 550°C is found to be a transition temperature from metallic Nickel sulfide phase to a semiconducting non-stoichiometric Nickel Oxysulfide phase. Band gap showed variety from 2.7 to 3.1eV depending on the oxidation temperatures.

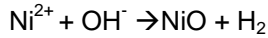
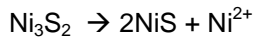
4.2 Future Work

Although it is demonstrated that including oxygen in the sulfide film resulted in a transition to semiconductor material, achieving 1.4eV direct band gap material is challenging due to complex microstructure structure of sulfides and deficient literature about transition metal oxysulfide compounds. There are some future works; however, will be necessary to form and characterize the desired compound.

Firstly, phase transformation of sulfide films oxidized at 550°C for different durations should be observed by using XRD characterization tool. It is expected to observe peak intensity increase and then decrease for the unknown phase with time. It is because oxysulfide will form gradually with time but when oxidation time is further increased all sulfide will be replaced by oxygen and left only oxide phase behind. As a result, if peak intensities follow increase and decrease order with increased oxidation time it will prove the unknown phase is Ni Oxysulfide.

Secondly, before oxidation step, sulfur vacancy free and stoichiometric compound is necessary. Electrochemical deposition of sulfide film alone is not effectively satisfying these conditions. Sulfurization step after the electrochemical deposition is necessary for obtaining sulfur vacancy and defect free, stoichiometric Nickel sulfide films. Also starting with more sulfur to nickel ratio compound such as NiS₂ can end up in better results due to increased probability to engage more oxygen into the structure. In order to get different sulfide phases, different sulfur precursors which don't require acidic environment such as NaS can be used which may also provide opportunity to work in alkaline environment.

Thirdly, thermal oxidation above 550°C cause most of sulfur to form SO₂, leaving highly oxide film behind. Optimum temperature and environment (oxygen and sulfur dioxide pressure) for oxidation should be found. Also anodic oxidation of sulfide film in alkaline solution should be considered. According to the pourbaix diagram for Ni-S-H₂O drawn by thermodynamic simulation NiO can be obtained by applying potential between 1.3 to 0.4eV at some alkaline solution. Ni₃S₂ can be oxidized by released Ni²⁺ ion and released ion will immediately react with OH⁻ and deposit as Nickel oxide on the surface according to the reaction below:



When oxide layer formed on the surface it will passivate surface and reaction rate will drastically decrease. Contrary to this intrinsic problem, this method can may provide ternary compound if the pH, temperature and potential conditions are optimized.

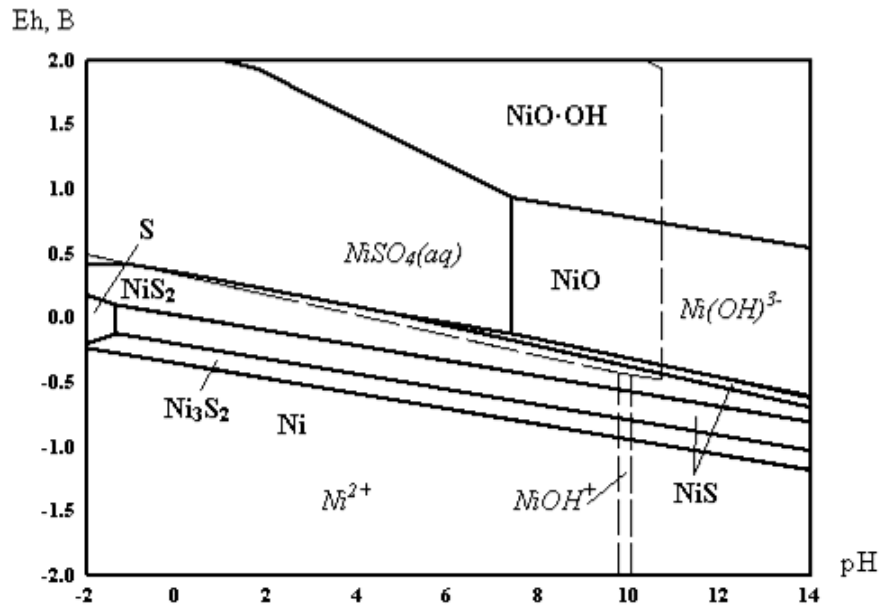


Figure 4.1 Phase diagram of the Ni-S-H₂O system at 25°C [142]

Lastly, electrodeposited Nickel Oxide is expected to perform better structural properties than Nickel sulfide, which in turn improve electrical and optical properties. This is simply due to

bonds in Nickel oxide have higher ionicity than bonds in Nickel sulfide. After Oxide film is formed by electrodeposition, it will be sulfurized in properly ventilated furnace.

REFERENCES

1. U.S. Department of Energy, <http://www.eia.gov/totalenergy/>
2. U.S. Department of Energy, <http://www.eia.gov/oiaf/ieo/world.html>
3. U.S. Department of Energy, <http://www.eia.gov/forecasts/aeo/index.cfm>
4. Energy Information Administration, *Annual Energy Outlook*, (2005).
5. M.I. Hoffert, K. Caldeira, A.K. Jain, E.F. Haites, L.D. Danny Harveyk, S.D. Potter, M.E. Schlesinger, S.H. Schneider, R.G. Watts, T. L. Wigley and D.J. Wuebbles, *Nature*, 395, 881, (1998).
6. Tom Whipple, "Peak Oil and the Great Recession", (2011).
7. The International Energy Agency (IEA), *World Energy Outlook*, (2008).
8. Daniel Lerch, "Making Sense of Peak Oil and Energy Uncertainty", (2011).
9. David Fridley, "Nine challenges of alternative energy", (2010).
10. USGS, "Factors that Influence the Price of Al, Cd, Co, Cu, Fe, Ni, Pb, Rare Earth Elements, and Zn", (2008).
11. US Department of Energy, *Energy Efficiency and Renewable Energy*.
12. *Biofuels, Solar and Wind as Renewable Energy Systems: Benefits and Risks*, New York: Springer, 109–132, (2008).
13. Nathan Lewis, <http://nsl.caltech.edu/files/energy6.pdf>
14. Energy Information Administration, *Annual Energy Outlook*, (2011).
15. Bengt Söderberg, "A Crash Program Scenario for the Canadian Oil Sands Industry," *Energy Policy*, 35, 1931–1947, (2007).
16. U.S. Energy Information Administration, *Annual Energy Outlook*, (2008)..

17. National Academy of Science, "*Coal: Research and Development to Support National Energy Policy.*", Washington, D.C.: National Academies Press., (2007).
18. Nathan Lewis, "Powering the Planet", *Engineering & Science*, 2, 13-23, (2007).
19. National Renewable Energy Laboratory, (2007).
20. U.S. Department of Energy Office of Energy Efficiency, (2004).
21. U.S. Energy Information Administration Annual Energy Review, (2009).
22. USGS, "Factors that Influence the Price of Al, Cd, Co, Cu, Fe, Ni, Pb, Rare Earth Elements, and Zn", (2008).
23. Sandia National Laboratories, <http://www.sandia.gov/>, (2006)
24. National Renewable Energy Laboratory, www.nrel.gov/, (2004).
25. U.S. Energy Information Administration (EIA), "Annual Photovoltaic Module/Cell Manufacturers Survey"
26. The European Photovoltaic Industry Association (EPIA), <http://www.epia.org/>
27. Kazmerski, L., National Renewable Energy Laboratory, (2009).
28. U.S. Energy Information Administration (EIA), "Technology roadmap. Solar photovoltaic energy".
29. U.S. Energy Information Administration (EIA), "Annual Photovoltaic Module/Cell Manufacturers Survey."
30. Harriet Kung, *U.S. Department of Energy*, (2005).
31. C. Wadia, A. P. Alivisatos, D. M. Kammen, *Environ. Sci. Tech.*, 43,2072, (2009)
32. P. Pramanik, S. Biswas, *J. Solid State Chem.* 65, 145, (1986).
33. K. Anuar, Z. Zulkarnain, N. Saravanan, A. Zuriyatina, R. Sharin, *Mater. Sci.* 10, 157, (2004).
34. D. Lincot, *Thin Solid Films* 487, 40, (2005).
35. M. P. Thekaekara, *Suppl. Proc. 20th Annu. Meet. Inst. Environ. Sci.*, 21, (1974).
36. A. E. Becquerel, *Comptes Rendus*, 9, 561, (1839).
37. C. E. Fritts, *Proc. Am. Assoc. Adv. Sci.*, 33, 97, (1983).

38. D. Chapin, C. Fuller, and G. Pearson, *J. Appl. Phys.*, 25, 676, (1954).
39. L.D. Danny Harvey, *Energy and the new reality*, Routledge,(2010).
40. <http://pveducation.org>
41. Henry, *JAP* 51, 4494, (1980).
42. The Electrochemical Society *Interface*, 35, (2008).
43. B. G. Yacobi, *Semiconductor materials: an introduction to basic principles*, (New York; London, Kluwer Academic/Plenum,(2003).
44. Aron Walsh, S H Wei, S Y Chen, X G Gong, 34th IEEE Photovoltaic Specialists Conference PVSC, (2009).
45. Alfred B. Anderson, Sung Y. Hong, J. L. Smialek *J. Phys. Chem.*, 91 (16), 4250, (1987).
46. A.B. Ellis, *Teaching General Chemistry: A Material Science Companion*, American Chemical Society, (1993).
47. C. H. Henry, *J. Appl. Phys.* 51, 4494, (1980).
48. F. P. Koffyberg, *J. Appl. Phys.*, 53, 1173, (1982).
49. A. E. Rakhshani, *Mater. Lett.*, 6, 37, (1987).
50. S. C. Ray, *Solar Energy Mater. Solar Cells*, 68, 307, (2001).
51. F. Marabelli, *Physica B*, 199-200, 255, (1994).
52. K. Santra, *Thin Solid Films*, 213, 226, (1992).
53. L. Wang, *4th World Conference on Photovoltaic Energy Conversion* (Hawaii, 2006).
54. N. Umezawa, A. Janotti, P. Rinke, T. Chikyow, C. G. Van de Walle, *Applied Physics Letters*, 92, 041104, (2008).
55. MRS report: Energy critical elements: Securing material for Emerging technologies.
56. K. Ellmer, *Phys. stat. sol.* , 245, 1745, (2008).
57. F. P. Koffyberg, *J. Appl. Phys.* 53, 1173, (1982).
58. A. E. Rakhshani, *Mater. Lett.* 6, 37, (1987).
59. S. C. Ray, *Solar Energy Mater. Solar Cells*, 68, 307, (2001).

60. F. Marabelli, *Physica B*, 199-200, 255, (1994).
61. K. Santra, *Thin Solid Films*, 213, 226, (1992).
62. A. Jäger-Waldau, M. C. Lux-Steiner, and E. Bucher, *Solid State Phenom.* 37/38, 479, (1994).
63. M. Tao, Photovoltaic Energy Conversion IEEE 4th World Conference , (2006).
64. C. H. Chen, W. Fabian, F. C. Brown, *Phys. Rev.*, B 21, 615, (1980).
65. A. A. Valeeva , *JETP Lett.*, 73, 702, (2001).
66. N. Umezawa, A. Janotti, P. Rinke, T. Chikyow, C. G. Van de Walle, *Applied Physics Letters*, 92, 041104, (2008).
67. S.D. Sartale, C.D. Lokhande, *Materials Chemistry and Physics*, 72, 101, (2001).
68. M. Page, O. Niitsoo, Y. Itzhaik, D. Cahen and G. Hodes, *Energy Environ. Sci.*, 2, 220, (2009).
69. W. Wang, D. Wu, Q. Zhang, L. Wang, and M. Tao, *Journal of Applied Physics*, 107, 123717, (2010).
70. W. Jaegermann and H. Tributsch, *J. Appl. Electrochem.*, 13, 743, (1983).
71. J. A. Baglio, G.S. Calabrese, D. J. Harrison, E. Kamieniecki, A. J. Ricco, M. S. Wrighton, and G. D. Zoski , *J. Am. Chem. Soc.*, 105, 2246, (1983).
72. N. Gaillard, J. Kaneshiro, M. M. Al-Jassim, C. Heske and E. L. Miller, 214th ECS Meeting, (2008).
73. USGS, <http://minerals.usgs.gov/minerals/pubs/commodity/mis.html>
74. David J. Vaughan, *Sulfide Mineralogy and Geochemistry*, V61, June, (2006).
75. A. Ennaoui, S. Fiechter, Ch. Pettenkofer, N. Alonso-Vante, K. Bilker, M. Bronold, H. Tributsch, *Solar Energy Materials and Solar Cells*, 29, 289, (1993).
76. M. Bouroushian, *Electrochemistry of Metal Chalcogenides* (Springer, Berlin, 2010), p. 40.
77. J. Han, W. Zhe, C. Jean-Luc Brédas M. Liu., *J. Chem. Phys.*, 127, 214705, (2007).
78. M. E. Fleet, *Am. Mineral.*, 62, 341, (1977).

79. J. B. Parise., *Acta Crystallogr Struct. Crystallogr. Cryst. Chem.*, B36, 1179, (1980).
80. A. D. Vershinin, E. N. Selivanov, R. I. Gulyaeva, and N. I. Selmenskikh, *Inorg. Mater.*, 41, 882, (2005).
81. V. Rajamani and C. T. Prewitt, *Can. Mineral.*, 12, 253, (1974).
82. N. H. Kolkmeijer and T. A. I. Moesvelt, *Z., Kristallogr., Kristallgeom., Kristallphys., Kristallchem.* 80, 91, (1931).
83. J. D. Grice and R. B. Ferguson, *Can. Mineral.*, 12, 248, (1974).
84. K. Schubert, *Acta Crystallogr Sect. B: Struct. Crystallogr. Cryst. Chem.*, 2631 ,(1997).
85. D. J. Vaughan and J. R. Craig, *Am. Mineral.*, 70, 1036, (1985).
86. D. Lundqvist, *Ark. Kemi, Mineral. Geol.* 24, 1, (1947).
87. L. G. Berry and R. M. Thompson, *Mem.-Geol. Soc. Am.*, 85, 78, (1962).
88. E. Nowack, D. Schwarzenbach, and T. Hahn, *Acta Crystallogr. Struct. Sci.*, B47, 650, (1991).
89. T. Fujii, K. Tanaka, F. Marumo, and Y. Noda, *Mineral. J.*, 13, 448, (1987).
90. Z. W. Lu and B. M. Klein, *Physical Review B*, Volume 54, 19, (1996).
91. K. Ellmer, *Phys. stat. sol.*, 245, No. 9, 1745, (2008).
92. K. Ramasamy, M. A. Malik, P. O'Brien, J. Raftery, and M. Helliwell, *Chem. Mater.*, 22, 6328, (2010).
93. M. M. Uplane, P. S. Patil, M. D. Uplane, and C. D. Lokhande, *Bull. Electrochem.*, 11, 569, (1995).
94. P. Pramanik and S. Biswas., *J. Solid State Chem.*, 65, 145, (1986).
95. L. J. Ferrer and C. Sanchez, *J. Mater. Proc. Tech.*, 92-93, 239, (1999).
96. K. Anuar, Z. Zulkarnain, N. Saravanan, A. Zuriyatina, and R. Sharin, *Mater. Sci.(Medziagotyra)*, 10, 157, (2004).
97. K. Anuar, N. Saravanan, W. T. Tan, S. M. Ho, and D. Teo, *Leonardo J. Sci.*, 16, 1, (2010).
98. Pramanik, P.; Biswas, S. *J. Solid State Chem.*, 65, 145, (1986).

99. Pramanik, P.; Bhattacharya, S. *J. Mater. Sci. Lett.*, 6, 1105, (1987).
100. Anuar, K.; Zainal, Z.; Saravanan, N.; Kartini, A. R. *AJSTD*, 21, 19, (2004).
101. Sartale, S. D.; Lokhande, C. D. *Mater. Chem. Phys.*, 72, 101, (2001).
102. Lee, H.; Kanai, M.; Kawai, T.; Kawai, S. *Jpn., J. App. Phys.*, 32, 2100, (1993).
103. Zhang, L.; Yu, J. C.; Mo, M.; Wu, L.; Li, Q.; Kwang, K. W., *J. Am. Chem. Soc.*, 126, 8116, (2004).
104. Yu, S. H.; Yoshimura, M. *Adv. Funct. Mater.*, 12, 277, (2002).
105. Nomura, R.; Hayata, H. *Trans. Mater. Res. Soc. Jpn.*, 26, 1283, (2001).
106. Alam, N.; Hill, M. S.; Kociok-Kohn, G.; Zeller, M.; Mazar, M.; Molloy, K. C. *Chem. Mater.*, 20, 6157, (2008).
107. O'Brien, P.; Waters, J. *Chem. Vap. Deposition*, 12, 620, (2006).
108. O'Brien, P.; Park, J. H.; Waters, J. *Thin Solid Films*, 431-432, 502, (2003).
109. Musetha, P. L.; Revaprasadu, N.; Malik, M. A.; O'Brien, P. *Mater. Res. Soc. Symp. Proc.*, 879E, Z7.4, (2005).
110. PS Patil, LD Kadam, *Appl Surf Sci.*, 199, 211, (2002).
111. S Hüfner, *Adv Phys*, 43, 183–356, (1994).
112. R.S Conell, D.A Corrigan and B.R Powell., *Solar Energy Mater. Solar Cells*, 25, 301, (1992).
113. P.S. Patil, L.D. Kadam, *Applied Surface Science*, 199, 211, (2002).
114. R. Tsu, L. Esaki, R. Ludeke, *Phys. Rev. Lett.*, 23, 977, (1969).
115. T. Seike, J. Nagai, *Solar Energy Mater.*, 22, 107, (1991).
116. H. Sato, T. Minami, S. Takato, T. Yamada, *Thin Solid Films*, 236, 27, (1993).
117. I. Hotovy, D. Bue, S. Hascik, O. Nennewitz, *Vacuum* 50, 41, (1998).
118. C.M. Lampert, T.R. Omstead, P.C. Tu, *Solar Energy Mater.* 14, 161, (1986).
119. P. Pramanik, S. Bhattacharya, *J. Electrochem. Soc.*, 137, 3869, (1990).
120. A.J. Varkey, A.F. Fort, *Thin Solid Films*, 235, 47, (1993).

121. M. Chigane, M. Ishikawa, *J. Chem. Soc., Faraday Trans.*, 94, 3665, (1998).
122. M. Utriainen, M. Kroger-Laukkanen, L. Niinisto, *Mater. Sci. Eng. B.54*, 98, (1998).
123. A. Surca, B Orel, B Pilhar, P. Bwkovec, *J. Electroanal. Chem.*, 408, 83, (1996).
124. Yi. Xie, W. Wang, Y. Qian, Li. Yang, Z. Chen, *J. Cryst. Growth*, 167, 656, (1996).
125. R.H. Misho, W.A. Murad, G.H. Fatahalah, I.M. Abdul-Aziz, H.M. Al-doon, *Phys Stat. Solidi*, K101, 109, (1988).
126. L.D. Kadam, C.H. Bhosale, P.S. Patil, *Tr. J. Phys.*, 21, 1037, (1997).
127. A. J. Bard and L. R. Faulkner, *Electrochemical Methods—Fundamentals and Applications*, 2nd edition, John Wiley & Sons, New York (2000).
128. J. Cheon, D. S. Talaga, and J. I. Zink, *Chem. Mater.* 9, 1208 (1997).
129. R. Nomura and H. Hayata, *Trans. Mater. Res. Soc. Jpn.* 26(4), 1283 (2001).
130. H. Lee, M. Kana, T. Kawai, and S. Kawai, *Jpn. J. Appl. Phys.* 32, 2100 (1993).
131. D. Lincot, *Thin Solid Films* 487, 40, (2005).
132. H. Sun, D. Qin, S. Huang, X. Guo, D. Li, Y. Luo, and Q. Meng, *Energy Environ. Sci.*, (2011).
133. M. Takahashi, S. Hasegawa, M. Watanabe, T. Miyuki, S. Ikeda, and K. Iida, *J. Appl. Electrochem.* 32, 359, (2002).
134. M. Jayachandran, M.J. Chockalingam and V.K. Venkatesan., *Bull. Electrochem.*, 5, 848 (1989).
135. L. Wang, H. Jia, L. Shi, N. Liao, X. jing Yu, and D. Jin, *Inorganic Materials*, 46, 8, 847–851 (2010).
136. S. Stolen, F. Gronvold, *J. Chem. Thermodynamics*, 23, 77-93, (1991).
137. G. Hodes, *Physical Electrochemistry: Principles, Methods, and Applications*, I. Rubinstein, Editor (Dekker, New York, 1995). p. 515.
138. M. Pourbaix, *Atlas of Electrochemical Equilibria in Aqueous Solutions*, 2nd ed. (National Association of Corrosion Engineers, Houston,(1974).

139. Ethel M. Zaiser and Victor K. La Mer, *Journal of Colloid Science*, 3 (6), 571 (1948)
140. R. G. Chaudhuri, S. Paria, *Journal of Colloid and Interface Science*, 343, 439, (2010).
- 141 Gerhard Angerer , "Raw Materials for Emerging Technologies," Berlin, (2009).
142. Selivanov E.N., Nechvoglod O.V., Pankratov A. A, *6th International Conference on Mathematical Modeling and Computer Simulation of Materials Technologie*, (2010).
143. C. Maurel, T. Cardinal, P. Vinatier L. Petit, K. Richardson, N. Carlie, F. Guillen, M. Lahaye, M. Couzi, F. Adamietz, V. Rodriguez, F. Lagugné-Labarthe, V. Nazabal, A. Royon, L. Canioni, *Materials Research Bulletin*, 43, 5, 1179-1187, (2008).

BIOGRAPHICAL INFORMATION

Munteha Pac was born in Ankara, Turkey. She received a B.S degree from the Metallurgical and Materials Engineering of Middle East Technical University, Ankara, Turkey in 2009. She began his graduate study at the University of Texas at Arlington in Materials Science and Engineering, in 2010. She joined the Giga-Nano Semiconductors group as a graduate research assistant under the guidance of Dr. Meng Tao in 2010 and earned a Master of Science (M. Sc.) degree in 2011.